Colloidal synthesis and characterization of two- and three-dimensional semiconductor nanocrystals

Guilherme Filipe Gonçalves Pereira Fonseca de Almeida

This dissertation is the outcome of three years of research, performed at the Nanochemistry Department of the Italian Institute of Technology under the guidance of Dr. Liberato Manna, and is submitted as partial fulfilment for the degree of Doctor of Philosophy to the Department of Chemistry and Industrial Chemistry of the University of Genoa.

February 2018

UNIVERSITÀ
DEGLI STUDI
DI GENOVA

ISTITUTO
ITALIANO DI
TECNOLOGIA

To my grandfather Ramiro

Declaration

This dissertation is the result of my own work and also includes results of work done in collaboration with other colleagues who are properly acknowledged throughout the text. It has not been previously submitted, in part or whole, to any university or institution for any degree, diploma, or other qualification. Some figures are re-printed from my own publications.

27th February 2018

Summary

Chapter 1. General introduction to the fields of nanomaterials, quantum confined semiconductors and colloidal synthesis.

Chapter 2. Synthesis of chalcopyrite $CuFeS_2$ nanocrystals with pyramidal and bipyramidal shapes. Pyramids exhibited molar attenuation coefficients above 10^6 $M^{-1}.cm^{-1}$ in the near-infrared and a good photo-thermal conversion efficiency (49%) in water. Electronic band structure calculations confirmed that $CuFeS_2$ is an indirect gap material with a narrow intermediate band that is mainly composed of Fe 3d states. This material exhibits an uncommon optical behaviour, as is demonstrated by steady-state and transient absorbance measurements, which is further discussed in the outlook section.

Chapter 3. Synthesis of perovskite $CsPbBr_3$ nanocubes, layered perovskite $[RNH_3]_2[CsPbBr_3]_{n-1}PbBr_4$ nanoplatelets and nanosheets and Cs_4PbBr_6 nanocrystals. Size, shape and phase control could be achieved by simply tuning the amounts of oleylamine and oleic acid. The acid-base equilibria between the two ligands was found to be key to achieve control over the synthesis as well as to stabilize $CsPbBr_3$ samples. ^1H and ^{13}C-NMR studies over temperature revealed that the protonation of oleic acid by oleylamine is an exothermic process in non-polar solvents.

Chapter 4. Synthesis of β-In_2Se_3 nanosheets with monolayer thickness (0.7 nm) and tunable lateral sizes (300 to 900 nm) triggered by aminonitriles. The crystal structure and thickness of the nanosheets could be identified by a combination of diffraction techniques coupled with simulations. The β-In_2Se_3 nanosheets were found to be indirect gap semiconductors (E_g = 1.55 eV) and single nanosheet photodetectors demonstrated remarkable photoresponsivities and response times.

CONTENTS

Foreword

The development of materials with nanometric dimensions has led to enormous technological and economic progress. Landmarks such as the miniaturization of electronic devices, the cost-reduction of catalysts and the genetic manipulation of cells were only possible thanks to the progress that was achieved in the understanding and in the control of condensed matter at the nanometre scale. The author hopes that the following manuscript can be considered a useful and trustful contribution, however small it may be, to the progress of this broad and interesting field.

1 Introduction

It has long been noticed that the properties of non-molecular solids change when their dimensions are reduced to the nanometre scale. An old but well documented example comes from the work of medieval glass artisans who fabricated stained windows by unwarily trapping metal nanoparticles inside glass. Curiously, the windows had a different colour with respect to that of the metal used to stain them (e.g. red-stained windows were typically obtained with gold). Today, it is well known that the colour of a metal nanoparticle is related to the spectral position of its surface plasmon resonance and can be tuned by engineering the size and the shape of the nanoparticle.[1,2] Likewise, many other physical phenomena have natural length scales comprised between 1 and 100 nm (10^2 to 10^7 atoms). Of most relevance to the present work are the size- and shape-dependent optoelectronic properties exhibited by semiconductors when spatially confined at the nanoscale.

The semiconductor technology is one of the great sources of progress in contemporary History. The development of integrated circuits opened the door to the digital age and progress in the fields of solar cells, light-emitting diodes and thermoelectrics bring good hopes to the energy field. In 1975, Gordon Moore forecasted that the number of transistors on integrated circuits would double approximately every two years. Moore's prediction proved accurate for several decades and commercial processors of today contain features as small as 14 nm. However, in this size regime, the optoelectronic properties of many semiconductors differ from those of bulk, according to the quantum confinement effect. It is therefore necessary to study how different semiconductors behave in this size-range. The fabrication of nanostructures evolved considerably over the past four decades and a precise control over size and shape can be achieved for a number of materials using different techniques. The investigation of novel nanoscale systems is a timely subject and, in this work, the colloidal synthesis of novel semiconductive nanostructures is reported along with their optoelectronic characterization.

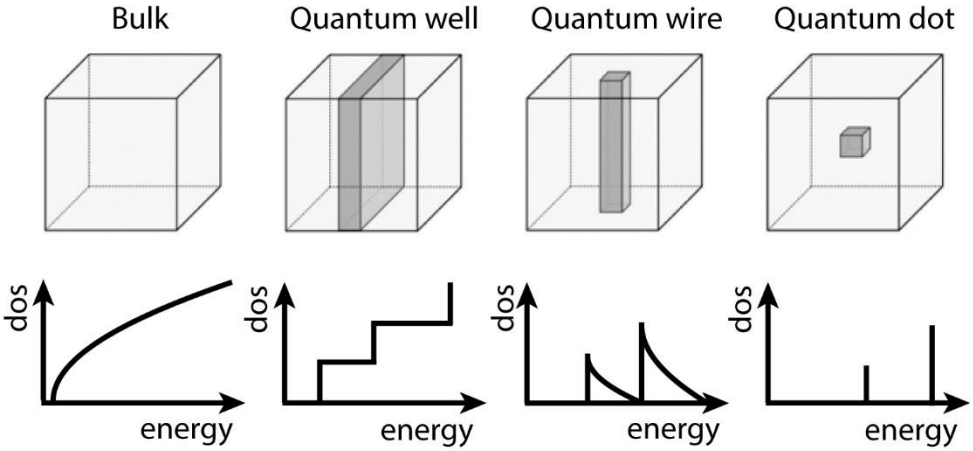

Figure 1.1 Sketch of the density of states of bulk and quantum confined semiconductors

i. Quantum confinement in semiconductors

The electronic properties of a crystal are determined by the long-range interaction between the constitutive atoms. As the dimensions of a crystal are reduced to the size of a few atoms, the electronic energy bands typical of extended lattices are split into discrete levels. The critical size at which the electronic structure starts deviating from that of bulk delimits the quantum confinement regime. This effect has been extensively studied over the past four decades and can be clearly appreciated in the electrical and optical properties of dielectrics in general. In short, quantum confinement leads to an increase of the energy gap that separates the bands, and to the appearance of discrete levels in this energy range.[3–6]

Quantum confinement is particularly interesting for semiconductors (i.e. dielectrics with a band gap < 4 eV) as a route to tailor their density of states. For example, remarkable electronic systems known as quantum wells, wires and dots are obtained by confining a semiconductor in one, two or three dimensions, respectively (see Figure 1.1). Furthermore, confinement in semiconductors also brings important consequences for excitons and, in this regard, two regimes are typically distinguished.[6,7] In the weak confinement regime, the exciton center-of-mass motion

becomes quantized and consequently its energy increases. Further confinement to dimensions below the exciton radius leads to the strong confinement regime where the electron and the hole are no longer correlated, i.e. the Coulomb interaction between them is no longer sufficiently strong to form a bound exciton.

ii. The hot injection method

The synthesis of nanomaterials is typically conducted either via dry methods such as physical and chemical vacuum depositions or by wet-chemical colloidal routes. In this work, all the nanomaterials were synthesized by colloidal chemistry, the oldest route to nanomaterials. In fact, the first scientific account of a colloidal dispersion of nanoparticles, a gold sol, dates from 1857 and is credited to M. Faraday.[8] Thereafter, the field rapidly grew and the term colloidal science was coined.

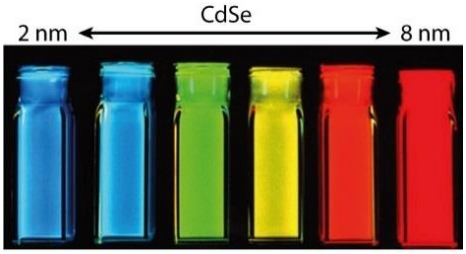

Figure 1.2 Photoluminescent colloidal CdSe nanocrystals with sizes comprised between 2 and 8 nm.

In the 1980s, nanometre sized crystallites of binary compounds could be synthesized colloidally. The first examples of fluorescent quantum dots and of quantum confinement in semiconductors date from this time with the pioneer works of Arnim Henglein, Louis Brus, Arthur Nozik etc.[9,10] However, these colloids often exhibited poor crystallinity and large size dispersions. It was not until 1993 that these issues were solved with the introduction of a novel synthetic method allowing the synthesis of monodisperse cadmium chalcogenides nanocrystals at temperatures up to 300 °C.[11] It consisted in the rapid injection of organometallic reagents into a hot coordinating solvent. This route immediately witnessed great success and a tremendous amount of literature reporting size, shape and phase control of many types of inorganic nanostructures and nanoheterostructures followed. For instance, not only a variety of quantum dots were synthesized but also quantum rods, quantum wires and quantum wells. However, it should be noted that, there is still no general understanding on how shape control is achieved.

iii. Scope of this work

The unifying theme of this work is the colloidal synthesis of semiconductive nanostructures that can efficiently absorb and convert light. In short, in a semiconductor, the absorption of a photon, leads to the excitation of an electron from the valence to the conduction band. This excited state relaxes in time and can do so in several ways. The absorbed energy can be dissipated in the form of phonons (heat), photons (photoluminescence) or can be consumed by a chemical reaction. Alternatively, this excited state can be exploited to generate a photocurrent (by applying a bias across the semiconductor), or, to produce a photovoltage (by dissociating the electron-hole pair).

Herein, novel semiconductor nanostructures capable of light to heat conversion ($CuFeS_2$, chapter 2), photoluminescence ($CsPbBr_3$, chapter 3) and photocurrent generation (In_2Se_3, chapter 4) were synthesized and characterized in terms of their optoelectronic properties. In each chapter, the experimental contribution is preceded by an introduction to the material in question (structure, properties etc.) and its respective research field, and is followed by a perspective section.

iv. References

(1) Ritchie, R. H. *Phys. Rev.* **1957**, *106*, 874.
(2) Kreibig, U. Zeitschrift für Phys. A Hadron. Nucl. **1970**, 231, 128.
(3) Esaki, L. *IBM J. Res. Dev.* **1970**, *14*, 61.
(4) Ekimov, A. *Solid State Comm.* **1985**, *11*, 921
(5) Brus, L. *J. Phys. Chem.* **1986**, *2*, 2555.
(6) Efros, A. L. *Annu. Rev. Mater. Sci.* **2000**, *30*, 475.
(7) Koole, R. In *Nanoparticles*; 2014.
(8) Faraday, M. Philos. Trans. R. Soc. London **1857**, 147, 145.
(9) Henglein, A. *Ber. Bunsen-Ges. Phys. Chem* **1982**, 86, 301.
(10) Rossetti, R. *J. Chem. Phys.* **1984**, *80*, 4464.
(11) Murray, C. B. *J. Am. Chem. Soc.* **1993**, *115*, 8706.

2 $CuFeS_2$ nanocrystals

2.1 Introduction

Chalcopyrite ($CuFeS_2$) is a mineral that has a golden lustre and the most important copper ore. Its name has come to represent an important structural family which consists of ternary compounds with the general formula ABC_2. The interest in compounds of this type arose in the 1950s with the necessity of expanding the library of tetragonal semiconductors which were (and still are!) experiencing enormous success.[1] In fact, the vast majority of known chalcopyrites are also semiconductors and since there are three distinct atomic sites in this structure, the scope for non-stoichiometry and for solid solutions is much greater than that for binary compounds such as CdS or GaAs.[2] Many chalcopyrites have gained considerable interest in the fields of energy conversion[3,4] and infrared non-linear optics.[5,6] Among the many chalcogenides, copper based ones have arguably found most success. They combine interesting optical properties, such as strong light absorption,[7,8] with their non-toxic nature. Furthermore, they are mainly composed of relatively inexpensive elements and can be processed at relatively mild temperatures (< 300 °C) via solution methods.[9] In fact, solar cells based on $Cu_2In_xGa_{1-x}Se_4$ absorber layers have reached efficiencies over 21% and are currently being commercialized.[4,10] In the nanocrystal form, materials such as $CuInS_2$, were found to exhibit strong photoluminescence and good bio-compatibility for e.g. in-vivo imaging.[11]

i. The chalcopyrite structure

The cubic and hexagonal carbon structures that are based on tetragonal bonding are known as diamond and lonsdaleite and any compound with a structure deriving from one or both of these is called adamantine. The similarities between the different adamantine compounds can be illustrated by starting with Ge and performing a proton exchange. If half the germanium atoms donate one (two) proton(s) to the other half, GaAs (ZnSe) is obtained. A one-proton exchange between Ga (Zn) atoms in GaAs (ZnSe) yields $ZnGeAs_2$ ($CuGaSe_2$), which is a II-IV-V_2 (I-II-VI_2) compound Note that the same exercise could be performed starting with PbS and in fact many ABC_2 compounds such $AgBiS_2$ crystallize in the sodium chloride structure.

The chalcopyrite structure is typified by the chalcopyrite itself, i.e. $CuFeS_2$, whose structure was first accurately determined in 1932 by Linus Pauling.[12] The chalcopyrite family consists of the ternary tetragonal adamantine compounds with the formula ABC_2. A and B are metal cations and C is, exclusively, a group V or group VI element. Their lattice can be thought of as a super-lattice of the diamond structure where cells containing A cations alternate with cells containing B cations. The chalcopyrite structure exhibits some chemical versatility. For instance, it tolerates some vacant cation sites as is evident in the defect chalcopyrite structure with the composition AB_2Te_4.

At elevated temperatures, many chalcopyrites disorder into a zinc blende structure[2] and, as most adamantine compounds, chalcopyrites also have a hexagonal analogue which consist of a wurtzite lattice in which the A and B cations are randomly distributed among the cationic sites.

ii. $CuFeS_2$ an intermediate band antiferromagnetic semiconductor

Most technologically relevant compound semiconductors adopt the diamond structure. In these materials, the conduction and valence bands (CB and VB, respectively) derive from the s and p orbitals of the cations and anions, and the

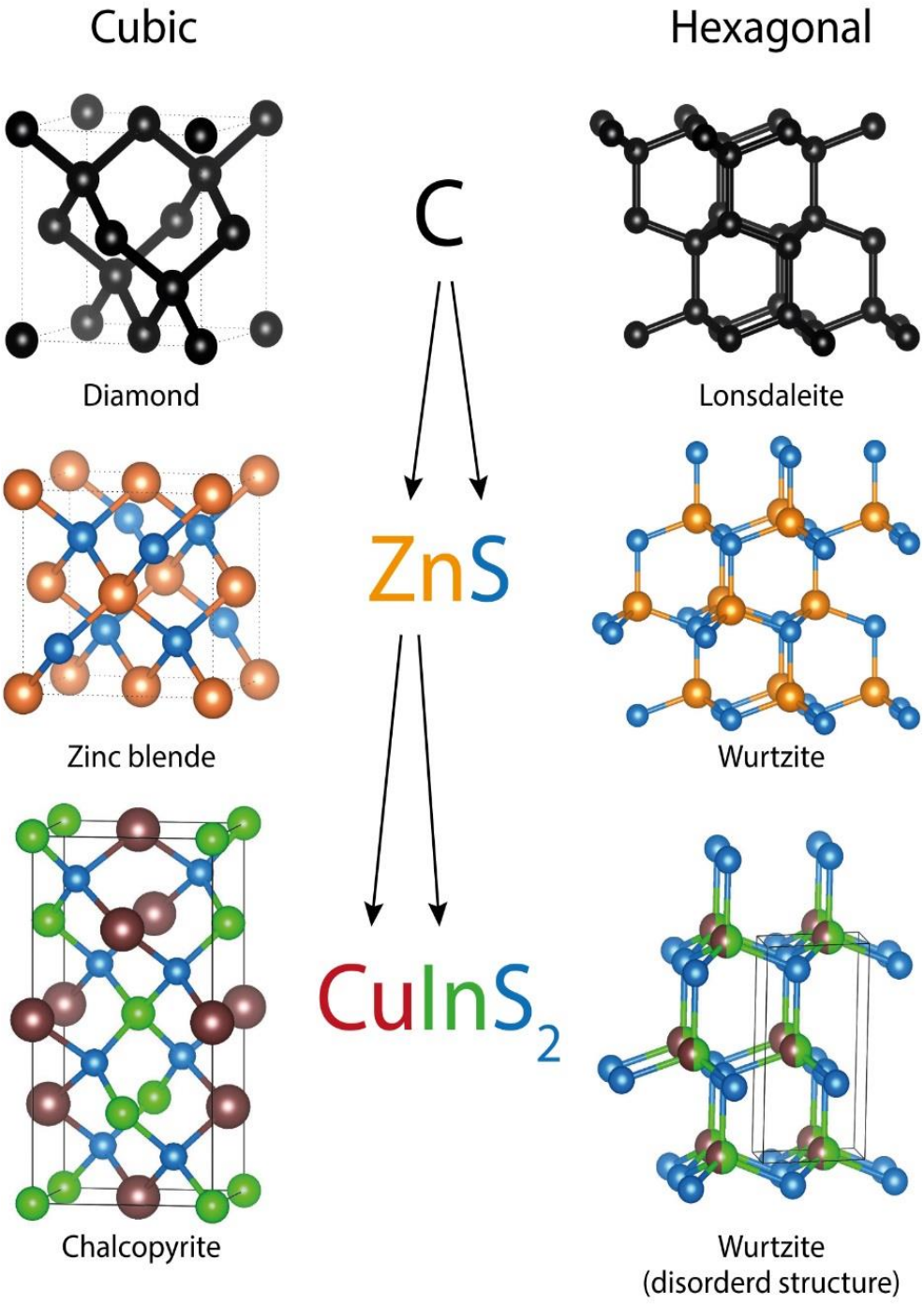

Figure 2.1 From elemental to ternary adamantine compounds

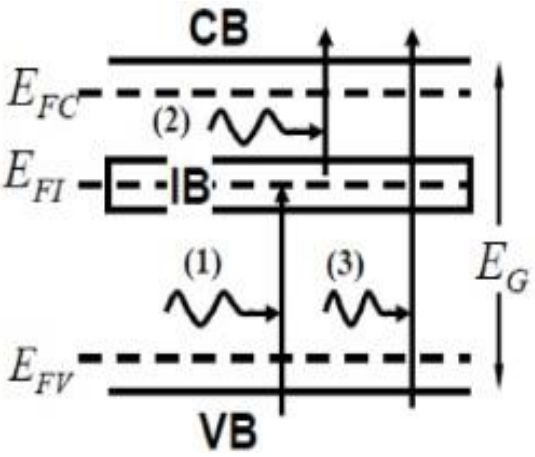

Figure 2.2 In an intermediate band (IB) semiconductor, in addition to valence to conducton band (VB, CB) transitions, sub-bandgap energy (E_G) photons can be absorbed through transition from the VB to the IB and from the IB to the CB (E_F denotes the Fermi energy)

introduction of impurities with d open shells tend to create in-gap states. The chalcopyrite structure can accommodate transition metal cations with open d-shells in high concentrations, leading to the formation of dense intermediate-bands as is the case for $CuFeS_2$. The concept of an intermediate band semiconductor (IBS) is broad, well known and of interest to the field of photovoltaics.[13,14] In short, while photons are absorbed exclusively through the VB to CB transition in a conventional semiconductor, additional sub-bandgap energy photons can be absorbed through transitions from the VB to the IB and from the IB to the CB in an IBS, as is sketched in Figure 2.2.

$CuFeS_2$, is an indirect semiconductor with a narrow optical band-gap of 0.5 eV[1] that corresponds to the VB to IB transition.[15] In addition, it is a strong light absorber (α up to 10^6 cm^{-1} in the visible range)[16] and displays a large Seebeck coefficient (480 $\mu K/V$).[17,18] In comparison with other I-III-VI_2 chalcopyrite semiconductors, $CuFeS_2$ is quite unique due to the presence of magnetic ferric (Fe^{3+}) ions. In fact, this material displays an antiferromagnetic ordering up to 823 K.[17] The antiferromagnetic structure consists of an arrangement in which the two iron atoms that are coordinated to a common sulfur atom have oppositely directed moments as is shown in Figure 2.3.

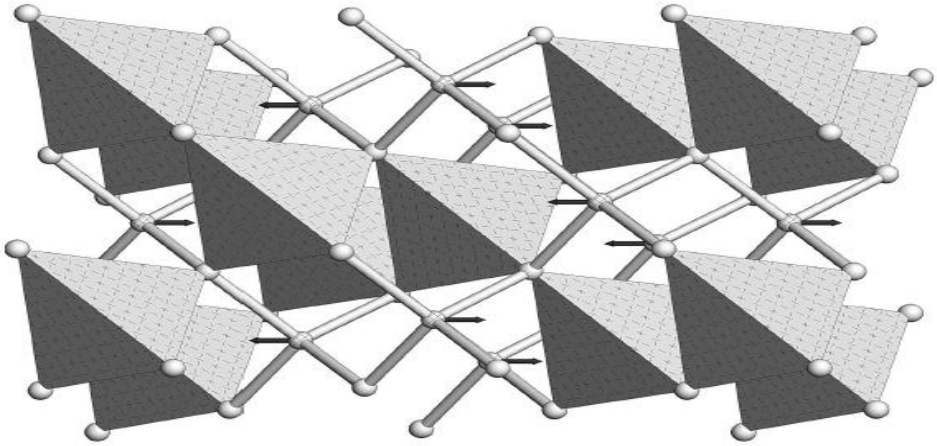

Figure 2.3 Crystal and magnetic structure of tetragonal $CuFeS_2$. Arrows indicate the magnetic moment direction on the ferric ion. Copper atoms are located within the shaded tetrahedral

iii. Goals

$CuFeS_2$ is a strong light absorber and a poor thermal conductor.[18] Despite its large thermoelectric power, its unusually low electrical conductivity hinders its application in thermoelectric and optoelectronic devices.[19,20] On the other hand, its extremely large absorption coefficient in the visible and near-infrared regions coupled with the indirect nature of its band-gap could lead to a reasonable performance as a light-to-heat transducer in the form of nanoparticles, a size-scale where the poor long-range heat transfer process become less relevant. The development of nanoparticles that can efficiently heat the surrounding medium by absorbing electromagnetic radiation (photo-thermal conversion) is key to localized hyperthermia therapy, a non-invasive method of cancer treatment. For this purpose, nanoparticles need to be non-toxic and able to absorb light with frequencies within one of the so called biological windows (0.88-1.24 eV or 1.26-1.77 eV). In this regard, $CuFeS_2$ is likely to satisfy both requirements.

In this work, the colloidal synthesis of tetragonal $CuFeS_2$ nanocrystals via a hot-injection route is reported. Furthermore, the relaxation of photo-generated carriers

was investigated by transient absorption measurements and the photo-thermal conversion efficiency of $CuFeS_2$ nanocrystals dispersed in water was assessed.

Although some chalcopyrite compounds such as $CuInS_2$ had already been synthesized in the form of colloidal nanocrystals, the direct synthesis of phase-pure tetragonal $CuFeS_2$ nanocrystals remained largely unexplored. To the best of the author's knowledge, only Wang et al. could obtain this material at such a high quality, but their synthetic protocol requires the use of non-commercial reagents.[21] The $CuFeS_2$ nanocrystals reported by Liang et al.[22] were most likely contaminated with a fraction of $Cu_{2-x}S$ and previous attempts to synthesize this material within our group resulted in the formation of iron-deficient phases. In fact, the chalcopyrite $CuFeS_2$ is very narrow in composition.[2] Therefore, the main challenges were tuning the relative reactivity of the different elements and avoiding the wurtzite phase using only commercial reagents.[23]

2.2 METHODS

Materials. Copper (I) iodide (≥ 99.5 %, CuI), iron (III) acetylacetonate (≥99.9%, $Fe(acac)_3$), iron (III) chloride (≥97%, $FeCl_3$), 1-octadecene (90%), oleylamine (70%, OlAm), 1-dodecanethiol (≥98%, DDT), chloroform (anhydrous), methanol (anhydrous) and isopropanol (anhydrous) were purchased from Sigma Aldrich. Tri-n-octylphosphine (97%, TOP) and α-methoxy-ω-mercapto polyethylene glycol (SH-PEG-OCH_3, MW: 2000 $g.mol^{-1}$) were purchased from Strem chemicals and Rapp polymere, respectively. All chemicals were used without further purification.

Syntheses (general considerations). All synthetic procedures were undertaken by employing standard Schlenk line techniques assisted by a nitrogen-filled glovebox. Syntheses were performed using 25 mL 3-neck round-bottomed flasks equipped with a thermocouple and a magnetic stirrer at 800 rpm.

Preparation of Cu-precursor. CuI (1mmol) was dissolved in 1 mL of ODE in the presence of TOP (1 mmol) at mild temperatures and in an inert atmosphere.

Preparation of S-precursor. A solution of DDT (1:3 vol.) and OlAm (2:3 vol.) was degassed at 80 °C and heated under nitrogen to 160 °C.

Synthesis of $CuFeS_2$ nanocrystals with a pyramidal shape. The Cu-precursor solution was added to a flask containing $Fe(acac)_3$ (1mmol) and ODE (7 mL) and the mixture was degassed at 80 °C for 1 hour. Thereafter, the temperature was ramped to 280 °C and 3 mL of the S-precursor solution (at 160 °C) was swiftly injected. Upon injection, the initial dark red solution turned dark brown within a few seconds. The reaction mixture was allowed to stir for 15 minutes at 270 °C at which point the heating mantle was removed in order to allow the mixture to cool down to room temperature. The final dark purple solution was diluted in chloroform. Methanol was added to the dispersions and the nanocrystals were separated by centrifugation and re-dispersed in chloroform. Larger crystals were separated by another centrifugation round at ca 1500 rpm.

Synthesis of $CuFeS_2$ nanocrystals with a bipyramidal shape. The procedure was similar to that described for the $CuFeS_2$ pyramids, except for the following: $FeCl_3$ was used instead of $Fe(acac)_3$; the reaction temperature was set to 255 °C; and the reaction time was shortened to 5 minutes.

Ligand exchange (performed by Dr. Tommaso Avellini). The $CuFeS_2$ NCs were transferred to water by replacing the native ligands with hydrophilic thiol terminated polyethylene glycol (PEG) molecules, SH-PEG-OCH_3. In a typical exchange procedure, 3 mL of the NC-solution in chloroform (3.0 μM, 12.6 nm tetrahedral edge) was mixed with a solution of SH-PEG-OCH_3 in methanol (248 mg dissolved in 15 mL of methanol). The amount of PEG units was roughly determined based on a fixed number of ligand molecules per unit NC surface area (50 ligand molecules per square nm of NC surface, in this case). The mixture was shaken vigorously for 2 h, and the PEG-coated NCs were then washed with 20 mL of hexane. The concentrated NC solution was diluted with about 4 mL of methanol, and the washing step described earlier was repeated twice to ensure an efficient removal of the hydrophobic ligands (e.g., DDT/OlAm). The solvent from the PEG-coated NC solution was then removed under reduced pressure yielding the dried NCs, which produced a clear homogeneous purple solution when dispersed in water. Some large NC aggregates were formed during these manipulations and were removed by syringe filtration (0.2 μm pore size). Finally, the excess of free PEG polymer was removed with two cycles of water dilution/concentration filtration using a Millipore Amicon centrifuge filter (100 kDa MWCO, 2300 rpm, 10 min).

X-Ray diffraction (XRD). Samples were prepared by drop-casting concentrated chloroform dispersions onto a zero diffraction silicon substrate. XRD measurements were conducted on a Rigaku SmartLab 9 kW diffractometer with the X-ray source operating at 40 kV and 150 mA. The instrument was equipped with a Cu source and a Göbel mirror (to obtain a parallel beam and suppress the Cu K_β radiation at 1.392 Å) and was used in the θ/2θ scan geometry for data acquisition.

Transmission electron microscopy (TEM, performed with the kind collaboration of Dr. Giovanni Bertoni). Bright field TEM images were acquired on a JEOL JEM-1011 microscope (W filament) operating at an accelerating voltage of 100 kV. Samples were prepared by drop-casting dispersions on carbon-coated 200 mesh copper grids. High-resolution TEM (HRTEM) and high angle annular dark field scanning (HAADF) images were acquired on a JEOL JEM-2200FS microscope, operating at 200 kV. The microscope is equipped with a CEOS objective corrector, allowing a resolution below 0.9 angstroms, and an in-column filter (Ω-type), ultrathin carbon coated Au grids were used and the measurements were carried out using a holder with a beryllium cup for background reduction in the spectra.

Elemental analysis. The composition of the nanocrystals was determined by inductively coupled plasma – optical emission spectroscopy (ICP-OES) analysis performed on aiCAP 6000 spectrometer (Thermo Scientific). The nanocrystal solutions were digested in aqua regia overnight and diluted to a known volume prior to the measurements. The chemical composition was also determined by energy dispersive X-ray spectroscopy (EDS) in the HRTEM described above using a JEOL JED-2300 Si(Li) detector.

Steady state exctinction spectroscopy. Optical extinction spectra of nanocrystals dispersed in chloroform were recorded in quartz cuvettes with a 1 cm path-length employing a Varian Cary 300 UV-Vis spectrophotometer.

Transient absorption spectroscopy (data kindly provided by Dr. Ilka Kriegel). Ultrafast pump–probe measurements were performed on a Ti/sapphire chirp pulse amplified source, with a maximum output energy of about 1 mJ, 1 kHz repetition rate, central wavelength of 800 nm, and pulse duration of about 150 fs. Pump pulses of 490 nm were generated by optical parametric amplification (OPA) in a β-Barium borate (BBO) crystal. White light was generated in a thin sapphire plate in approximately the range of 430–700 nm. The detection system was based on a fast optical multichannel analyzer (OMA) with a dechirping algorithm to obtain chirp-free transient transmission spectra, measured as the normalized transmission

change, ΔT/T. The excitation energy per pulse was kept in the linear regime with a maximum fluence of ~80 μJ/cm^2. All measurements were performed at room temperature on sealed samples prepared in a nitrogen atmosphere.

Photothermal efficiency (PTE, data kindly provided by Dr. Tommaso Avellini). The PTE of the PEG-coated NCs was determined according to the protocol of Roper et al.[24] A quartz cuvette, which contained an aqueous solution of NCs, was placed inside a vacuum chamber and irradiated with a 808 nm continuous laser (RTLMDL-808–5W, Roithner Laser Technik) while the temperature was monitored using a thermo-probe (FOT Lab Kit equipped with Fluoroptic probe, Luxtron). The laser was switched off when the solution temperature reached a plateau and the temperature versus time profile of the solution was recorded. As a control, the same heating–cooling cycle was performed for a quartz cuvette filled with the same volume of deionized water. From the cooling profiles, the PTE was determined.

DFT calculations (kindly performed by Dr. Roberto Gaspari). Calculations have been performed considering the orthorhombic unit cell, which is composed of 4 Fe, 4 Cu, and 8 S atoms, using the plane wave code pwscf.[25] For all calculations, ultrasoft pseudopotentials, a Brillouin zone sampling using a 4 × 4 × 4 Monkhorst–Pack mesh,40 and a plane wave cutoff of 30 and 240 Ry for the wave function and charge density expansion, respectively, were employed. The PBE functional[26] and linear response DFT+U[27] was used. The system geometry was relaxed until the largest force on atoms was smaller than 10^{-4} Ry/Bohr and the largest stress tensor component was smaller than 3×10^{-5} Ry/Bohr^3. Spin polarization was allowed to reproduce the antiferromagnetic ground state of the system.

2.3 RESULTS AND DISCUSSION

Herein is reported the hot-injection synthesis of tetragonal $CuFeS_2$ nanocrystals with trigonal pyramidal and square bipyramidal shapes. These nanocrystals are indirect semiconductors and exhibit strong optical extinction coefficients over the visible and near-infrared regions. Their extinction spectrum is characterized by two bands centred around 1.30 and 2.53 eV, which are ascribed to electronic transitions from the valence band to the empty intermediate band that is mainly composed of Fe 3d orbitals. Carrier dynamics were investigated by transient absorption spectroscopy, pumping at 2.53 eV. Water-transferred nanocrystals were found to exhibit a photothermal efficiency of 49 % upon irradiation at 1.53 eV.

i. Synthesis of $CuFeS_2$ nanocrystals

The colloidal synthesis of metal chalcogenide nanocrystals typically consists of dissolving metal salts in the presence of long chain aliphatic ligands followed by the injection of a chalcogen source. As previously mentioned, the main issue with the synthesis of $CuFeS_2$ nanocrystals is the preferential formation of Cu-rich phases. Therefore, in order to increase the incorporation of Fe in the crystals, it was hypothesized that higher reaction temperatures would promote a higher reactivity of the iron precursor. On the other hand, in order to decrease the reactivity of the copper precursor, alkyl phosphine ligands were added to the reaction scheme since they are known to form strong complexes with Cu^+. In fact, tertiary alkyl phosphines (soft bases) are typically used in cation exchange reactions in order to extract Cu+ (soft acid) from nanocrystals.

The synthetic strategy involved using a copper (I) phosphine complex based on copper (I) iodide (CuI) and tri-octylphosphine (TOP). CuI was preferred over CuCl and CuBr in order to further reduce its reactivity based on the same acid-base considerations that led to the choice of the phosphine ligand (I^- is softer base than Br^- or Cl^-). In short, $CuFeS_2$ nanocrystals were synthesized by injecting a mixture of dodecanethiol (S-precursor, soft base) and oleylamine (capping agent) into a hot

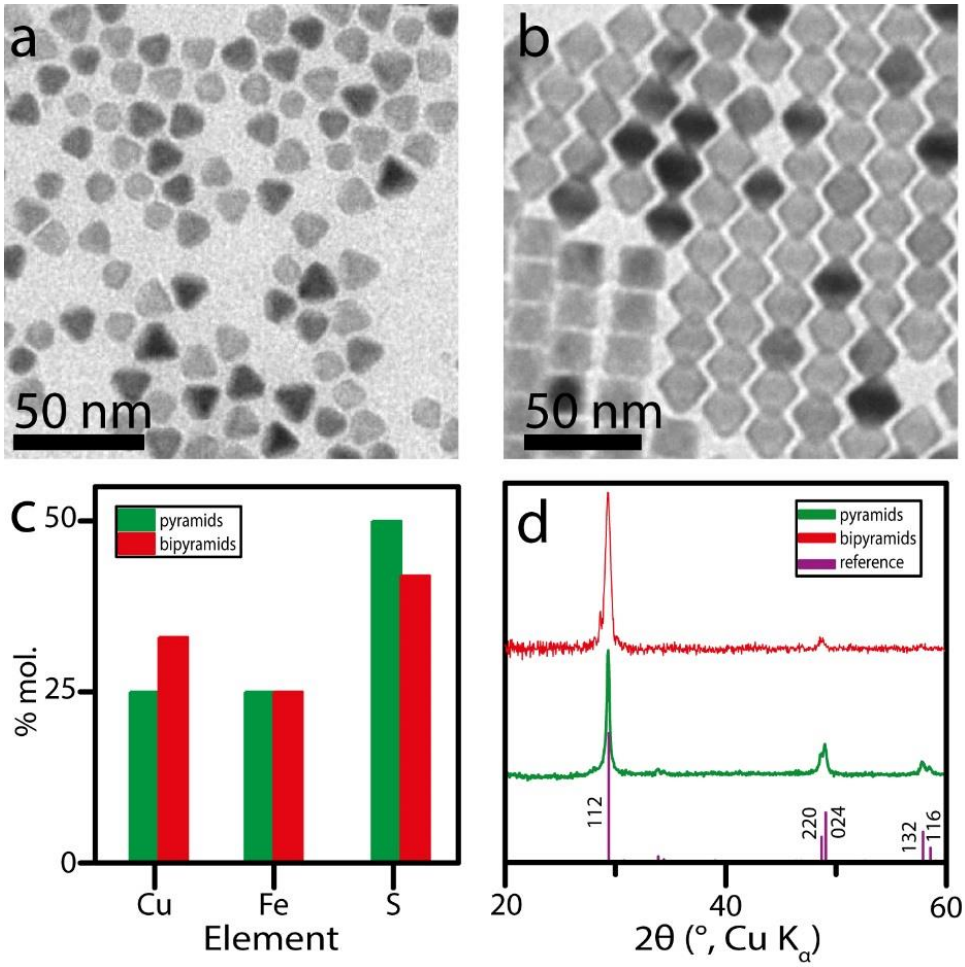

Figure 2.4 TEM image of $CuFeS_2$ nanocrystals with (a) pyramidal and (b) bipyramidal shape along with their (c) elemental composition (as assessed by ICP-OES) and (d) XRD patterns (reference: icsd 96-901-5637)

(270 °C) 1-octadecene solution containing the metal precursors, i.e. the CuI-TOP complex and iron (III) acetylacetonate. This resulted in ca. 10 nm (edge length) nanocrystals with a triangular pyramidal shape and reasonably good size-dispersion, as is shown in figure 2.4a. Inspired by the colloidal synthesis of another copper based chalcopyrite,[28] a second procedure was developed by employing iron (III) chloride ($FeCl_3$) instead of $Fe(acac)_3$. In this case, monodisperse square bipyramids with an edge length of 13 nm were obtained (see Figure 2.4b).

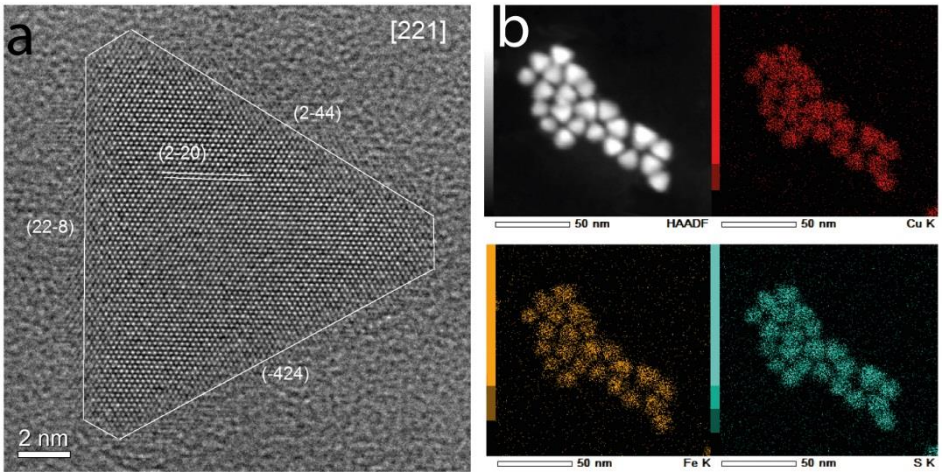

Figure 2.5 (a) HRTEM image of a single $CuFeS_2$ pyramid viewed along the [221] direction. (b) HAADF-STEM image and corresponding STEM-EDS elemental maps of $CuFeS_2$ pyramids

The elemental composition and crystal phase of the nanocrystals were determined through ICP-OES analysis and x-ray diffraction, respectively (see Figure 2.4c,d). The pyramids displayed the desired Cu : Fe : S molar ratio of 1 : 1 : 2 and their XRD pattern matched the reference pattern. However, the bipyramids were found to be off-stoichiometric (copper rich and sulphur poor with respect to iron). Furthermore, the high-angle peaks were missing in their XRD pattern which could suggest a lower degree of crystallinity. On the basis of these results, the $CuFeS_2$ trigonal pyramids were chosen for further characterization.

The structural quality of the $CuFeS_2$ pyramids was further assessed under the high-resolution transmission electron microscope (see Figure 2.5). An HRTEM image of a single but representative nanocrystal viewed along the [221] direction is shown in Figure 2.5a. It can be seen that the edges of this particular nanocrystal are truncated by the (22-8), (-424) and (2-44) planes. The distribution of the constituent elements in the set of nanocrystals shown in the HAADF-STEM image (Figure 2.5b upper left panel) was established by EDS elemental mapping. It is evident that all the

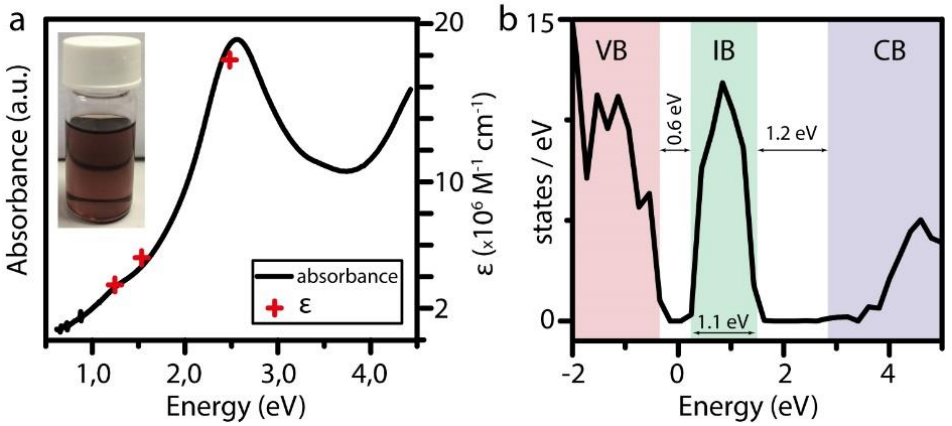

Figure 2.6 (a) Absorbance spectrum and molar attenuation coefficients of pyramidal shaped $CuFeS_2$ nanocrystals dispersed in chloroform (dispersion shown in inset). (b) Calculated joint electronic density of states for $CuFeS_2$

nanocrystals in this set contain all three elements in an apparent homogeneous distribution.

ii. Optical characterization of $CuFeS_2$ nanocrystals

The absorbance spectrum of the dark purple colloidal dispersions of the $CuFeS_2$ pyramids was measured in the range of 0.5 – 4.5 eV, and is displayed in Figure 2.6a. It can be seen that the nanocrystals exhibit a continuous absorbance starting from the near infrared region (ca. 0.5 eV), with a peak at 2.53 eV which is accompanied by a shoulder at ca. 1.30 eV. The slow absorbance onset is in agreement with the indirect nature of the band-gap. Furthermore, the molar attenuation coefficient ε was determined by measuring the absorbance spectra of nanocrystal dispersions at different concentrations (c) and by applying the Lambert-Beer law

$$A(\lambda) = \varepsilon b c$$

in which A is the absorbance at a given wavelength (λ) and b denotes the optical path length. Values range from 10^6 in the near infrared region to 10^7 $M^{-1}.cm^{-1}$ close to the peak maximum, which highlights the strong absorption characteristic of this material.

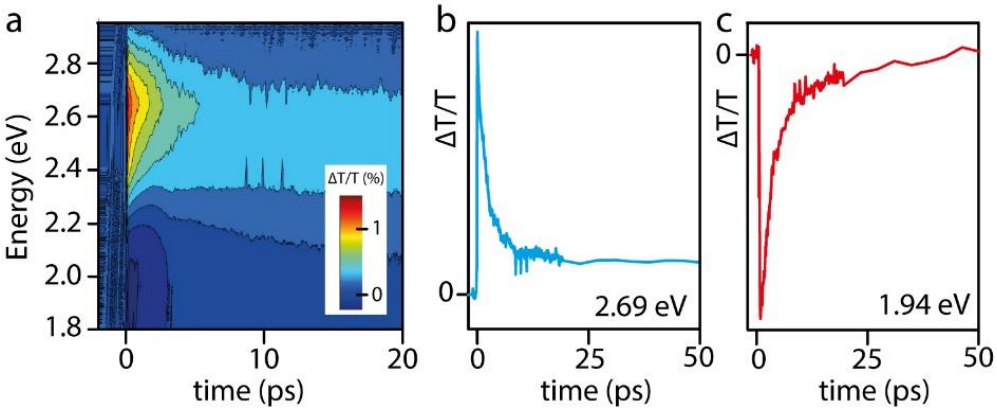

Figure 2.7 (a) Transient absorbance map (2.53 eV, 150 fs pulses) and temporal cross-sections of the map at probe wavelengths of (b) 2.69 and (c) 1.94 eV

In order to interpret the absorbance spectrum, the electronic band-structure and density of states of $CuFeS_2$ were calculated. The electronic band structure, shown in Figure A2.1 of the Appendix, shows that $CuFeS_2$ is an indirect gap semiconductor that is characterized by an empty intermediate band as can also be seen from the electronic density of states shown in Figure 2.6b. This intermediate band has a strong Fe 3d character and, according to the calculations, is quite narrow (with a width of 1.1 eV) and lies 0.6 eV above the valence band maximum (VBM). This energy gap seems to be in good agreement with the experimental optical gap. Furthermore, the energy gap that separates the intermediate and conduction bands seems to explain the dip in absorbance in the 3-4 eV range. However, the energy width from the VBM to the top of the intermediate band is only 1.7 eV, which suggests that the absorbance peak observed at 2.53 eV cannot be explained by electronic transitions alone. In fact, Oguchi et al. showed that in $CuFeS_2$ the real part of the dielectric constant crosses 0 at 1.8 and 2.5 eV and is negative in this range. This suggests that a plasmonic resonance or a similar phenomenon could explain the broad absorption band observed here. This will be further discussed in section 2.5.

Nevertheless, carrier dynamics were investigated via ultrafast transient absorbance spectroscopy and the results will be briefly described. The nanocrystals were excited by 150 fs laser pulses of wavelength corresponding to the absorbance peak maximum (2.53 eV). The transient absorption map is reported in Figure 2.7a. Upon pumping,

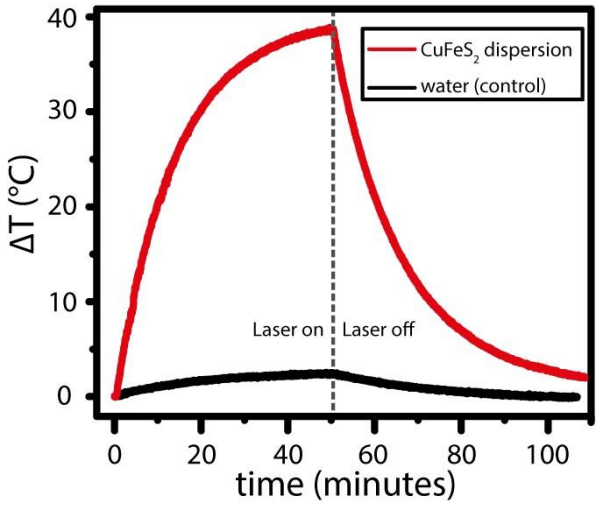

Figure 2.8 Heating of an aqueous dispersion of $CuFeS_2$ nanocrystals upon continuous laser irradiation (1.53 eV, 4.92 $W.cm^{-2}$) and subsequent cooling when the laser is switched off.

the region of highest absorption in the steady state is bleached and, photo-induced absorption is observed at lower energies. The decay dynamics in the bleached region are governed by a fast initial component of about 20 ps, which is then followed by a slower component (see Figure 2.7b). The photo-induced absorption signal follows a similar decay dynamic. (see Figure 2.7c) As previously mentioned, the interpretation of this data is complicated and will be further discussed in section 2.5.

iii. Photothermal conversion in water

It was previously demonstrated that $CuFeS_2$ nanocrystals exhibit a strong molar attenuation coefficient in the near-infrared (> 10^6 $M^{-1}.cm^{-1}$) and in particular, within the first biological window (1.26-1.77 eV). This makes them potentially suitable for photo-thermal bio-applications. The investigation of their potential as photo-thermal transducers in water is described in this section.

In order to transfer the nanocrystals into water, a ligand exchange procedure was employed. In this process, the native ligands, i.e. oleylamine and dodecanethiol, were replaced by molecules containing a thiol (-SH) moiety, which anchors them to the

nanocrystal surface, and a polyethylene glycol chain with a hydrophilic methoxy (-OCH_3) head-group, which renders the nanocrystals dispersible in water.

The photo-thermal conversion was assessed by placing the aqueous nanocrystal dispersion inside a vacuum chamber and irradiating it with a 1.53 eV continuous-wave laser while monitoring the temperature with a thermo-probe. As shown in Figure 2.8, a remarkable temperature increase of almost 40 °C was recorded upon irradiating an aqueous dispersion of $CuFeS_2$ nanocrystals for 50 minutes. In the absence of nanocrystals, a much smaller increase of 2.5 °C was recorded. The typical figure of merit for this type of transducers is the so-called photo-thermal efficiency (PTE). PTE represents the amount of heat generated per incident light power and was calculated following the method reported by Roper et al.[24]In this case, a PTE of 49 % was estimated and is attributed to the high molar attenuation coefficient and the lack of radiative recombination. This value is in line with the PTEs observed in plasmonic copper chalcogenides[29] but it is lower than the record unity efficiencies that have been exhibited by plasmonic metal nanoparticles.[30]

2.4 Conclusion

In this work, original synthetic protocols to synthesize monodisperse chalcopyrite ($CuFeS_2$) nanocrystals with trigonal pyramidal and square bipyramidal shapes were described. These nanocrystals are narrow-gap semiconductors which are characterized by the presence of a narrow intermediate band and high molar attenuation coefficients over the near-infrared and visible spectra regions. These nanocrystals were found to be efficient light to heat transducers that operate through a different mechanism from that of plasmonic nanoparticles like gold or copper chalcogenides. Subsequent collaborative work with Dr. Teresa Pellegrino's group consisting of assessing the potential of these nanocrystals in-vitro for photo-thermal therapy, was quite successful and the results can be found in a joint publication (see Publications section). Nevertheless, the intriguing optical (and electrical) properties of this material remain unsatisfactorily understood. An overview of this question and of recent progress will be given in the following section.

2.5 OUTLOOK

The optoelectronic properties of $CuFeS_2$ are certainly intriguing and, in fact, they remain a matter of scientific curiosity. A brief but hopefully constructive overview of the matter follows.

In comparison with $Cu_2InGaSe_4$, another member of the chalcopyrite family, which is a great optoelectronic material for photovoltaics, $CuFeS_2$ has a narrower optical gap (0.5 eV vs 1-1.5 eV), and typically exhibits higher concentrations of free carriers ($>10^{19}$ cm^{-3} vs. 10^{15}-10^{18} cm^{-3}).[20,31] However it is known to be a poorer conductor and in fact, is not used for either photovoltaics or for thermoelectrics despite its good Seebeck coefficient. Some authors have suggested that its poor electrical conductivity is due to polarons.[20] Indeed, $CuFeS_2$ is an ionic compound and, as such, polaronic effects should be considered. For instance, it is known that in haematite (α-Fe_2O_3), photo-excited electrons become trapped in small polarons which are localized at the Fe sites. Interestingly, the photoexcitation of $CuFeS_2$ also shifts the electron density to the Fe atoms. As previously mentioned, $CuFeS_2$ displays a narrow intermediate band mainly composed of Fe 3d orbitals.

This system is, however, more complicated because it also exhibits antiferromagnetic ordering up to temperatures well above room temperatures (823 K). Nevertheless, E. L. Nagaev, a known theoretical physicist in the field of magnetism, developed a theory entitled "Spin polaron theory for magnetic semiconductors with narrow bands" (1974)[32] which also addresses antiferromagnetic semiconductors [note: a spin polaron (quasi particle) describes the interaction of a charge carrier with the atomic magnetic moments (magnetic lattice)]. In this theory, Nagaev predicted that spin polaron quasi-oscillators may exist in antiferromagnetic semiconductors with narrow bands: "a conduction electron oscillates relative to an equilibrium position which is moving itself through the crystal (...) and is accompanied by a collective excitation of the spin structure" (i.e. a spin wave).

This year, in what seems to be a first confirmation of Nagaev's theory, Gaspari et al. demonstrated that the absorption spectrum of $CuFeS_2$ nanocrystals could be calculated in exceptionally good experimental agreement by introducing a quasi-static oscillator model for the electrons in the intermediate band.[33] In the same work, the-fast carrier dynamics could be modelled. In this case, the excited electrons were divided into two populations, namely hot carriers which are responsible for the bleach signal and thermalized electrons as in the Three-Temperature Model. However, the authors did not describe the dynamics within the other energy reservoirs (i.e. lattice and spin). The existence of spin polarons and of spin waves in this material remains to be demonstrated.

2.6 References

(1) Austin, I. G. *J. Electrochem. Soc.* **1956**, *103*, 609.

(2) Pamplin, B. R. *Prog. Cryst. Growth Charact.* **1979**, *1*, 331.

(3) Yusufu, A. *Jpn. J. Appl. Phys.* **2013**, *52*, 81801.

(4) Jackson, P. Phys. status solidi – Rapid Res. Lett. **2015**, 9, 28.

(5) Boyd, G. *IEEE J. Quantum Electron.* **1972**, *8*, 419.

(6) Isaenko, L. *Cryst. Growth Des.* **2005**, *5*, 1325.

(7) Oguchi, T. *J. Phys. Soc. Jpn.* **1980**, *48*, 123.

(8) Aguilera, I. *Thin Solid Films* **2008**, *516*, 7055.

(9) Mitzi, D. B. *Thin Solid Films* **2009**, *517*, 2158.

(10) Todorov, T. K. *Prog. Photovoltaics Res. Appl.* **2013**, *21* (1), 82.

(11) Li, L. *Chem. Mater.* **2009**, *21*, 2422.

(12) Pauling, L. Zeitschrift für Krist. - Cryst. Mater. **1932**, 82, 188.

(13) Luque, A. *Nat. Photonics* **2012**, *6*, 146.

(14) Okada, Y. *Appl. Phys. Rev.* **2015**, *2*, 021302

(15) Kambara, T. *J. Phys. Soc. Japan* **1974**, *36*, 1625.

(16) Sato, K. *J. Phys. Soc. Japan* **1976**, *40*, 197.

(17) Teranishi, T. *J. Phys. Soc. Jpn.* **1961**, *16*, 1881.

(18) Popov, V. V. *Phys. Solid State* **2011**, *53*, 71.

(19) Kradinova, L. V. *Semicond. Sci. Technol.* **1993**, *8*, 1616.

(20) Zhang, Z. *ACS Appl. Mater. Interfaces* **2016**, *8*, 11215.

(21) Wang, Y.-H. A. *Solid State Sci.* **2010**, *12*, 387.

(22) Liang, D. *Nanoscale* **2012**, *4*, 6265.

(23) Hessel, C. *Nano Lett.*, **2011**, 11, 2560.

(24) Roper, D. K. *J. Phys. Chem. C* **2007**, *111*, 3636.

(25) Giannozzi, P. *J. Phys. Condens. Matter* **2009**, *21*, 395502.

(26) Perdew, J. P. *Phys. Rev. Lett.* **1996**, *77*, 3865.

(27) Cococcioni, M. Phys. Rev. B Condens. Matter Mater. Phys. **2005**, 71, 35105.

(28) Reifsnyder, D. C. *ACS Nano* **2013**, *7*, 4307.

(29) Riedinger, A. *J. Am. Chem. Soc.* **2015**, *137*, 15145.

(30) Qin, Z. *Sci. Rep.* **2016**, *6*, 29836.

(31) Xie, H. *Npg Asia Mater.* **2017**, *9*, e390.

(32) Nagaev, E. L. *Phys. Status Solidi* **1974**, *65*, 11.

(33) Gaspari, R. *Nano Lett.* **2017**, *17*, 7691.

2.7 Appendix

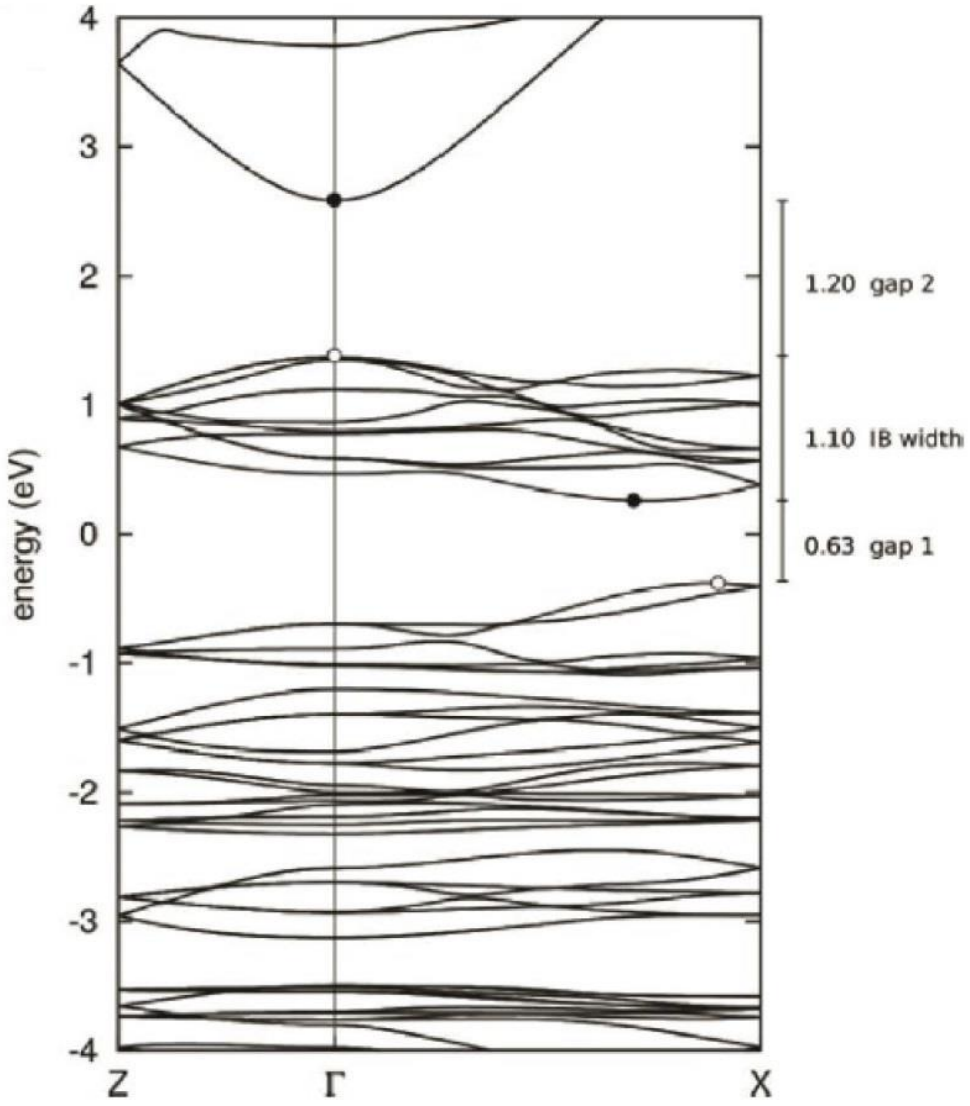

Figure A 2.1 Electronic band structure of tetragonal $CuFeS_2$

3 $CsPbBr_3$ nanocrystals

3.1 Introduction

In 1839, Gustav Rose, a Prussian mineralogist, reported the discovery of a new mineral ($CaTiO_3$) in the Ural Mountains, which he named "perovskite" in honour of the Russian mineralogist Lev Perovski.[1] Its crystal structure, also known as the perovskite structure, was first determined by Victor Goldschmidt[2,3] in the mid-1920s and is common in a variety of minerals – including bridgmanite, $(Mg,Fe)SiO_3$, earth's most common mineral. In fact, this family of compounds has an enormous compositional and structural flexibility, which makes it the most multifunctional ternary structure known, far ahead of the spinel structure.[4,5] Oxide perovskites were initially used as pigments[2,6] and high-k dielectrics[5], until the number of applications expanded to include piezoelectrics[7] and superconductors[8], thanks to the demonstration of ferroelectricity in perovskite $BaTiO_3$ as well as the intimate relation of this phenomenon to the material's structural distortions[9–12]. Shortly after, the semiconducting nature of (lead) halide perovskites was reported but did not find much follow-up in the following years.[13–15] The revival of halide perovskite semiconductors started in the 1990s with the exploration of quantum wells[16–19] and the observation of efficient photoluminescence in micro/nano crystallites[20,21]. However, the major breakthroughs were made during the following decade with two seminal papers. In 2009, the Miyasaka group introduced lead halide perovskites as promising materials for solar cells,[22] a line of research that has been extensively pursued by several groups worldwide and is proving to be very successful, since efficiencies have quickly risen and now match commercial solar cell technologies.[23,24] Then, in 2015, the Kovalenko group introduced the colloidal synthesis of highly luminescent and color-tunable cesium lead halide nanocrystals[25] which are expected to be applied as photonic sources in, for example, solid-state lightning and lasers.[26]

i. The perovskite structure

The ideal ABX_3 perovskite structure belongs to the cubic system and is typically exemplified by $SrTiO_3$, as depicted in Figure 3.1. It consists of a three-dimensional anionic (BX_3^-) framework of corner-sharing (BX_6) octahedra with A-cations that occupy the cuboctahedral voids of the framework. The ideal cubic structure is uncommon because it imposes strict limitations on the ion's relative size. Nevertheless, the perovskite structure tolerates small distortions such as the buckling and rotation of octahedra, which allow the formation of several versions of lower-symmetry (e.g. $CsPbBr_3$). In particular, the relative size of the A cation with respect to the volume of its cuboctahedral cage, dictates the distortion of the anionic framework. The stability of a perovskite structure can be predicted using the octahedral factor (μ) and the tolerance factor (t) that were introduced by Goldschmidt[27]

$$\mu = \frac{r_B}{r_X} \qquad\qquad t = \frac{r_A + r_B}{\sqrt{2}\,(r_B + r_X)}$$

and that can be calculated given the ionic radii (r) of the different elements. While the octahedral factor predicts the structural stability of the BX_6 octahedron (typically, $0.44 \leq \mu \leq 0.90$), the tolerance factor measures the formability of the perovskite structure by considering the size constraints introduced by the cuboctahedral voids (typically, $1.0 > t > 0.7$ and $t > 0.9$ for ideal cubic structure). It should be noted that the tolerance factor has been revised in order to predict the stability of heavy-halide perovskites.[28]

The structural tolerance of the perovskite structure allows for the partial or full substitution of A, B and C ions with other ions of a similar size and valency. It is also possible to replace one of the elements with two other elements that have a complementary valency, as is the case for double perovskites (e.g. Sr_2FeMoO_6). More complex substitutions involving the simultaneous replacement of cations and anions with elements of different valence are also possible.[4,5] Like their oxide counterparts,

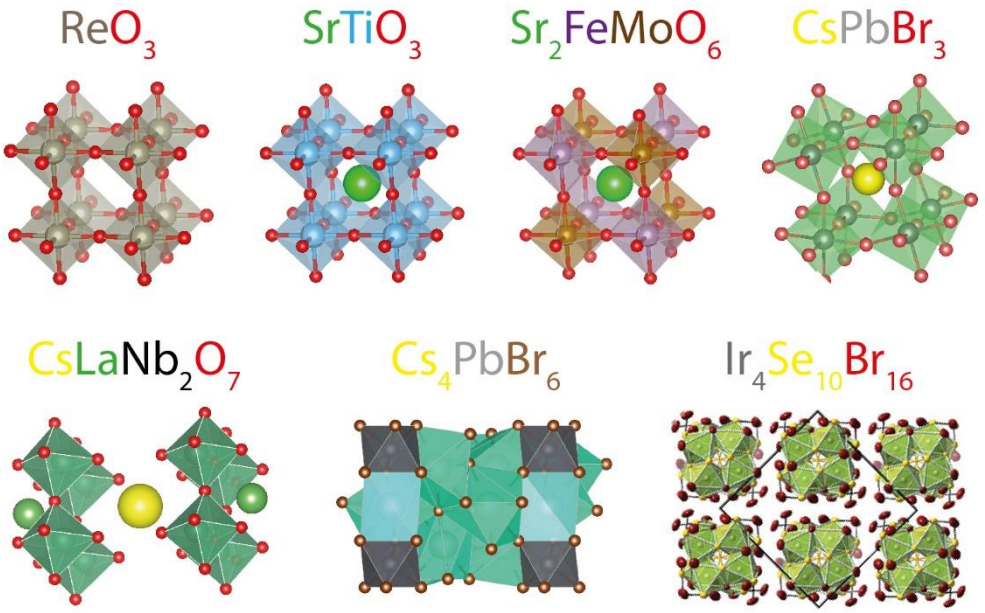

Figure 3.1 (top row) Perovskite and (bottom) derivate structures

halide perovskites exhibit a similar degree of chemical versatility.[29,30] Furthermore, in halide perovskites, the nature of the A cation is not limited to inorganic elements but also encompasses organic cations (e.g. $CH_3NH_3^+$), highlighting the chemical versatility of the perovskite structure.

It is also important to note that other interesting structures can be considered to derive from the perovskite structure. For instance, several layered structures consisting of infinite two-dimensional slabs of corner-sharing BX_6 octahedra which are spatially separated by a motif are well known (e.g. $CsLaNb_2O_7$). Other noteworthy examples are structures in which the BX_6 octahedron are completely disconnected in all three dimensions (e.g. the so-called zero-dimensional Cs_4PbBr_6) and structures in which the BX_6 octahedra cluster (e.g. $Ir_4Se_{10}Br_{16}$).

ii. Lead halide perovskites

In lead halide perovskites ($APbX_3$), the A-sites are occupied by monovalent cations such as methylammonium (MA), formamidinium (FA) or Cs^+, while the X-sites can

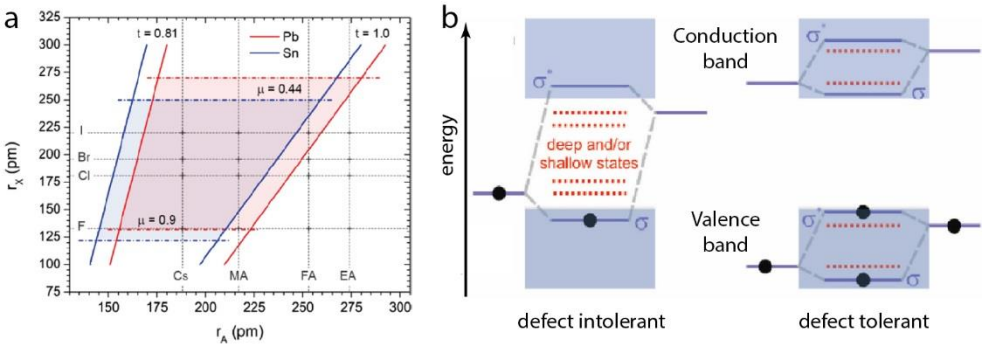

Figure 3.2 – (a) Formability of Pb and Sn halide perovskites as a function of the radii of the A and X elements (Re-printed from Ref. 31). (b) Illustration depicting two limiting cases of a band-structure in semiconductors: defect intolerant and ideal hypothetical defect tolerant (red dashed lines indicate states introduced by defects; re-printed from Ref. 37)

be occupied by F, Cl, Br or I anions (note that, according to structural factors, not every combination is possible, see figure 3.2a). $APbX_3$ are ambipolar direct-gap semiconductors that are known for being strong light absorbers and excellent emitters.[31,32] Furthermore, through the compositional control of halides, their band-gap can be easily and continuously tuned from 1.55 (X=I) to 3.15 eV (X=Cl), i.e. across the whole visible range.

Their electronic structure near the band-edge is mainly dictated by the PbX_3^- framework. In particular, the band-gap is opened across two antibonding bands consisting of Pb and X atomic orbitals. Typically, $APbX_3$ crystals have a high defect density (1-2 at. %) but, fortunately, the most abundant type of point defects (A and X vacancies) either form shallow in-gap traps or are enclosed in the conduction or valence bands.[33] Therefore, in these crystals, the density of electronic traps appears to be low and the emission bands are impressively narrow. Although such a defect tolerance has also been observed in other Pb-based semiconductors,[34] it should be noted that it is in striking contrast with the more drastic consequences of structural defects in conventional semiconductors (e.g. Si, GaAs) in terms of both performance and subsequent fabrication costs. Defect tolerance is considered to be key to the success of $APbX_3$ as active absorber materials in solar cells, whose efficiencies now exceed 22 %.[23,24] Intriguingly, also contributing to such a good performance is the

long lifetime of photo-generated charge carriers in bulk crystals.[31,32,35] This is rather unexpected considering the direct nature of the band-gap. In fact, Sutherland et al. demonstrated that a weak indirect transition exists 60 meV below the direct one.[36]

Reducing the crystal's dimensions shortens photoluminescence lifetimes and attenuates the re-absorption of emitted light.[32] In nanometer sized crystals, quantum yields are high (10-70% depending on composition), even in as-synthesized and non-passivated samples, which further demonstrates the defect tolerance of these compounds. Moreover, simple post-synthetic treatments have been reported to increase their photoluminescence quantum yields up to unity.[37,38] Therefore, $APbX_3$ NCs show great promise for use in light-emitting diodes (LEDs) and, recently, green and red electroluminescent devices with external quantum efficiencies of ca. 10 % have been reported (current commercial technologies: 15 - 40 %).[26,39] Furthermore, $APbX_3$ NCs are also starting to become successful candidates for use in optical amplification and in single photon sources.[26,40]

iii. Synthesis of leads halide perovskites and goals

As stated in the previous section, one of the main advantages of lead halide perovskites with respect to conventional semiconductors lies in the economic competitiveness of their fabrication methods, which are based on low temperature solution processes. These materials can be easily formed due to their highly ionic structure, but it should be noted that they can also be easily destroyed. In fact, they are particularly sensitive to protic solvents, and environmental degradation is a major concern in I-rich compositions.

The main fabrication methods can be classified according to the characteristic of the (solution) systems in terms of the polarity and type of acid-base interactions. Bases such as dimethyl sulfoxide, dimethylformamide and γ-butyrolactone are commonly employed as polar solvents in the fabrication of polycrystalline thin-films and single-crystals. On the other hand, the fabrication of nanocrystals is typically performed in non-polar solvents with the presence of an aliphatic mixture of amines and carboxylic acids (ligands). Although the presence of protic acids is known to

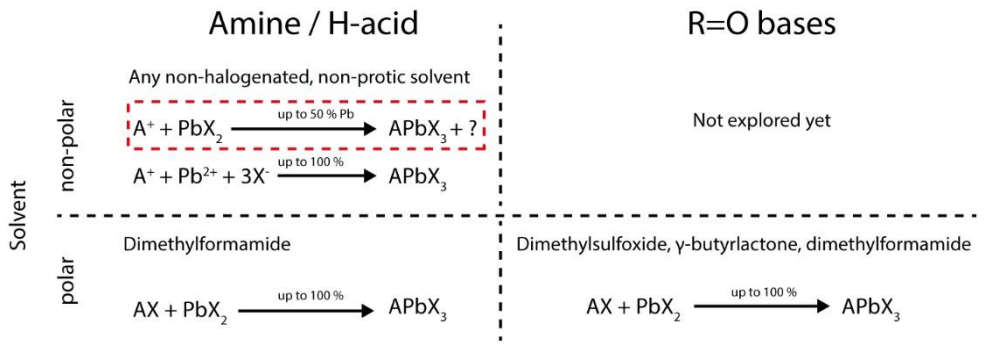

Figure 3.3 Classification of halide perovskite syntheses according to solvent polarity and acid-base characteristics. Nanocrystals (and powders) are typically obtained in non-polar solvents while thin-films and mm-sized single crystals are obtained from polar solvents. Note that dimethylformamide is known to decompose into dimethyl amine and formic acid. The system under investigation in this work is denoted by the red-dashed box and is the most popular route to synthesize halide perovskite nanocrystals

influence the nucleation and growth processes in both types of solvents, the active acid-base equilibria at play remain empirically understood. Moreover given the pace at which lead halide perovskites are progressing towards commercialization, it has now become a necessity to investigate the underlying solution chemistry in order to improve the material's quality standards. In the following sections, experiments devoted to improving the understanding of the synthesis of lead halide nanocrystals in non-polar solvents will be discussed. Using $CsPbBr_3$ as the prototype material, a general synthetic route towards nanocrystals with size, shape and phase control could be devised based on the investigation of the acid base equilibria that occurs between the ligands. Furthermore, a novel synthetic scheme for lead halide perovskite nanocrystals will also be demonstrated.

Before addressing the results of this work, the synthesis of lead halide perovskite nanocrystals (NCs) will be briefly overviewed. As previously mentioned, the synthesis of $APbX_3$ NCs is conducted in a non-polar solvent, and a binary ligand system composed of aliphatic carboxylic acids and primary amines of various chain lengths is often present.[25,41] In the common hot-injection synthesis of cube-shaped $CsPbBr_3$ NCs,[25] Cs-oleate is injected into a hot solution (190 °C) of $PbBr_2$, oleic acid (OA), oleylamine (OlAm), and octadecene. Although this approach leads to highly

luminescent NCs, reports have also indicated a fast de-focusing of the size-distribution within a few seconds of injection,[42] making it difficult to obtain samples with standard deviations below 15% which are highly desirable for both device fabrication and fundamental studies. Moreover, size control is limited (8 - 12 nm) by the narrow workable temperature range, which is bound by the precipitation of $PbBr_2$ at ca. 195 °C and by the co-formation of nanoplatelets (NPLs) below 150 °C.[25,43,44] Furthermore, accurate shape and thickness control of NPLs is yet to be achieved using the hot-injection method.[43,44] In this regard, a clearer understanding of the factors that regulate the formation of NPLs is needed in order to improve their quality. So far, their formation has not only been correlated to low temperatures[44] but also to the presence of short alkylamines,[43] and to high concentrations of alkylammonium ions.[45,46] However, there is no clear consensus as to what the key driving factor is.

3.2 METHODS

Materials. $PbBr_2$ (≥ 98 %), oleylamine (70 %, OlAm), octadecylamine (≥ 98 %), oleic acid (90 %, OA), stearic acid (95 %), hexanoic acid (≥ 99 %, HA), benzenesulfonic acid (≥ 94 %, BSA), didodecyldimethylammonium bromide (≥ 98 %, DDAB), 1-octadecene (90 %), toluene (≥ 99.7 %), toluene-d_8 (99 atom. % D), hexane (≥ 95 %), 2-propanol (≥ 99.8 %) and methyl acetate (anhydrous, 99.5 %) were purchased from Sigma Aldrich and were used without any further purification unless otherwise stated.

Preparation of Cs-oleate precursors.

Solution 1. Cs-oleate in 1-octadecene (Cs_2CO_3 / OA = 26% w). Cs_2CO_3 was weighed inside a 3-neck round-bottomed flask along with oleic acid and 1-octadecene. The mixture was degassed under vacuum at 100 °C for 2 hours in order to obtain a colorless Cs-oleate solution which was then transferred to the glovebox. Typically, 407 mg Cs_2CO_3, 1.55 g OA and 11.7 ODE were combined to obtain a 0.15 M Cs-oleate solution.

Solution 2. Cs-oleate in oleic acid. Cs_2CO_3 was weighed inside a 3-neck round-bottomed flask along with oleic acid (see table 3.2 for concentrations). The mixture was degassed under vacuum at 100 °C for 2 hours in order to obtain a colorless Cs-oleate solution which was then transferred to the glovebox. Diluted solutions were prepared inside the glovebox by dilution with degassed oleic acid.

Syntheses (general considerations). All synthetic procedures were undertaken by employing standard Schlenk line techniques assisted by a nitrogen-filled glovebox where lead (II) bromide and the Cs precursors were stored. Syntheses were performed in 25 mL 3-neck round-bottomed flasks which were equipped with a thermocouple and a magnetic stirrer at 800 rpm.

Synthesis of cube-shaped $CsPbBr_3$ nanocrystals. All nanocrystals were synthesized in 6.0 mL solutions containing 72 mg of $PbBr_2$ (0.2 mmol, 33 mM) and various amounts of oleylamine, oleic acid and 1-octadecene (see table 3.1). Mixtures were degassed for 15 minutes at 100 °C in order to obtain colorless solutions. Thereafter, the temperature was ramped to the desired value under a dry nitrogen flow and 0.5 mL of a 0.15 M Cs-oleate solution in 1-octadecene (solution 1, which had previously been heated for 10 minutes on a hot-plate set to 200 °C) was swiftly injected. Unless otherwise stated, the solutions were immediately cooled after injection with an ice bath and diluted with 5 mL of toluene. The dispersions were centrifuged at 2500 rpm (for 3 minutes) and the nanocrystals were re-dispersed in 2.0 mL of hexane. 4.0 and 4.8 nm nanocubes could not be separated by centrifugation alone (even at 14 krpm). In both cases, 1 mL of oleic acid was added to the dispersion (to assist the

Table 3.1 Synthesis conditions used to prepare the $CsPbBr_3$ nanocubes and some photoluminescence (PL) properties (μ - mean size; σ – standard deviation; T – temperature; λ – photon energy at PL maximum; FWHM – full width at half maximum). All syntheses were immediately quenched upon injection of 0.5 mL of Cs-oleate (0.15 M, in 1-ocatadecene) except the > 100 sample where 2 mL of Cs-precursor was used and the growth time was increased to 60 s.

NC Size		Reaction conditions			Photoluminescence (PL)	
μ (nm)	σ (%)	T (°C)	[OlAm] (mM)	[OA] (mM)	hν (eV)	FWHM (meV)
> 100	n/a	240	3500	3500	-	-
16.4	15	220	500	500	2.39	69
8.7	26	190	500	500	2.41	83
13.2	41	190	250	1000	2.41	103
10.3	26	190	250	500	2.41	84
7.6	16	190	250	250	2.41	80
8.1	10	190	250	63	2.42	75
8.6	12	190	500	63	2.41	74
12.3	31	190	1000	63	2.41	83
7.6	8	150	250	25	2.43	79
4.8	9	125	250	25	2.53	136
4.0	13	120	250	25	2.60	170

precipitation process) and the particles were then precipitated by adding methyl acetate until the solution became slightly turbid. The nanocrystals were separated by the same centrifugation and re-dispersion steps. Nanocrystals smaller than 4.0 nm could also be synthesized (at temperatures under 120 °C), but they could not be isolated from solution by centrifugation alone and the addition of anti-solvents lead to the formation of nanowires (See appendix A3.1).

Synthesis of two-dimensional $[RNH_3]_2[CsPbBr_3]_{n-1}PbBr_4$ nanocrystals. The general procedure consisted in performing the nanocube synthesis under a high concentration of oleylammonium species ([OlAm] = 0.25 M and [OA] = 0.50 M) and varying the concentration of Cs^+ (the smaller the [Cs^+], the thinner the crystals). Note that in this case the injection solution consisted of 0.5 mL of a solution of Cs-oleate in oleic acid (solution 2, 0 ≤ [Cs+] ≤ 300 mM) and that the growth times ranged from 1 to 5 minutes. A complete description of the reaction conditions is provided in table 3.2. Also note that the 1.7 nm thick nanoplatelets tend to transform into 2.3 nm thick nanoplatelets upon dilution, which did not allow me to investigate their photoluminescence quantum yields. In order to obtain $(RNH_3)_2PbBr_4$ nanosheets, the concentration of Cs in the injection solution was set to 0.

Table 3.2 Synthesis conditions used to prepare $CsPbBr_3$ nanoplatelets and $(RNH_3)_2PbBr_4$ nanosheets (1 ML) and some photoluminescence properties (T – temperature; t – reaction time; λ – photon energy at PL maximum; FWHM – full width at half maximum). The injection solution consisted of 0.5 mL of Cs-oleate in oleic acid and $[Cs]_i$ denotes its concentration in the injection solution.

NPL / NS	Reaction conditions					Photoluminescence	
thickness	T	[OlAm]	[OA]	$[Cs]_i$	t	hν	FWHM
nm	(°C)	(mM)	(mM)	(mM)	min	(eV)	(meV)
2.4	90	250	500	300	5		
1.8	90	250	500	23	5		
2.4	140	250	500	150	5	2.67	78
1.8	140	250	500	23	5	2.84	81
1 ML	140	250	500	0	*	3.08	130
2.4	190	250	500	23	5		
1.8	190	250	500	15	1		

$CsPbBr_3$ to Cs_4PbBr_6 transformation reactions. 100 μL of a nanocube dispersion ([Pb] = 13 mM, as measured by ICP) was injected into a stirring hexane solution containing oleylamine (0.4 M) and oleic acid (of various concentrations), with a total volume of 1.0 mL. Aliquots were collected over time in hexane in order to follow their transformation spectroscopically. The transformed nanocrystals were separated by centrifugation and re-dispersed in hexane or toluene for further analysis.

Inductively couple plasma – optical emission spectroscopy (ICP-OES). The concentration of nanocrystal dispersions in Pb was determined by ICP-OES on a aiCAP 6000 spectrometer (Thermo Scientific). The nanocrystal solutions were digested in aqua regia overnight prior to the measurements.

X-Ray diffraction (XRD). Samples were prepared by drop-casting concentrated dispersions onto a zero diffraction silicon substrate. XRD measurements were conducted on a PANalytical Empyrean X-ray diffractometer equipped with a 1.8 kW Cu K_α ceramic X-ray tube and PIXcel3D 2 × 2 area detector, operating at 45 kV and 40mA. The diffraction patterns were collected in air at room temperature using parallel-beam (PB) geometry and symmetric reflection mode. Due to preferential orientation, the diffraction pattern of the $(RNH_3)_2PbBr_4$ nanosheets was collected using an in-plane geometry on a Rigaku SmartLab 9 kW with the X-ray source operating at 40 kV and 150 mA (measurements were kindly performed by Dr. Sergio Marras).

Transmission electron microscopy (TEM, performed in collaboration with Dr. Zhiya Dang). Bright field TEM images were acquired on a JEOL JEM-1011 microscope (W filament) operating at an accelerating voltage of 100 kV. For this purpose, samples were prepared by drop-casting dispersions on carbon-coated 200 mesh copper grids. High-resolution TEM (HRTEM) and high angle annular dark field scanning (HAADF) images were acquired on a JEOL JEM-2200FS microscope, operating at 200 kV. The microscope is equipped with a CEOS objective corrector, allowing a resolution below 0.9 angstroms, and an in-column filter (Ω-type), which

was used to increase the contrast in the images by filtering around the elastically transmitted electrons. To obtain a top-view and side-view of the nanocrystals, the samples were drop-casted on ultrathin carbon on holey carbon coated 400 mesh copper grids.

Nuclear magnetic resonance (kindly performed by Dr. Luca Goldoni)**.** All spectra were acquired on a Bruker Avance III 400 MHz spectrometer, equipped with a Broad Band Inverse probe (BBI). Before each acquisition, automatic routines optimized matching, tuning, resolution and a 90 degree pulse calculation on both the ^{1}H nucleus.
^{1}H-NMR: 16 transients were accumulated, without steady state scans, at 300 K, over a spectral width of 20.55 ppm (offset at 6.175 ppm), at a fixed receiver gain (64), using 30 s of inter pulse delays.
^{1}H-NMR at different temperatures (from 300 to 353 K): 16 transients were accumulated, with 4 steady state scans, over a spectral width of 20.55 ppm (offset at 6.175 ppm), at a fixed receiver gain (64), using 2.5 s of relaxation delay.
^{13}C-NMR: 10240 transients were accumulated after a 30 degree pulse and 4 steady state scans, at 300 K, over a spectral width of 239 ppm (offset at 100 ppm), using 2.2 s of inter pulse delays. The receiver was automatically optimized.
All NMR chemical shifts were referred to the not deuterated toluene residue peak at 7.09 ppm and 129.24 ppm at ^{1}H- and ^{13}C-NMR, respectively.

Steady-state UV-Vis extinction and photoluminescence spectroscopy. Optical extinction and photoluminescence spectra of hexane dispersions were recorded in quartz cuvettes with a 1 cm path-length employing a Varian Cary 300 UV-Vis spectrophotometer and a Varian Cary Eclipse Fluorescence Spectrophotometer respectively.

Photoluminescence quantum yields and time-correlated single-photon counting (kindly performed by Dr. Ali Hossain Khan). The time-resolved photoluminescence spectra were measured using an Edinburgh Instruments FLS920 spectrofluorometer. The PL decay traces were recorded by exciting the samples at 405 nm using a 50 ps

laser diode. The data were collected at the PL peak position with an emission bandwidth of 10 nm. The photoluminescence quantum efficiencies were measured using the same instrument with an integrating sphere, exciting the nanocrystal solution at 400 nm. The optical density of the nanocrystal solution was 0.1 at 400 nm.

Fourrier transformed infrared spectroscopy (data kindly provided by Dr. Francisco Palazon). Infrared spectroscopy was conducted in attenuated total reflection (ATR) mode from 600 cm-1 to 4000 cm-1 with a resolution of 4 cm-1 in a Vertex 70v instrument from Bruker. 256 scans were averaged for each sample as well as for the background.

3.3 Results

The $CsPbBr_3$ NCs that are reported in this work were all synthesized based on the synthesis by Protesescu *et al.*[25], and the size and shape control was obtained by only altering the reaction temperature and the concentrations of OA, OlAm and Cs^+. In short, 72 mg of $PbBr_2$ (0.20 mmol, 33 mM) were dissolved in a 6.0 mL mixture with various concentrations of ligands (OlAm and OA) and solvent (1-octadecene). After $PbBr_2$ was dissolved at 100 °C under vacuum, the mixture was heated to the target reaction temperature under nitrogen, at which point 0.5 mL of a warm Cs-oleate solution was injected, resulting in an instantaneous nucleation burst. Thereafter, samples were immediately cooled to room temperature with an ice bath and separated by centrifugation (see the Methods section for additional details).

It is important to note that $PbBr_2$ is highly soluble in the binary ligand mixture (OLAM + OA) but not in OA or OLAM alone (as will be further discussed later). Under the conditions that are proposed by Protesescu *et al.* ([OA] = [OlAm] = 0.25 M), $PbBr_2$ precipitates when the solution is heated to a threshold temperature of 195 °C.[25] By increasing the amount of ligands, this precipitation temperature can be increased up to 290 °C, as shown in Figure 3.4a, which allows for the synthesis of $CsPbBr_3$ NCs even at high temperatures. On the other hand, keeping the concentration of ligands close to the minimum amount needed to solubilize the $PbBr_2$ enabled the synthesis of nanocubes with narrow size distributions (Figure 3.4c).

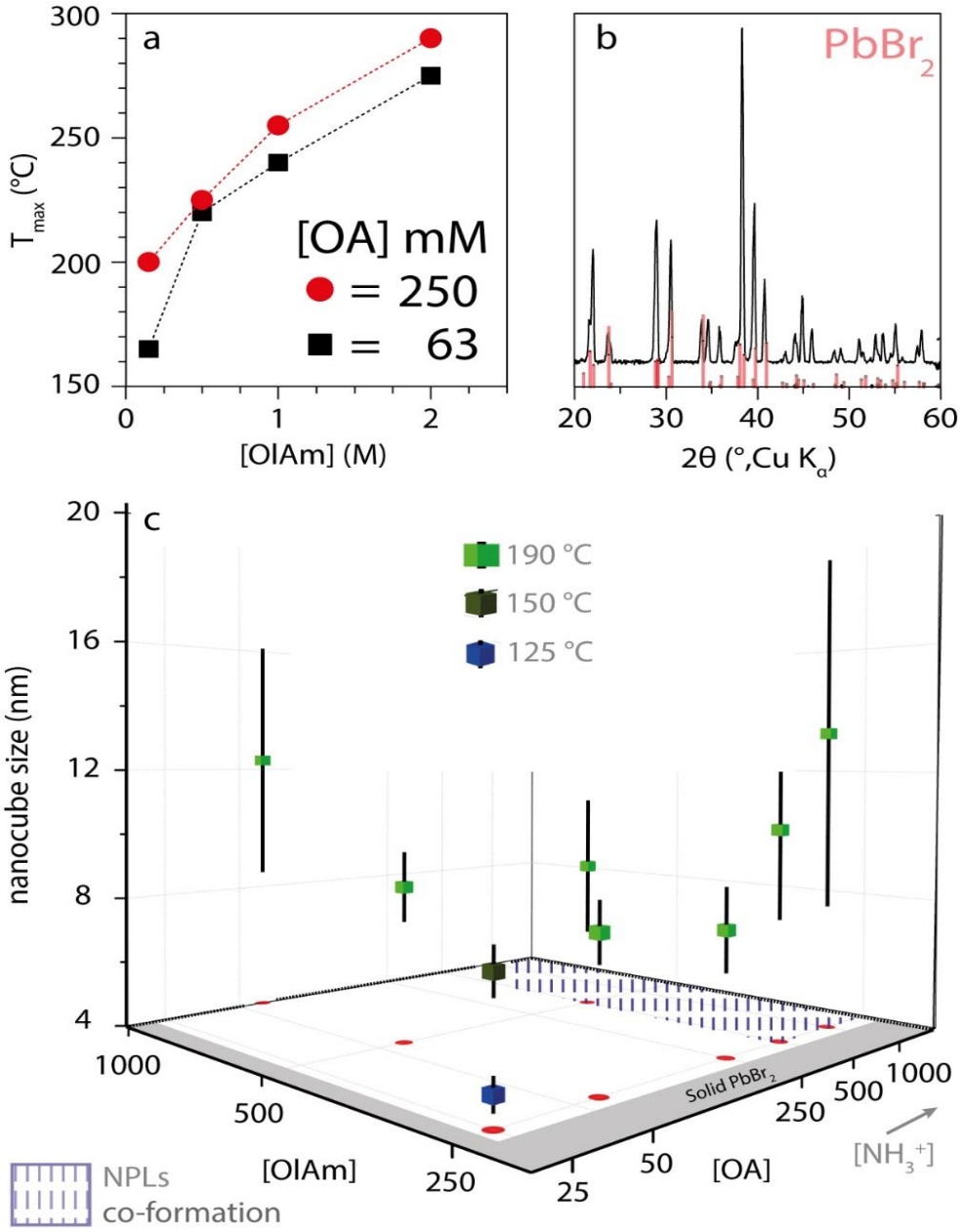

Figure 3.4 (a) Maximum reaction temperature T_{max} as a function of ligand concentration; at Tmax, $PbBr_2$ precipitates from the reaction medium 33 mM $PbBr_2$ in ODE with [OA] set to a constant of 63 and 250 mM). (b) XRD pattern of $PbBr_2$ precipitated from the mixture at 190 °C. (c) Sizes of $CsPbBr_3$ nanocubes that were synthesized using various concentrations of oleylamine and oleic acid and different reaction temperatures (size distributions are represented as vertical bars across each symbol.

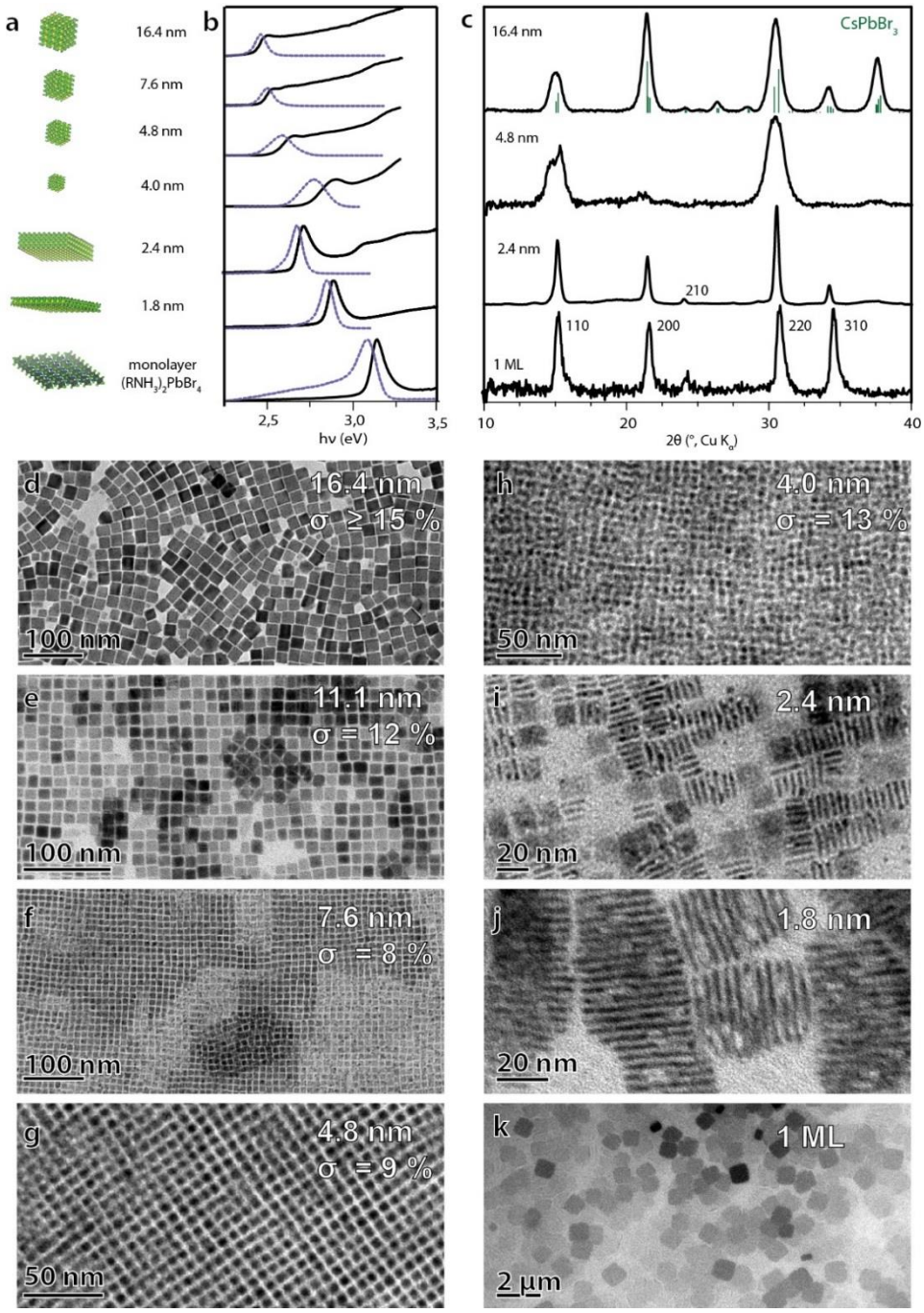

Figure 3.5 (a) Image illustrating the range of monodisperse $CsPbBr_3$ nanocubes, nanoplatelets and nanosheets that were synthesized using only oleylamine and oleic acid as ligands. (b) Absorbance (black solid line) and photoluminescence (blue dashed line) spectra, (c) XRD patterns and (d-k) TEM images of the depicted samples.

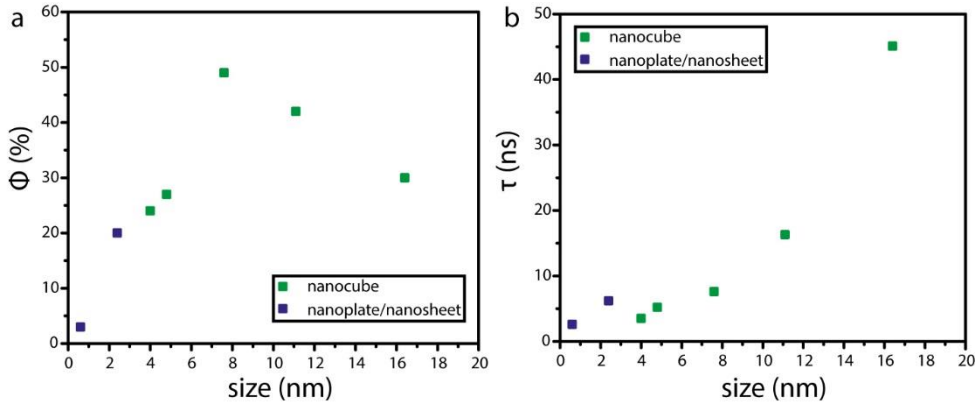

Figure 3.6 Photoluminescence quantum yields (Φ) and lifetimes (τ) of the various sized $CsPbBr_3$ nanocrystals (measured at an excitation wavelength of 3.10 eV)

Examples of NCs that can be synthesized with this general scheme are reported in Figure 3.6: 4.0 to 7.6 nm cubes (σ = 8 - 13 %) were prepared at 120 - 150 °C in the presence of 0.25 M OlAm and 25 mM OA. Larger cubes were obtained by increasing the reaction temperature, which also required increasing the concentration of ligands. For instance, 16.4 nm cubes (σ = 15 %) were obtained at 220 °C. Syntheses that were performed at 240 °C ([OlAm] = [OA] = 1.5 M) delivered even larger nanocubes (over 100 nm), but they had a very broad size distribution (see Table 3.1 and Figure A3.2 of the appendix). All nanocubes that were synthesized with this approach had crystal structures that matched the orthorhombic $CsPbBr_3$ phase (Figure 3.5c), narrow photoluminescence (PL) peaks and high PL quantum yields (see Table 3.1 and Figure 3.6).

Synthesizing $CsPbBr_3$ nanocubes using the minimum amount of ligands that is needed to solubilize $PbBr_2$ also suppressed Ostwald ripening, which normally leads to the fast defocusing of NC size within seconds of the injection of Cs^+. The suppression of Ostwald ripening was clear, since nearly monodisperse NCs could be obtained even when the reaction was allowed to cool without an ice bath, i.e. solely by removing the heating mantle, which is a procedure that normally requires at least 10 min for the flask to cool down (as illustrated by the 7.6 nm nanocubes shown in Figure 3.5f). Furthermore, under such reduced concentrations of ligands, the formation of nanoplatelets was never observed, regardless of the reaction

temperature. Rather, the amount of NPLs increased when the concentration of oleic acid in the reaction mixture was increased (see Figure A3.3). Following this observation, pure, square shaped (ca. 10 x 10 nm, x 2.4 nm thick) $CsPbBr_3$ NPLs were prepared at 140 °C by increasing the concentration of oleic acid in the reaction mixture (from 25 mM to 0.5 M) as well as in the injection solution (see Figure A3.4). The thickness of the NPLs could be reduced by decreasing the amount of Cs^+ injected (while keeping the amount of OA constant, see table 3.2), as is evidenced by the absorbance and PL spectra of the samples (see bottom 3 rows of Figure 3.6a,b). Similar to findings in previous reports,[46,47] the NPLs exhibited narrow PL peaks (see Figure 3.5b, Figure 3.6 and table 3.2) and their structural anisotropy was evidenced by strong (hk0) reflections in their XRD patterns (Figure 3.5c; see figure 3.7 for representative high-resolution transmission electron microscopy images).

Interestingly, when Cs^+ ions were omitted from the injection solution, a white precipitate formed upon cooling the mixture. This precipitate consisted of micron-sized nanosheets whose crystal phase could be assigned to that of a hybrid organic-inorganic two-dimensional perovskite slab with the formula $(RNH_3)_2PbBr_4$, in which RNH_3 denotes the oleylammonium ion (Figure 3.5k). Its PL spectrum (Figure 3.6b, bottom row) is characterized by a peak at 3.09 eV with a long tail to lower energies, which is in agreement with previous reports on two-dimensional perovskites.[48]

t was also observed that by increasing the concentrations of both oleic acid and oleylamine in the reaction mixture, the NCs crystallized in the lead-poor hexagonal Cs_4PbBr_6 phase (Figure 3.8a-e), which is a non-luminescent insulator that is characterized by a strong and narrow absorption band resembling that of individual $[PbBr_6]^{4-}$ clusters (Figure 3.8b).[49] A similar result was observed by treating $CsPbBr_3$ NCs with an excess of these same ligands (OA and OLAM), as their phase changed to Cs_4PbBr_6 (Figure 3.8f-h). In this case, 8-nm cube-shaped NCs could be transformed into ca. 20 nm hexagonal NCs. This increase in NC size is in agreement with the two-step dissolution-recrystallization mechanism that is reported in similar works.[50,51] Interestingly, the rate of this transformation was found to be dictated by the ratio between OA and OlAM, and will be discussed in the next section.

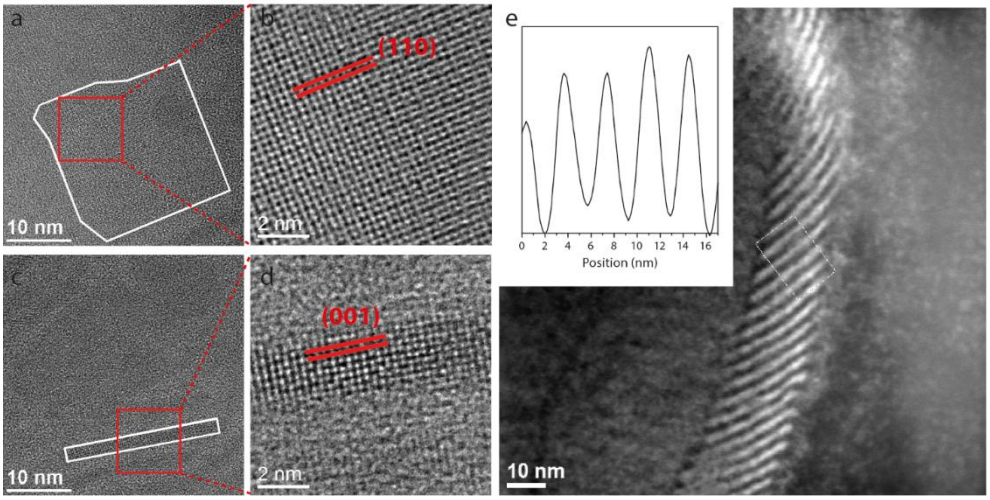

Figure 3.7 (a-b) top- and (c-d) side-view STEM and HRTEM images of 2.4 nm thick $CsPbBr_3$ nanoplatelets, respectively. (e) HAADF image of stacks of 1.8 nm thick $CsPbBr_3$ nanoplatelets from side-view (inset: contrast line-scan of the region delimited in the image)

3.4 DISCUSSION

i. The acid-base equilibrium

This section discusses the acid base chemistry of OlAm and OA mixtures in non-polar solvents and how the size, shape and phase control of cesium lead bromide NCs are regulated. It is known that, in aprotic solvents, partially substituted nitrogen bases and carboxylic acids can form hydrogen bonded ionic salts.[52] The first hint of the formation of ammonium carboxylate salts can be observed by simply mixing OlAm (base, B) and OA (AH) at a 1: 1 mol. ratio at room temperature. This generates heat and leads to the formation of a gel (Figure 3.9a), which indicates that, under these conditions, the ions mainly associate in the salt form under these conditions.

$$B + H - A \leftrightarrow BH^+ \ldots A^- \qquad \text{(eq. 1)}$$

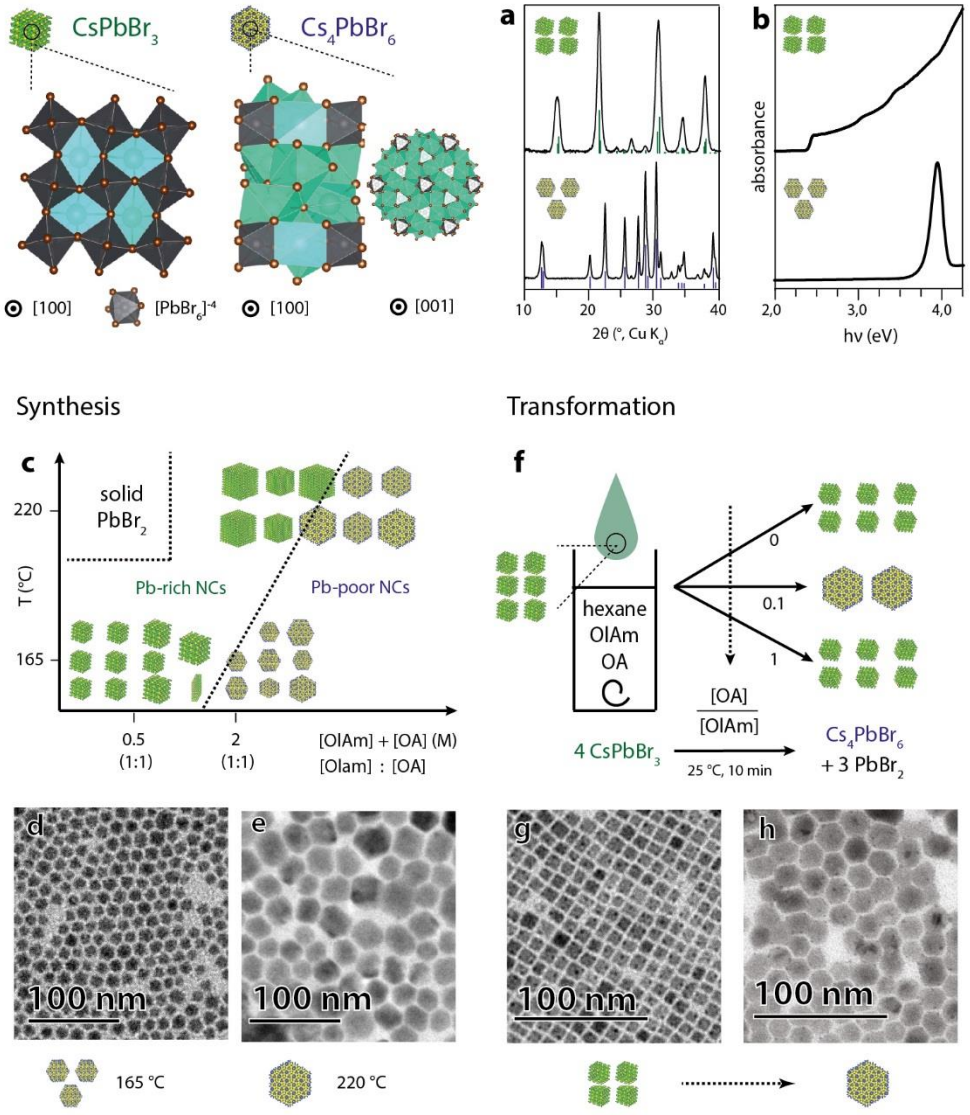

Figure 3.8 Ligand-mediated synthetic and post-synthetic phase control of cesium lead bromide NCs (OlAm= oleylamine, OA = oleic acid). (a) Typical XRD patterns and (b) absorbance spectra of $CsPbBr_3$ and Cs_4PbBr_6 NCs. (c) Scheme depicting how the interplay between reaction temperature and ligand concentration affects the crystal structure and, subsequently, the composition of the obtained NCs. TEM image of Cs_4PbBr_6 NCs synthesized at (d) 165 and (e) 220 °C. (f) Illustration depicting the ligand-driven transformation of $CsPbBr_3$ NCs into Cs_4PbBr_6 NCs: in short, 100 µL of a dispersion containing $CsPbBr_3$ nanocubes was added to a stirring solution (1.0 mL) that contained a fixed concentration of OlAm (0.4 M) and various concentrations of OA and solvent (hexane), and the transformation was followed spectroscopically. TEM images of NCs (g) before and (h) after transformation.

To confirm the formation of this ammonium carboxylate, nuclear magnetic resonance (NMR) analysis was performed on OlAm and OA mixtures in toluene-d_8 When an excess of oleic acid is present, the α-CH_2 resonances of oleylamine (19) exhibit a downfield shift in the ^{1}H-NMR spectrum, which occurs as a consequence of the nitrogen protonation, while the α-CH_2 resonances of oleic acid (2) show a downfield shift with the de-protonation of the carboxylic acid (Figure 3.9c). Opposite shifts are observed in the ^{13}C-NMR spectrum i.e. upfield shifts occur for the α -CH_2 carbon of both the OlAm and the OA as a result of the protonation of the adjacent functional group (Figure 3.9d). In the appendix (section A3.5) is reported the complete assignment of the components in a model mixture of 0.5 M OlAm and 1 M OA in toluene-d_8. The α-CH_2 resonances of OlAm (19) and OA (2) were unambiguously identified by the ^{1}H-^{13}C-HMBC NMR spectrum (Figure A3.5).

As previously mentioned, the formation of the ammonium carboxylate is exothermic, which implies, based on Le Chatelier's principle, that the equilibrium will shift towards the reactants when the temperature is increased. This was confirmed by ^{1}H-NMR spectroscopy. Notably, the α-CH_2 ^{1}H-NMR resonances of the protonated oleylamine (19) and those of OA (2) shifted upfield when the temperature was increased, which confirms the de-protonation of the oleylammonium ions and the protonation of the carboxylic acid (Figure 3.9e). These facts have important implications in the colloidal synthesis and phase stability of $CsPbBr_3$ NCs, as will be outlined in the next section.

ii. Role of ligands in size and shape control

First, it is important to re-emphasize the fact that both ligands are necessary to solubilize solid $PbBr_2$, which highlights the active role of both the ammonium and the carboxylate species in this process (note that heating $PbBr_2$ in oleylamine leads to the formation of lead oxyhalide, see appendix A3.6). In this system, $PbBr_2$ exhibits an inverse solubility behavior (see Figure 3.4a,b) which is related to the decrease in the concentration of ammonium and carboxylate species when the temperature is increased, as has been previously demonstrated. In addition, it was found that this binary ligand mixture can also dissolve $CsPbBr_3$ NCs (Figure 3f-h). This

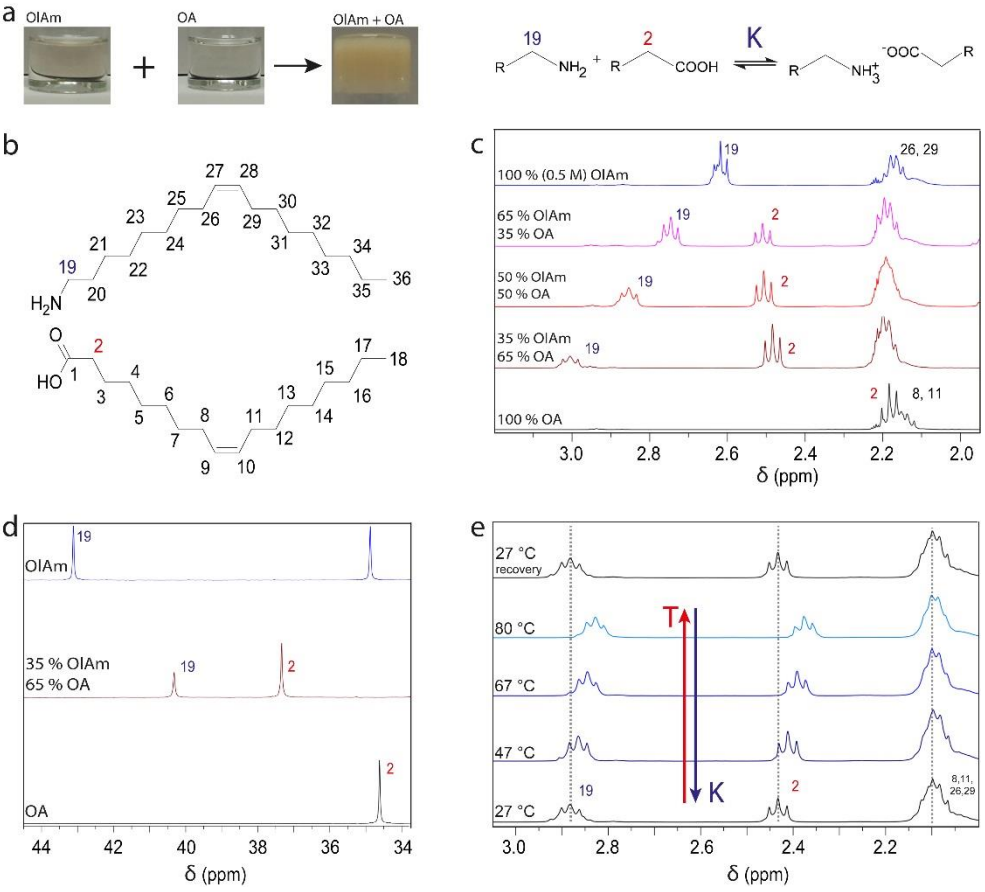

Figure 3.9 (a) photographs illustrating the formation of the oleylammonium oleate salt. (b) Structure of oleylamine (OlAm) and oleic acid. Selected regions of the (c) ^{1}H- and (d) ^{13}C-NMR spectra of OlAm and OA solutions in toluene-d8. (e) ^{1}H-NMR spectra of a mixture of OlAm and OA in toluene-d_8 recorded at different temperatures in the range of 27 to 80 °C (upfield shifts are observed for the α-CH_2 1H-NMR resonances 19 and 2, while all the other signals, e.g. 8,11,26,29, remain unchanged). All resonances identified are in agreement with previous works.[59,60]

phenomenon is in agreement with the strong Ostwald ripening effects that were observed during the NC growth. Accordingly, we found that Ostwald ripening could be suppressed by reducing the concentration of ligands, as is evidenced by the narrow size distributions of the NCs that were obtained following the proposed strategy (Figure 3.5).

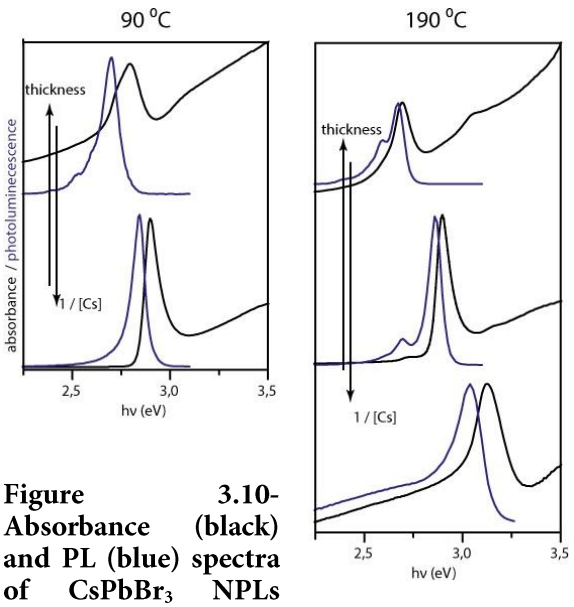

Figure 3.10- Absorbance (black) and PL (blue) spectra of $CsPbBr_3$ NPLs synthesized at 90 and 190 C

Secondly, it has now been well established that aliphatic ammonium (RNH_3^+) ions can compete with Cs^+ for lattice sites and promote the formation of hybrid layered structures of general formula $[RNH_3]_2[CsPbBr_3]_{n-1}PbBr_4$ (in which n denotes the number of $PbBr_6$ octahedra along the thickness).[53,54] Indeed, the results in terms of shape control showed that NPLs could be obtained by increasing the $[RNH_3^+]/[Cs^+]$ ratio. Following this concept, and considering the temperature profile of $[RNH_3^+]$, pure NPL samples could be synthesized even at high temperatures (190 °C) by simply adjusting the $[Cs^+]$ accordingly (see Figure 3.10 and table 3.2). Moreover, such two-dimensional hybrid systems could also be synthesized in the presence of other Brønsted acids. Notably, when the acid strength increased (benzylsulfonic >> hexanoic > oleic acid) lower amounts of acid were needed to start forming such structures (see Figure 3.11).

iii. Mechanistic insights.

The solubility of $PbBr_2$ in this system can be interpreted on the basis of the dissociation of the oleylammonium oleate salt, followed by the solvation of $PbBr_2$. In addition to thermal effects, the dissociation of acid base salts in aprotic solvents can also occur *via* homoconjugation:

$$BH^+ \dots A^- + B \leftrightarrow (BH^+ \dots B)A^- \qquad \text{(eq. 2)}$$

This is a mechanism that typically shows high equilibrium constants for amine-based systems.[52,55–57]

The interpretation of the oleylammonium oleate salt as an inactive specie is supported by the results in terms of phase transformation (Figure 3.8f-h). In short, the transformation of $CsPbBr_3$ into Cs_4PbBr_6 is driven by the ability of the ligand mixture to solubilize $PbBr_2$, which is the by-product of this transformation (similarly, other substances can also induce this transformation, see appendix A3.7). It was demonstrated that the kinetics of this reaction is modulated by the relative amounts of acid and base (Figure 3.8f). The transformation does not occur when acid is

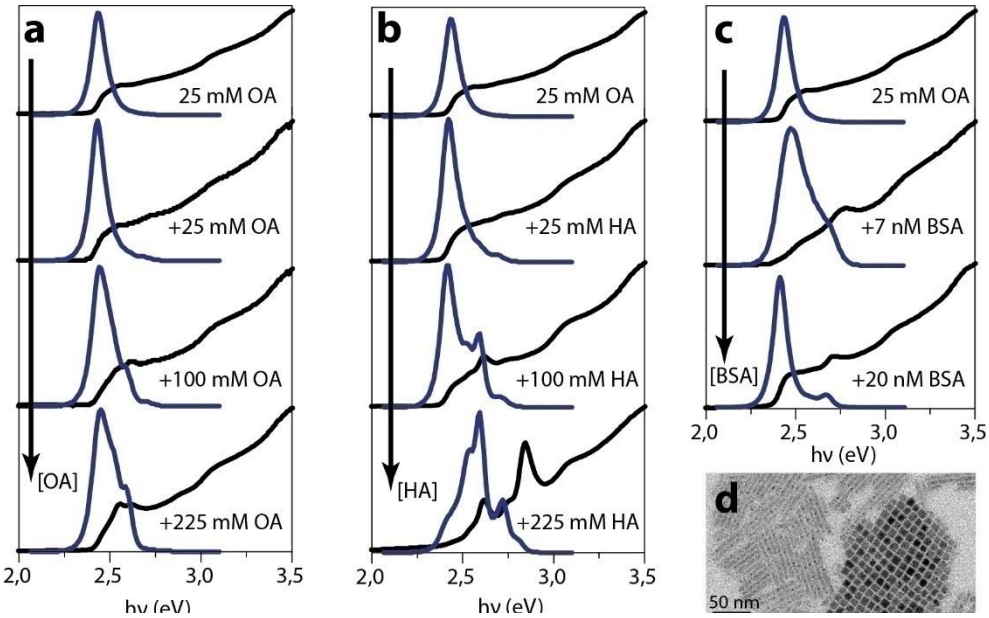

Figure 3.11 Absorbance (black) and photoluminescence (blue) spectra of nanocrystals synthesized with increasing amounts of (a) oleic acid (OA), (b) hexanoic acid (HA) and (c) benzylsulfonic acid (BSA). With increasing amounts of acid, extra peaks appear in the absorption and photoluminescence spectra of the nanocrystal product, attributed to the presence of nanoplatelets (deduced from peak position and, at high intensities, the narrow width of these peaks can be observed in agreement with what is expected from a two-dimensional semiconducting system). (d) TEM image of nanocrystals (cubes + stripes) obtained in presence of BSA.

absent, but it is found to be completed in a few minutes when the amount of acid is ca. 10% mol of that of the amine. However, increasing the concentration of acid any further slows down the transformation until it does not proceed again. Therefore, at room temperature, a 1 : 1 mol. mixture of oleylamine and oleic acid, which mainly exists in the salt form, gelates in the absence of a solvent. However, when an excess of base is present, it can dissociate into ionic species which, in turn, can dissolve $PbBr_2$ and drive the transformation.

Furthermore, it was found that $PbBr_2$ (1 equivalent) can be dissolved at mild temperatures (ca. 80-100 °C) when a minimum amount of 0.5 eq. of stearic acid and an excess of amine ligands (4-5 eq.) are present (here, octadecylamine and stearic acid were used due to their high purity), which is likely a result of the partial dissociation of $PbBr_2$:

$$2PbBr_2 + BH^+ \dots A^- + xB \rightarrow PbBr_3^-.BH^+ + PbBr^+.A^- + xB$$

(eq. 3)

Note that the presence of $PbBr_3^-$ species has also been predicted to precede the formation of lead halide perovskite crystals in other aprotic solvents.[58]

The results in terms of phase control (Figure 3.8c-e) demonstrate that the NCs tend to crystallize in the lead-poor Cs_4PbBr_6 phase when there is a large excess of both ligands present. Under such conditions, a full dissociation of the lead salt into lead oleate and oleylammonium bromide is likely to occur:

$$PbBr_2 + 2(BH^+ \dots B)A^- \rightarrow Pb.A_2 + 2(BH^+ \dots Br^-) + 2B$$

(eq. 4)

This system allows a greater degree of freedom, than the one described by eq. 2 with respect to possible outcomes upon the injection of Cs^+ ions. For instance, the reaction of an alkylammonium bromide with Cs^+ in the same ligand mixture results in the formation of CsBr NCs (Figure 3.12). The two extreme situations illustrated in eq. 3 and eq. 4 can thus explain the results in terms of ligand mediated phase

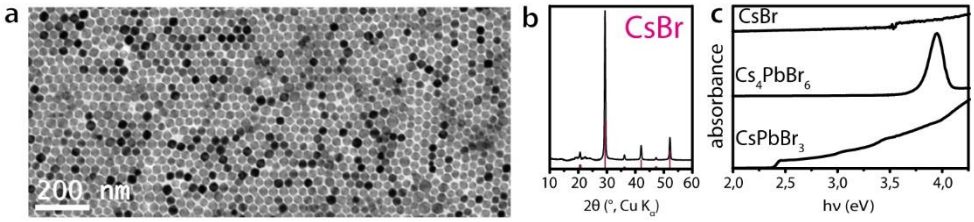

Figure 3.12 CsBr nanocrystals could be synthesized by reacting a tetralkylammonium bromide (DDAB) with Cs-oleate at 150 ^{0}C for 5 minutes in the presence of oleylamine. (a) TEM image and (b) XRD pattern (ICSD 98-005-3848) of CsBr nanocrystals. (c) absorbance spectra of CsBr, Cs_4PbBr_6 and $CsPbBr_3$ nanocrystals

control. Again, given the temperature profile of the acid base-equilibrium, a system described by eq. 4 should shift to the one described by eq. 3 when the temperature is increased. Indeed, we could find a ligand concentration that yields Cs_4PbBr_6 NCs at a low temperature (165 ^{o}C), and $CsPbBr_3$ NCs at a high temperatures (220 ^{o}C, Figure 3.8c).

iv. Extension to other halide systems

Most of the findings reported herein were also found to be valid for the Cl and I systems. For instance, $PbCl_2$ and PbI_2 also exhibit inverse solubility in this binary ligand system, and the re-precipitation temperatures follow a similar trend to that found for $PbBr_2$ (see Figure A3.8 of the appendix). Furthermore, $CsPbX_3$ NCs, Cs_4PbX_6 NCs and $(RNH_3)_2PbX_4$ nanosheets (X = Cl, I) could also be synthesized following the same strategies presented here for the phase and shape control of bromides (see Figures A3.9 and A3.10). Unfortunately, for the Cl and I cases, due to the poorer solubility of $PbCl_2$ and the lower re-precipitation temperature of PbI_2 in this binary ligand system, I could not reproduce the low ligand concentration conditions which had enabled me to synthesize $CsPbBr_3$ nanocubes with narrow size distributions.

Figure 3.13 Illustration summarizing size and shape control of $CsPbBr_3$ NCs

3.5 CONCLUSION

In this work, it was shown how the acid-base interactions within a ligand system that consists of aliphatic primary amines and carboxylic acids affect the synthesis and transformation of cesium lead bromide nanocrystals in non-polar solvents. This allowed me to not only achieve precise control over the size, shape and phase of the nanocrystals but also to understand the solubility behavior of $PbBr_2$ in this system. In addition, many of the findings reported herein were also found to be valid for the Cl and I systems. Furthermore, one should be able to extend these observations to non-protic polar solvents such as dimethylformamide, a commonly used solvent in the synthesis of lead halide perovskites, which is known to self-decompose into dimethylamine and formic acid[12] and is able to sustain the growth of perovskite single crystals via inverse solubility. Finally, the fact that this binary ligand system is able to dissolve $CsPbX_3$ nanocrystals and cannot provide good surface passivation should prompt further studies into other ligand systems.

3.6 OUTLOOK

The growth of lead halide perovskite thin-films and single-crystals is typically performed in the presence of R=O bases as is previously mentioned in section 3.2iii. However, the use of such compounds in the synthesis of nanocrystals has not yet been explored. Here, it was found that $PbBr_2$ can be dissolved in the presence of trioctylphosphine oxide, an organic ligand with high-boiling point which is commonly used in the synthesis of nanocrystals.

An amine- and ammonium-free route for the synthesis of $CsPbX_3$ (X=Br, I) nanocrystals was developed. In short, the PbX_2 precursor (0.1 mmol) was dissolved

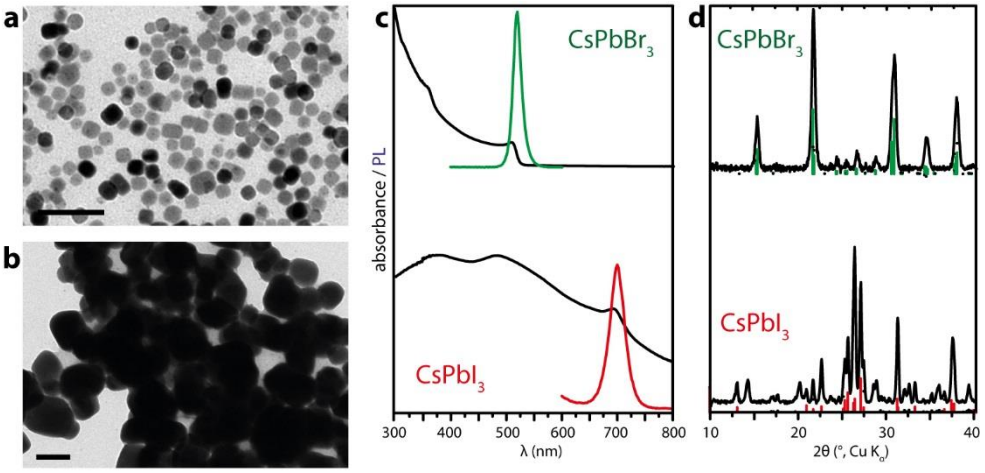

Figure 3.14 TEM images of (a) CsPbBr3 and (b) CsPbI3 NCs synthesized with TOPO (scale bars: 100 nm). Their (c) absorbance, PL spectra and (d) XRD patterns

in a mixture of TOPO (0.50 g) and OA (200 μL) in 1-octadecene (ODE, 4.0 mL) at ca. 100 °C. The mixture was heated to 150 °C, at which point 0.5 mL of a warm Cs-oleate solution (0.15 M, in ODE) was swiftly injected. The mixture was then immediately cooled down. These syntheses were performed in 20 mL vials and in air.

Results are summarized in Figure 3.14. In short, $CsPbBr_3$ nanocrystals of ca. 20 nm could be obtained (Figure 3.14a) but $CsPbI_3$ nanocrystals were ca. 70 nm. Both the absorption and photoluminescence spectra (Figure 3.14c) and the XRD patterns (Figure 3.14d) are in good agreement with the orthorhombic phases. Work is ongoing with regards to improving the size and size-distributions as well as understanding surface passivation.

3.7 References

(1) Rose, G. *De novis quibusdam fossilibus quae in montibus Uraliis inveniuntur*; 1839.

(2) Goldschmidt, V. Titanium pigment and process of producing same. US 1436164 A, 1922.

(3) Goldschmidt, V. *Nor. Videnkap, Oslo* **1927**.

(4) Roy, R. *J. Am. Ceram. Soc.* **1954**, *37*, 581.

(5) Bhalla, A. S. *Mater. Res. Innov.* **2000**, *4*, 3.

(6) Ardit, M. In *Perovskites and Related Mixed Oxides*; Wiley, 2016; 259.

(7) Uchino, K. *Sci. Technol. Adv. Mater.* **2015**, *16*, 46001.

(8) Murphy, D. W. *Phys. Rev. Lett.* **1987**, *58*, 1888.

(9) Von Hippel, A. *Rev. Mod. Phys.* **1950**, *22*, 221.

(10) Von Hippel, A. *Zeitschrift fur Phys.* **1952**, *173*, 158.

(11) Lines, M. E. *Principles and Applications of Ferroelectrics and Related Materials*; International series of monographs on physics; OUP Oxford, 1977.

(12) Cohen, R. E. *Nature* **1992**, *358*, 136.

(13) Wells, H. L. *Zeitschrift für Anorg. Chemie* **1893**, *3*, 195.

(14) MØLLER, C. *Nature* **1958**, *182*, 1436.

(15) Radhakrishna, S. *J. Lumin.* **1976**, *12–13*, 409.

(16) Ishihara, T. *Solid State Commun.* **1989**, *69*, 933.

(17) Papavassiliou, G. C. *Solid State Commun.* **1994**, *91*, 695.

(18) Era, M. *Synth. Met.* **1995**, *71*, 2013.

(19) Kagan, C. R. *Science* **1999**, *286*, 945.

(20) Nikl, M. *J. Lumin.* **1997**, *72–74*, 377.

(21) Kondo, S. *J. Phys. Soc. Japan* **2003**, *72*, 1789.

(22) Kojima, A. *J Am Chem Soc* **2009**, *131*, 6050.

(23) Park, N.-G. *Nat. Energy* **2016**, *1*, 16152.

(24) Yang, W. S. *Science* **2017**, *356*, 1376.

(25) Protesescu, L. *Nano Lett.* **2015**, *15*, 3692.

(26) Sutherland, B. R. *Nat. Photonics* **2016**, *10*, 295.

(27) Goldschmidt, V. M. *Naturwissenschaften* **1926**, *14*, 477.

(28) Travis, W. *Chem. Sci.* **2016**, *7*, 4548.

(29) Nedelcu, G. *Nano Lett.* **2015**, *15*, 5635.

(30) Van der Stam, W. *J. Am. Chem. Soc.* **2017**, *139*, 4087.

(31) Manser, J. S. *Chem. Rev.* **2016**, *116*, 12956.

(32) Wenger, B. *Nat. Commun.* **2017**, *8*, 590.

(33) Kang, J. *J. Phys. Chem. Lett.* **2017**, *8*, 489.

(34) Li, W.-F. *J. Phys. Condens. Matter* **2015**, *27*, 355801.
(35) Chen, Y. *Nat. Commun.* **2016**, *7*, 12253.
(36) Wang, T. *Energy Environ. Sci.* **2017**, *10*, 509.
(37) Huang, H. *ACS Energy Lett.* **2017**, *2*, 2071.
(38) Koscher, B. A. *J. Am. Chem. Soc.* **2017**, *139*, 6566.
(39) Xiao, Z. *Nat. Photonics* **2017**, *11*, 108.
(40) Yakunin, S. *Nat. Commun.* **2015**, *6*, 8056.
(41) Sun, S. *ACS Nano* **2016**, *10*, 3648.
(42) Koolyk, M. *Nanoscale* **2016**, *8*, 6403.
(43) Pan, A. *ACS Nano* **2016**, *10*, 7943.
(44) Bekenstein, Y. *J. Am. Chem. Soc.* **2015**, *137*, 16008.
(45) Sichert, J. A. *Nano Lett.* **2015**, *15*, 6521.
(46) Akkerman, Q. A. *J. Am. Chem. Soc.* **2016**, *138*, 1010.
(47) Shamsi, J. *J. Am. Chem. Soc.* **2016**, *138*, 77240.
(48) Dohner, E. R. *J. Am. Chem. Soc.* **2014**, *136*, 1718.
(49) Bohun, A. *Czechoslov. J. Phys. B* **1970**, *20*, 803.
(50) Liu, Z. *J. Am. Chem. Soc.* **2017**, *139*, 5309.
(51) Palazon, F. *Chem. Mater.* **2017**, *29*, 4167.
(52) Davis, M. M. *Acid-base behavior in aprotic organic solvents*; U.S. department of commerce, National Bureau of Standards, 1968.
(53) Ravi, V. K. *J. Phys. Chem. Lett.* **2017**, *8*, 4988.
(54) Weidman, M. C. *Chem. Mater.* **2017**, *29*, 5019.
(55) Maryott, A. A. J. *Res. Natl. Bur. Stand.* **1947**, 38, 527.
(56) Witschonke, C. R. *J. Am. Chem. Soc.* **1947**, *69*, 2472.
(57) Coetzee, J. F. *J. Am. Chem. Soc.* **1965**, *87*, 5005.
(58) Stevenson, J. *Chem. Mater.* **2017**, *29*, 2435.
(59) Moreels, I. *J. Am. Chem. Soc.* **2008**, *130*, 15081.
(60) Moreels, I. *ACS Nano* **2012**, *5*, 2004.

3.8 APPENDIX

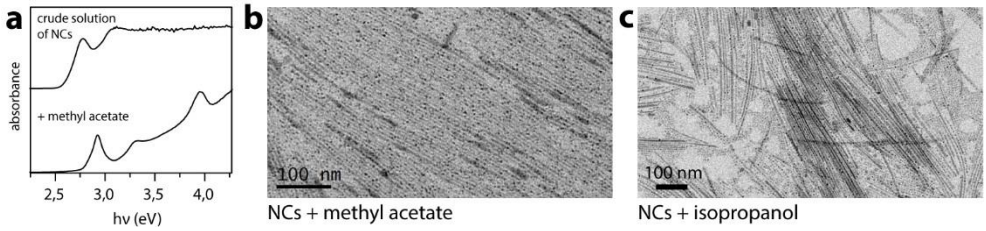

Figure A3.1 Effect of anti-solvents on $CsPbBr_3$ nanocrystals synthesized at 100 ^{o}C ([OlAm] = 0.25 M, [OA] = 0.025 M). (a) Absorbance spectra of the crude solution containing $CsPbBr_3$ nanocrystals (< 4.0 nm) and of the nanocrystals precipitated by adding methyl acetate. TEM images of nanocrystals precipitated with (b) methyl acetate and (c) isopropanol show the presence a large quantity of nanowires.

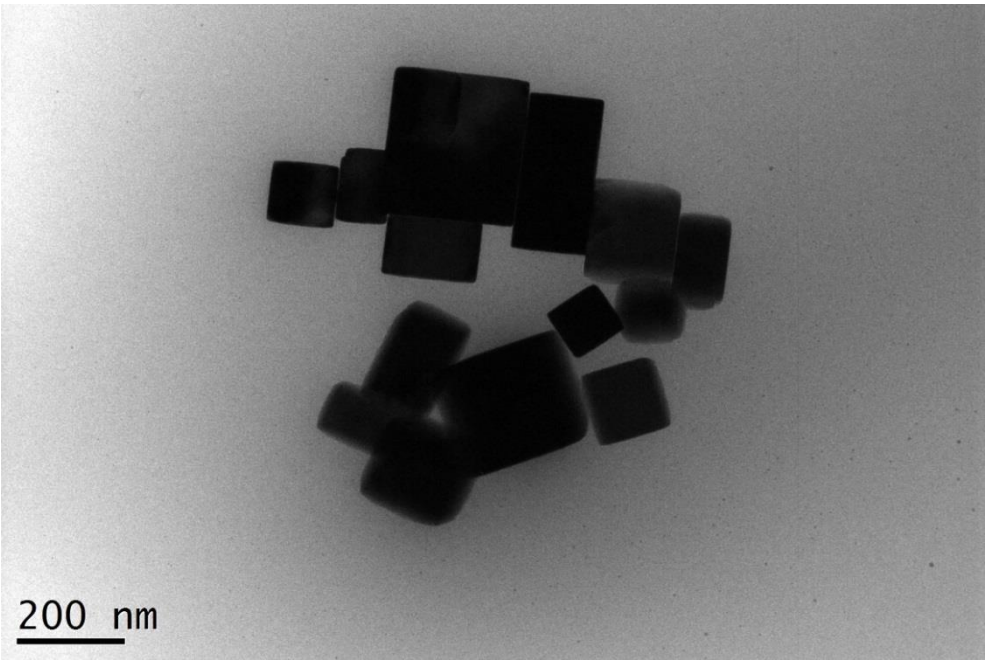

Figure A3.2 $CsPbBr_3$ nanocubes over 100 nm synthesized at 240 C with [OlAm] = 1.5 M, [OA] = 1.5 M and grown for 5 minutes

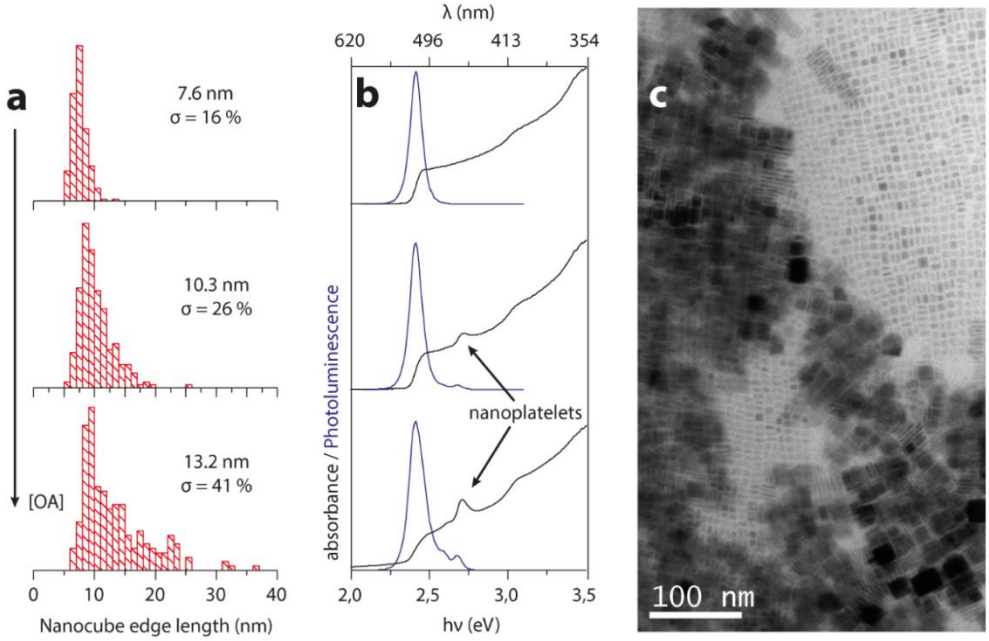

Figure A3.3 Effect of oleic acid concentration on the size and shape of $CsPbBr_3$ nanocrystals synthesized at 190 °C. (a) Size-distribution histograms and (b) optical spectra of nanocrystals synthesized with increasing concentrations of oleic acid ([OA] = 0.25, 0.50 and 1.00 M, [OlaM] = 0.25 M). (c) TEM image of nanocrystals synthesized with [OA] = 1.00M and [OlAm] = 0.25M, note the presence of nanoplatelets.

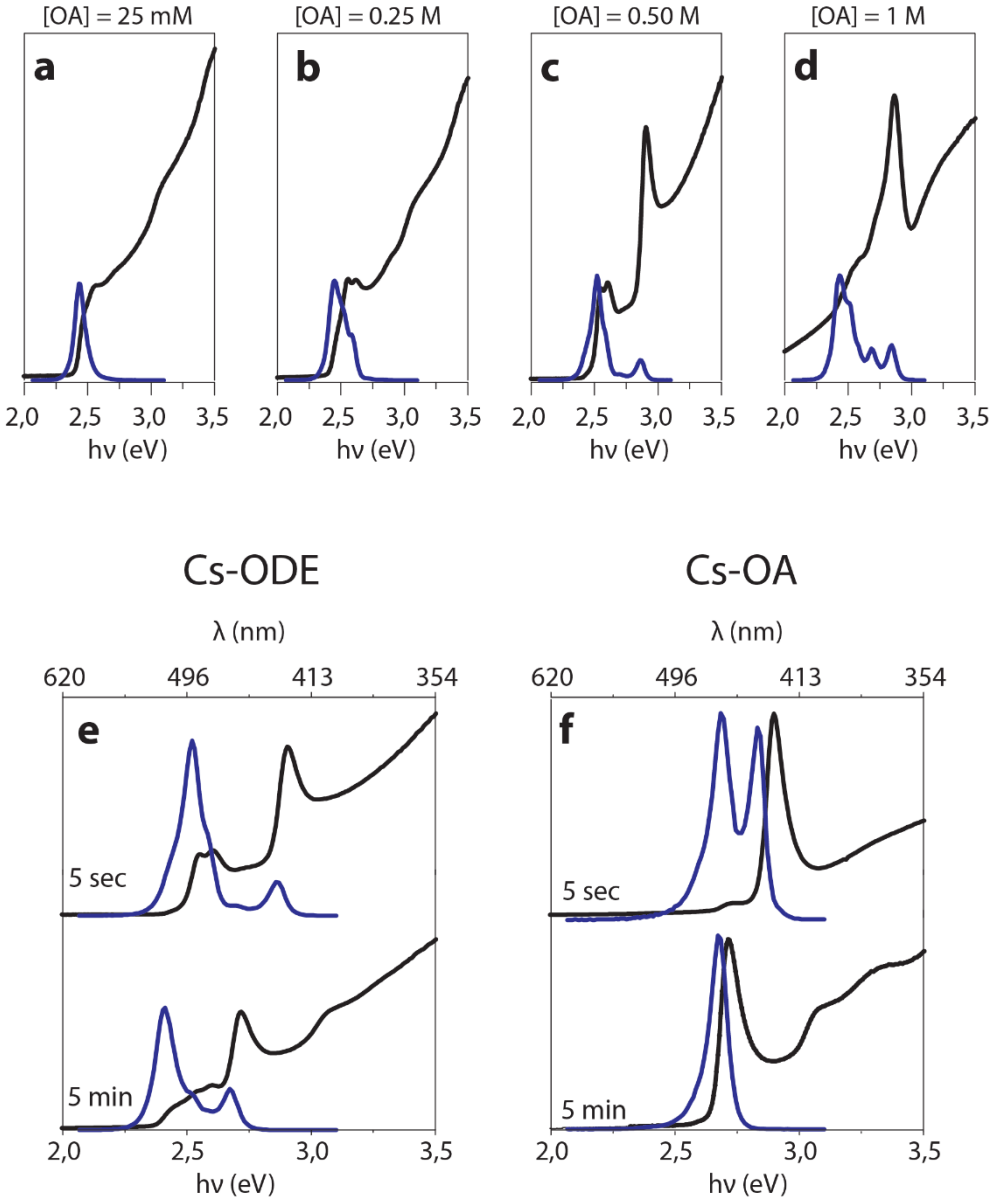

Figure A3.4 (a-d) absorption (black) and photoluminescence (blue) spectra of $CsPbBr_3$ nanocrystals synthesized for 5 s at 140 ^oC with increasing amounts of oleic acid ([OlAm]=0.25M) using Cs-oleate in ODE. (e-f) Absorption (black) and photoluminescence (blue) spectra of $CsPbBr_3$ nanocrystals synthesized at 140 ^oC for 5 secs and 5 min using Cs-ODE and Cs-OA, respectively, as a Cs-precursor

F

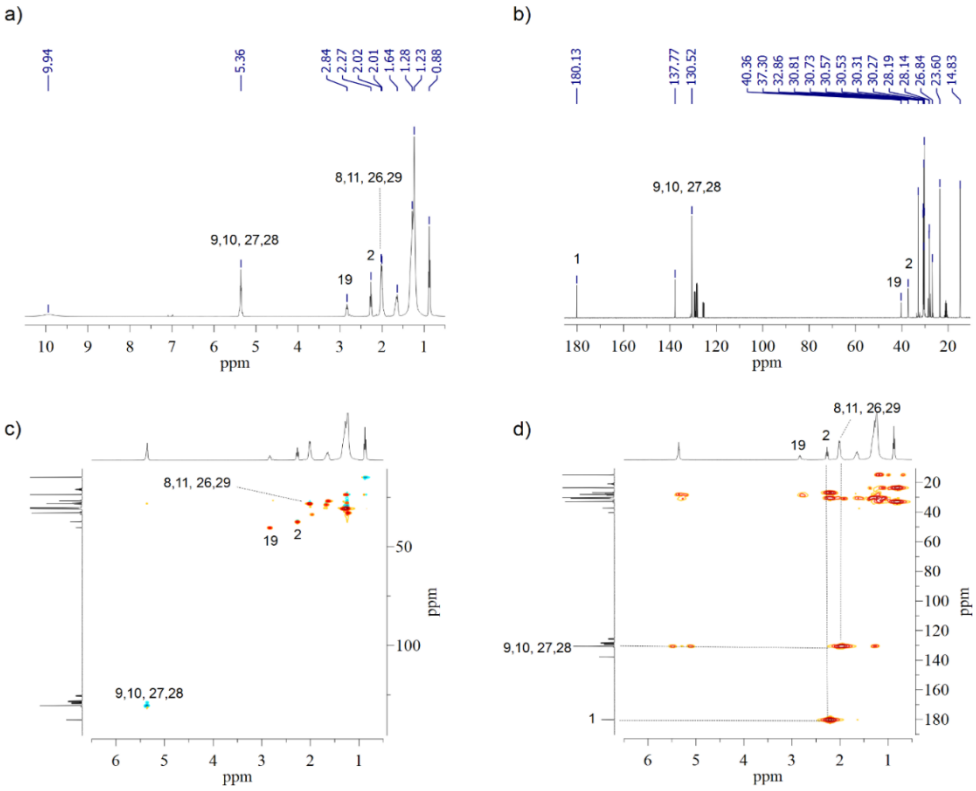

Figure A3.5 a) 1H, b) 13C, c) 1H-13C-HSQC edited and d) 1H-13C-HMBC NMR spectra of OlAm : OA solution in toluene-d8. Diagnostic signals have been embedded in the figures.

Table A3.1 Assignment of resonances

Assignment	^{1}H	J(Hz)		^{13}C
-	9.94	-	br s	-
9,10, 27 and 28	5.36	-	m	130.5
19	2.84	-	ps t	40.4
2	2.27	7.65	t	37.3
8, 11, 26 and 29	2.11-2.91	-	m	28.2 and 28.1
20	1.67	-	m	28.6
3	1.64	-	m	26.8
4-7,12-15, 21-25, 30-33	1.45-1.05	-	m	30.8-20.3
17 and 35	1.26	-	m	23.6
16 and 34	1.23	-	m	32.9
18 and 36	0.88	6.9	t	14.8
1	-	-	CO	180.1

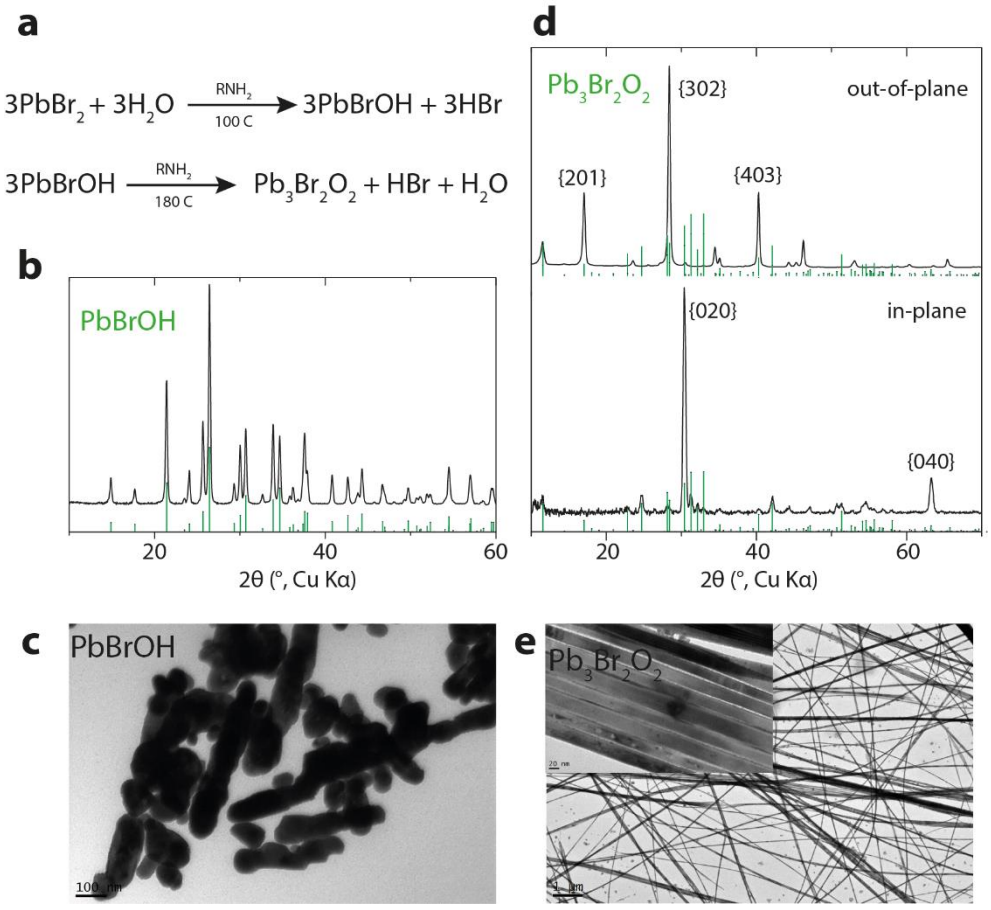

Figure A3.6 Heating $PbBr_2$ in air in the presence of oleylamine (RNH_2) yields (b,c) PbBrOH colloids at 100 °C and (d,e) $Pb_3Br_2O_2$ nanowires (elongated over the [100] direction) at 180 °C

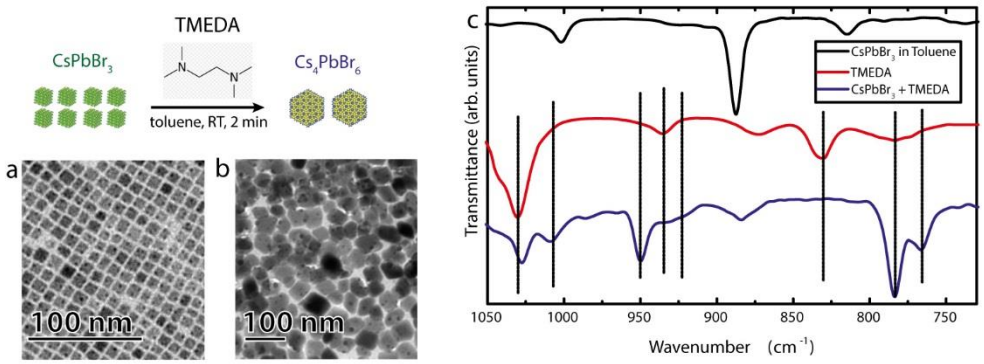

Figure A3.7 N,N,N',N'-Tetramethylethylenediamine (TMEDA) driven transformation of (a) $CsPbBr_3$ NCs into (b) Cs_4PbBr_6 NCs. (c)The FTIR spectrum of TMEDA treated nanocrystals shows characteristic peaks of TMEDA-$PbBr_2$ complexes

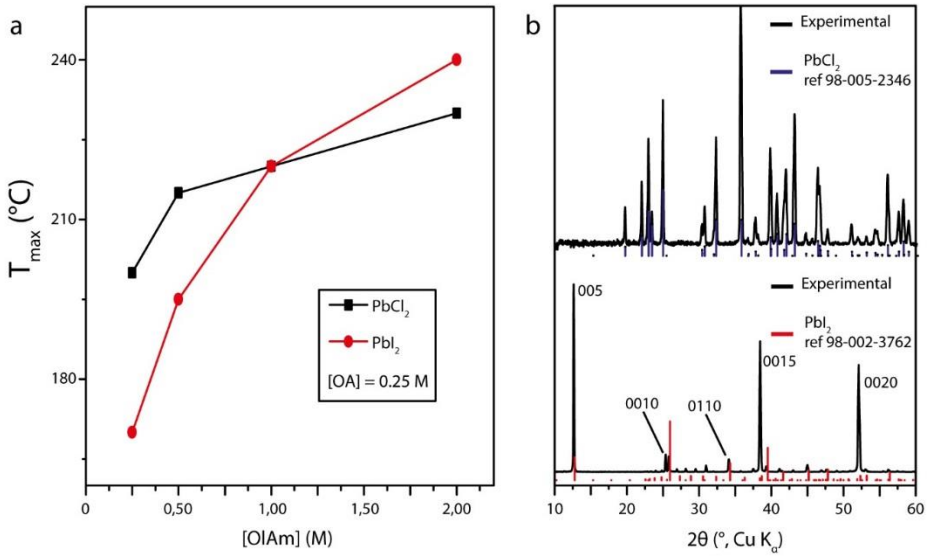

Figure A3.8 (a) Maximum reaction temperature T_{max} as a function of ligand concentration; at T_{max}, PbX_2 (X = Cl, I) precipitates from the reaction medium (33 mM of PbBr2 solution in 1-octadecene with [OA] set at a constant 250 mM), as confirmed by (b) x-ray diffraction.

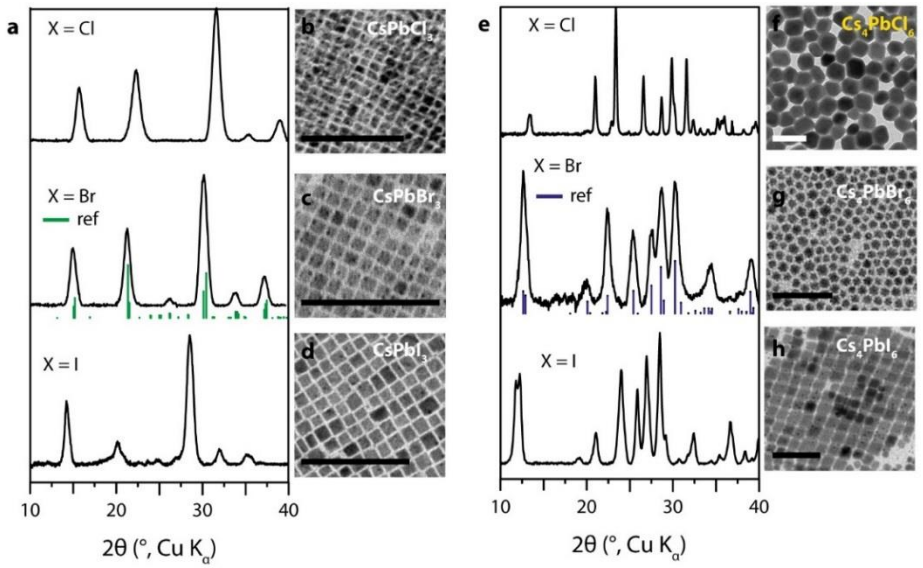

Figure A3.9 (a) x-ray diffraction patterns and (b-d) respective transmission electron images of $CsPbX_3$ (X = Cl, Br, I) nanocubes synthesized at 165 °C in the presence of [OlAm] = [OA] = 0.25 M. (e) x-ray diffraction patterns and (f-h) respective transmission electron images of Cs4PbX6 nanocrystals synthesized at 165 °C in the presence of [OlAm] = [OA] = 1.0 M (when X = Br, I) or 1.5 M (when X = Cl). All scale bars represent 100 nm.

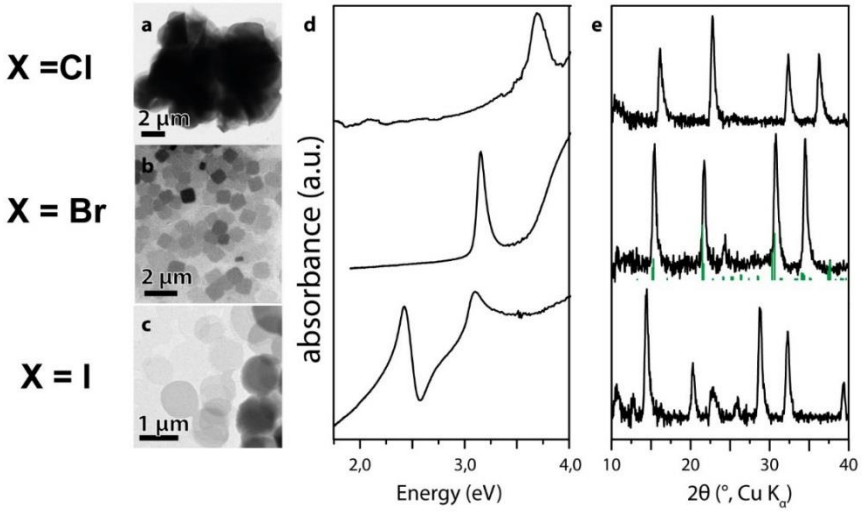

Figure 3.10 (a-c) transmission electron images, (d) absorbance spectra and (e) x-ray diffraction patterns of $(RNH_3)_2PbX_4$ nanosheets (green lines correspond to the $CsPbBr_3$ reference pattern) obtained by adding oleic acid to a hot solution of PbX_2 ([OlAm]=$[OA]_i$=0.25 M, $[OA]_i$ denotes the initial concentration of oleic acid).

4 Single-layer β-In_2Se_3 nanosheets

4.1 Introduction

Layered crystals consist of infinite two-dimensional slabs of a certain structure, which are stacked in a precise sequence and separated by a gap (see Figure 2.1). There is no electronic bonding between the layers and only weak attractive van der Waals forces keep the layers in close proximity. Due to their weak interlayer interactions, layered crystals typically exhibit low friction coefficients (i.e. the layers can easily slide) and in fact, they have been used as solid lubricants for decades.[1] Layered structures are also well known for their ability to accept ions (typically alkali metals) or molecules within their expandable gap. This process is typically reversible and allows not only to greatly tune the material's properties but also to exploit these structures for storage applications.[2,3] It is also worth noting that certain layered materials are important catalysts in the oil and synthetic chemical industries.[4]

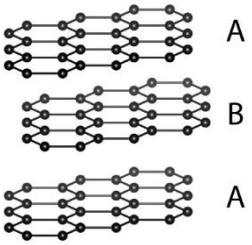

Figure 4.1 – The structure of Bernal stacked graphite (C)

Although many layered materials have long been known to be conductive and semiconducting,[4] it is only recently that these materials have gained attention with regards to electronic and photonic applications. The major breakthrough in this field occurred in 2004 with the isolation of a single layer of graphite (layered allotrope of carbon, structure depicted in Figure 4.1) known as "graphene".[5] Although single layer atomic films were long thought to be thermodynamically unstable, graphene is in fact very stable and possesses remarkable mechanical, thermal and electronic

properties. This discovery opened up new frontiers in experimental physics and paved the way for the exploration of a variety of layered materials down to the single-layer limit. Two-dimensional layered materials are currently the most researched topic in the field of solid-state physics, and one of the main goals of this field is to realize ultrathin, flexible and highly efficient electronic and photonic devices.

i. Layered structures

An overview of the various layered structures will be given in this section. For simplicity, the structures are classified according to their complexity in terms of their composition, as is shown in Figure 4.2. The vast majority of layered structures arise in compounds, while only a few light elements are known to crystallize in layered structures. These include carbon (graphite), (black) phosphorous, silicon and boron. However, it should be noted that the layered allotropes of silicon and boron are still difficult to prepare and have never been observed in the form of bulk crystals.[6,7]

Graphite (C) can be considered the most simple layered structure. Each layer is only one atom thick and is only composed of carbon atoms which are arranged in a perfect honeycomb lattice (sp^2 bonding configuration). Remarkably, the structure of layered boron nitride (h-BN) is identical to that of graphite. Black phosphorous also forms a similar honeycomb lattice, but it is not planar. In this case, each layer is two atoms thick and the atoms are arranged in an armchair configuration (sp^3 hybridization). Neither silicene (single layer Si) nor borophene (single layer B) are planar either.

In layered compounds, each layer is typically a few atoms thick; the exact thickness depends on the structure. A considerable number of metal halides with the formula MX_2 or MX_3 crystallize in layered structures with three-atom thick layers. These compounds can be subdivided according to the nature of the metal halide bond: the more ionic compounds crystallize in the $CdCl_2$ or $CrCl_3$ structures, whereas the more covalent ones prefer CdI_2 or BiI_3 arrangements.[8] Many metal chalcogenides also adopt layered structures and can be classified according to the thickness of their layers. Chalcogenides with group-IV metals (e.g. GeS) adopt a two-atom thick layer structure, similar to that of phosphorene, while transition metal dichalcogenides (e.g.

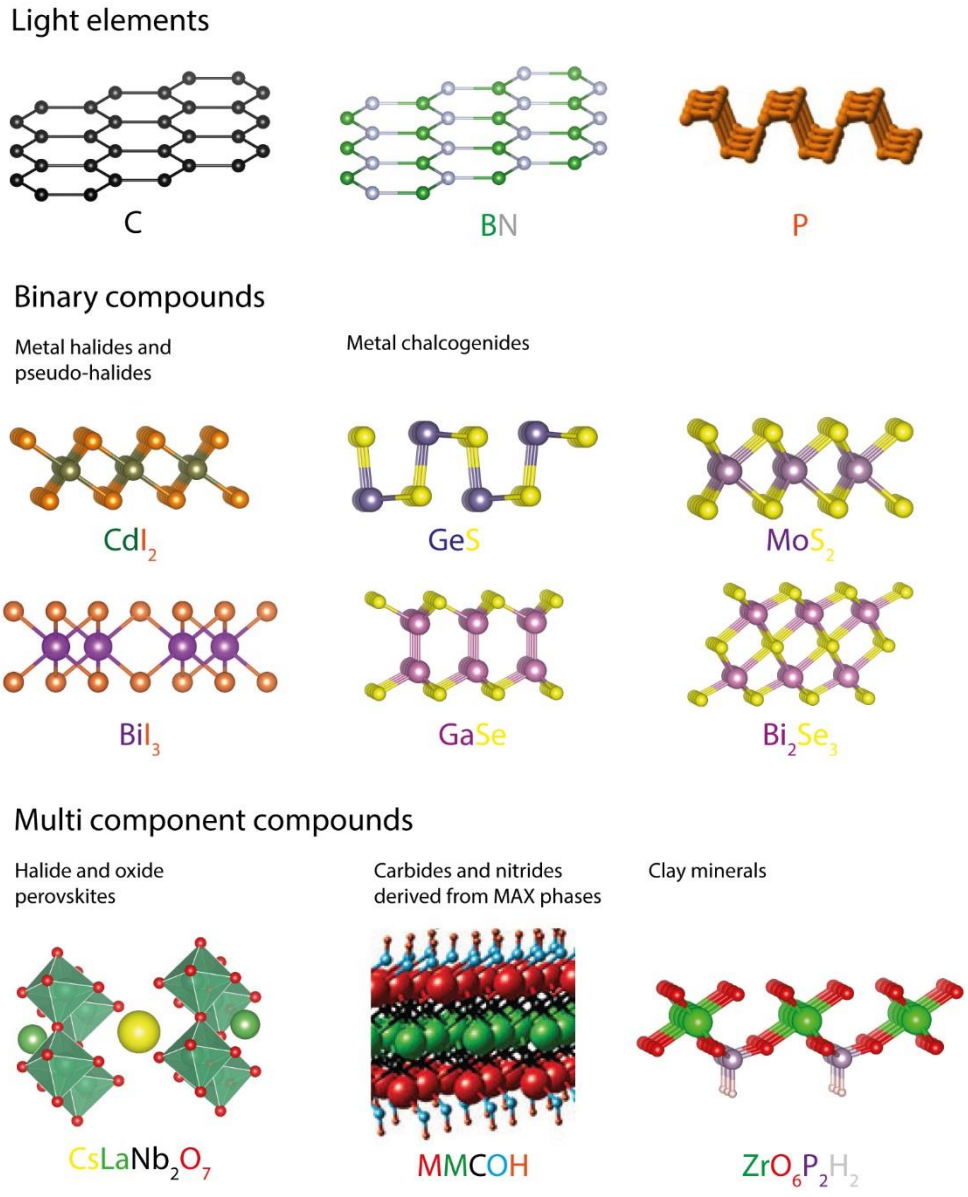

Figure 4.2 Important layered structures in material science, classified by their complexity in terms of composition. One important class that is not depicted is layered oxypnictides (muti component).

MoS_2) are three-atom thick and have similar structures to metal halides. Chalcogenides with group III metals such as Al, Ga and In can form four-atom thick layers that comprise a metal-metal bond (e.g. GaSe). In this case the metal atoms are in an unusual subvalent oxidation state of +2 and in fact they have been rarely observed. More often, these compounds form layered crystals of the tetradymite structure with five-atom thick layers in order to generate closed-shell configurations (e.g. In_2Se_3, Bi_2Te_3). Distorted versions of the tetradymite structure also exist and include stibnite (Sb_2S_3) and orpiment (As_2X_3).[9] Note that the layered chalcogenides typically exhibit a rich polytypism, as is exemplified in Figure 4.3 for transition metal dichalcogenides.

Layered structures composed of three or more elements also exist. For instance, several layered perovskites are well known and include the Ruddleson-Popper (Sr_2RuO_4), Aurivillius (Bi_3TiNbO_9) and Dion-Jacobson ($CsLaNb_2O_7$) phases. Although they are considered layered structures, the layers are not separated by a gap but rather by a motif. Layered perovskite structures in which the layers are separated by a gap are represented by the hybrid organic – inorganic structures which were presented in Chapter 3. Other important multi-element layered structures include the vast array of naturally occurring clay minerals or the so-called MXenes which encompass metal carbides and nitrides[10,11] Another important class is the compounds that crystallize in the tetragonal ZrCuSiAs structure which are composed of two different and more tightly bonded layers.[12,13]

ii. Two-dimensional electronic layered materials

Following the isolation graphene,[5] a panoply of layered systems were investigated in the few and single-layered regimes. Many of these systems transpired to be so fascinating that they quickly became popular platforms for physicists to perform experiments on. In particular, some were found to be of great interest for electronics and photonics, as will be highlighted in the following paragraphs.

Perhaps it is a fortuitous coincidence, but the first material to be isolated in the form of a single layer is still, to date, the most remarkable one. Graphene (single layer

graphite) is a transparent semimetal with extremely high charge carrier mobilities that can be used as a two-dimensional electrical contact.[5] Arguably, its most remarkable feature is that it exhibits Dirac-type fermions i.e. in graphene, charge carriers are massless and behave like photons, and new types of electron switches based on this property have been developed.[14,1516] Furthermore, this discovery also lead to the development of novel nano-engineered two-dimensional lattices[17,18]. It should be noted that many of graphene's incredible properties can only be fully explored when it is placed on top of (or sandwiched by) a lattice matching substrate. For this purpose, hexagonal boron nitride (hBN) is typically used.[19] Although it is isostructural to graphene, hBN is a wide-gap insulator with excellent dielectric properties even in the few layer regime, and is typically used in the fabrication of high-quality field effect transistors.[20]

Although the initial motivation behind the isolation of graphene was to use it as a transistor channel,[5] in reality it is too conductive for such a purpose. Therefore, many efforts were put into identifying layered semiconductors that could be compatible with graphene and hBN, i.e. ones that have a similar honeycomb lattice. All the layered metal chalcogenides fulfil this structural requirement and many of them are actually semiconductive.[21] In particular, molybdenum and tungsten dichalcogenides single layers have direct band-gaps in the near-infrared to the visible region and have been extensively investigated over the past few years for electronic and photonic applications.[22–24] Although they are less studied, many layered chalcogenides of post transition met als are also semiconductive. They are mostly indirect-gap semiconductors, but they still exhibit interesting properties. For instance, MX compounds such as GaSe are efficient non-linear emission sources[25] while M_2X_3 compounds typically outperform their transition metal counterparts as photoconductors[26].

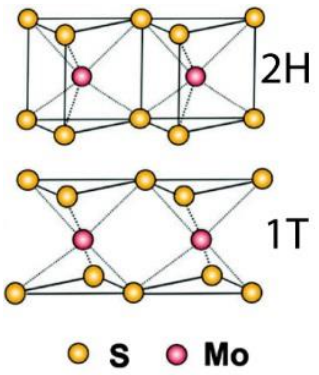

Figure 4.3 structures of (semiconducting)2H- and (metallic)1T-MoS_2

iii. Two-dimensional layered materials: fabrication methods

The most simple way to isolate ultra-thin flakes of layered materials is through the mechanical exfoliation (repeated peeling) of small mesas using scotch tape.[5] This approach allows one to obtain high-quality samples, but in small yields and with no control over morphology. Chemical exfoliation (extreme case of intercalation) in liquid phase is another popular route and it allows to obtain colloidal dispersions of ultra-thin flakes which can be used as inks. Nevertheless, it should be noted that this approach typically requires aggressive sonication steps that damage the structure of the flakes, it often involves using toxic reagents, the dispersions suffer from re-aggregation and, furthermore, it also doesn't provide much control over the morphology of the flakes.[27] A much improved top-down strategy to obtain stable dispersions of two-dimensional layered materials is to modify the starting material in such a way that it spontaneously dissolves in polar solvents.[28] This is a very elegant route but comes at the expense of changing the material's properties and its suitability for large-area flakes (> 100x100 nm) as not yet been demonstrated.

In terms of bottom-up approaches, physical/chemical vapor deposition methods have been demonstrated and are now routinely used to synthesize highly-crystalline single layer flakes of graphene and many layered chalcogenides.[29,30] Many efforts are being put into achieving control of these growth processes on different substrates and to scale them up to the wafer size. Nevertheless, note that this strategy relies on costly high temperature processes. In this regard, the bottom-up synthesis in liquid phase is also of interest. Colloidal chemistry offers a low-temperature route to creating nanomaterials with unique morphological control and it has been proven to be a valid alternative for growing two-dimensional materials for use in solution-processed electronic devices.[31] In the past few years, colloidal methods have been successfully employed to grow two-dimensional crystals of both non-layered[32–35] and layered structures such as transition metal dichalcogenides[36,37] and the monochalcogenides of iron[38], germanium[39] and tin[40]. Different strategies have been reported for the colloidal growth of two-dimensional nanocrystals, including slow growth kinetics[36] and the presence of chlorine containing compounds.[33,41] Short

ligands have been proposed too,[32,35] but their use is limited by their low boiling points.

iv. Goals

To date, the amount of literature on colloidal synthesis of layered chalcogenides is low, particularly in comparison to the number of publications on vapor deposited layered chalcogenides, suggesting that it remains challenging. In this context, this work addresses the colloidal synthesis of indium selenide (β-In_2Se_3) nanosheets. The choice of this particular system was based upon several factors. The first is its novelty: up to now, apart from a few works on In_xSe_y nanostructures,[42–45] the colloidal synthesis of layered indium selenide has yet to be clearly demonstrated. Secondly, the indium selenide system is quite interesting from a structural point of view as it can form several semiconducting layered phases with band-gaps around 1.3 eV. Furthermore, mechanically exfoliated and vapor grown thin-flakes of this material have shown interesting electronic and optoelectronic characteristics, and these reports could also serve as quality benchmarks.[46–53] Given the many possible structures for this material, a brief review of their properties and phase transitions will be given in the next section.

v. Structures and properties of In_2Se_3

This section describes the properties of, and phase transitions in, the In_2Se_3 compound. It should be noted that the indium selenide system can also crystallize in a layered phase with a InSe composition but this is beyond the scope of this work. Readers interested in the two-dimensional InSe system are encouraged to check the works cited in references 46 to 50.

The basic structures of several $A^{III}{}_2B^{VI}{}_3$ compounds are the zincblende and wurtzite lattices which have tetrahedral bonding. Given the stoichiometry, in order to satisfy the octet rule for sp^3 hydbridization, one-third of the cationic (A) sites must be vacant and are often found to be randomly distributed.[54] In_2Se_3 belongs to this class of

compounds and it exhibits a rich polymorphism. The phase transitions between the main phases can be described as follows

$$\alpha \overset{200^{\circ}C}{\longleftrightarrow} \beta \overset{350^{\circ}C}{\longrightarrow} \gamma \overset{650^{\circ}C}{\longleftrightarrow} \alpha$$

The γ-phase is typically obtained when the synthesis is conducted at low-temperatures,[55–58] i.e. under 550˚C. It grows in a columnar mode and crystalizes in the enantiomorphous space groups $P6_1$ or $P6_5$, meaning that twin crystals can be obtained. In short, it consists of two interconnected frameworks in the form of screws that build up along the 6_1 axis forming a defect ZnS wurtzite arrangement [57] One is formed by corner-sharing $InSe_4$ tetrahedra and the other by edge-sharing $InSe_5$ bipyramids. The screws of one type are interlinked only by those of the other type and vice versa, as is shown in figure 4.4.The structural vacancies are also ordered in screw-form along the c-axis and, in fact, this phase is also known as the *vacancy ordered in screw form* (VOSF) phase.[58]

This phase is semiconductive and has a reported optical (direct) band-gap of ca. 1.7-1.9 eV.[58–60] A photoluminescence peak at 2.11 eV was observed at 11 K.[61] It is typically n-doped but electrically it is quite insulative (resistivities of 10^6 to 10^9 ohm.cm depending on the annealing temperature).[59–62] Its poor electrical behavior is probably a result of a low density of carriers ($<10^{13}$ cm^{-3}) combined with moderate carrier mobilities (20-60 $cm^2.V^{-1}s^{-1}$). This material was found to be prone to surface oxidation and can form a thin conductive In_2O_3 layer.[61]

A layered phase arises from the aggregation of the structural vacancies on one closely packed plane, which forms an interlayer gap**.** According to previous research, several layered polymorphs might exist. The identification of these polymorphs, as well as of their crystal structures, physical properties and stability, remain controversial. This seems to be due to several factors, including the various synthesis methods employed, the poor structural characterization of the samples, the coexistence of several polymorphs –which often have similar structures - in samples, the presence of impurities and the lack of a consistent nomenclature to denote

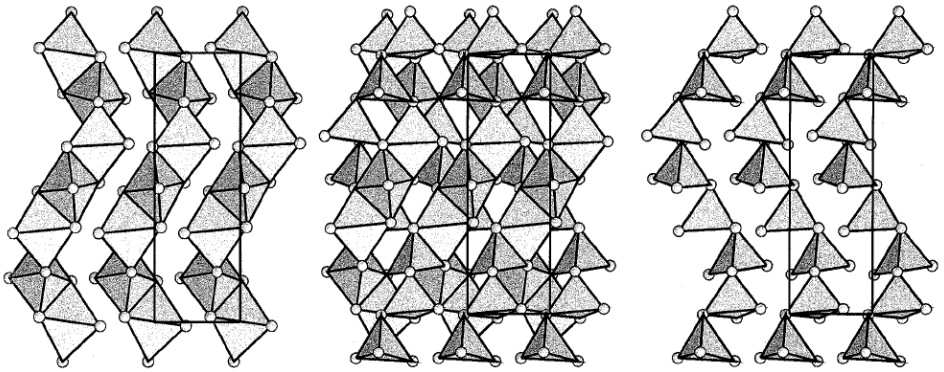

Figure 4.4 – (center) The structure of γ-In_2Se_3 consists of two interlinked frameworks with the form of screws. The 3D framework is formed of (left)edge-sharing $InSe_5$ trigonal bipyramids and (right) corner-sharing $InSe_4$ tetrahedra (re-printed from Ref. 57).

them.[63,64] Although it is often stated that two major layered polymorphs, denoted by α and β, exist, some authors suggest that only one layered structure exists and is prone to structural distortions.[9,64–66]

The layered structure consists of hexagonal Se-In-Se-In-Se quintuple layers that are separated by a van der Waals gap, and these layers are often stacked in an ABC sequence (rhombohedral). Various models have been proposed to describe the structure of the quintuple layers (see Figure 4.8 of section 4.3). These models differ in the coordination of the indium atoms (tetrahedral, octahedral or mixed) and in the stacking sequence of the five atomic layers (wurtzite or zincblende). Note that a tetradymite-like structure is obtained when all the indium atoms are octahedrally coordinated.

A layered phase is obtained by conducting the synthesis above 550-650 °C and is typically denoted by α.[56,58,67] Bulk α-In_2Se_3 is a semiconductor with an optical band-gap of ca. 1.3 eV, the nature of which is still controversial.[51,58,68] In this material, an insulator to metal transition was reported to occur upon cooling to -73 °C without any structural changes.[56] On the other hand, upon heating (pressurizing) to 200 °C (0.7 GPa), a small lattice contraction (< 1%) was observed. The contracted structure is denoted by β, and has a similar band-gap to α.[56,59,67,69–71] Although it is not clear if

the lattice contraction is accompanied by other structural changes, abrupt changes in the electrical properties of the material were reported. In bulk, the transition was found to be reversible and was accompanied by an important decrease in the electrical conductivity.[71] However, the complete opposite was observed in thin-lakes.[72] This illustrates the ongoing debate regarding the possible existence of more than one layered phases in this system.

4.2 METHODS

Materials. Indium (III) chloride ($InCl_3$, 99.999%), indium (III) bromide ($InBr_3$, 99.999%), indium (III) iodide (InI_3, 99.998%), selenourea (98%), dicyandiamide (99%), cyanamide (99%), hexane (95%), toluene (99.8%), 1-octadecene (90%), diethyl ether (99.7%), methanol (99.8%) and N,N-dimethylformamide (DMF, 99.8%) were purchased from Sigma-Aldrich and used without any further purification. Oleylamine (80-90%) was purchased from Acros Organics and filtered through a 0.45 μm PTFE filter before use.

Synthesis of 900 nm In_2Se_3 nanosheets via double injection procedure. All synthesis procedures were undertaken by employing standard Schlenk line techniques which were assisted by a nitrogen-filled glove box. $InCl_3$ (10 mg, 45 μmol), oleylamine (1.0 mL) and 1-octadecene (4.0 mL) were loaded into a 25 mL 3-neck round-bottomed flask equipped with a thermocouple and a magnetic stirrer and degassed at 100 °C for 1 hour. Thereafter, the temperature was raised to 215 °C under a dry nitrogen flow and a solution of selenourea (12 mg, 97 μmol) dissolved in DMF (160 μL) was injected. The initial colorless solution turned yellow then red then darkened within ca. 5-10 seconds, indicating the formation of In_xSe_y particles. Next, the mixture was quickly cooled to below 150 °C with an air-jet and quickly recovered to 200 °C at which point a solution of dicyandiamide (3.7 mg, 45 μmol) dissolved in DMF (200 μL) was injected to promote the growth of nanosheets. The reaction mixture was stirred for additional 10 minutes, and the heating mantle was removed to cool the reaction mixture. The final solution was dissolved in 15 mL of toluene and centrifuged at 1500 rpm for 20 minutes. The nanoparticle-rich supernatant was discarded and the nanosheet-rich precipitate was re-dispersed in ca. 5 mL of toluene, hexane or diethyl ether. Extra centrifugation rounds led to significant aggregation of the nanosheets.

Synthesis of In2Se3 nanosheets via a single-injection procedure.$InCl_3$ (10mg, 45μmol), oleylamine (1.0 mL) and 1-octadecene (4.0 mL) were loaded into a 25 mL 3-neck round-bottomed flask equipped with a thermocouple and a magnetic stirrer and degassed at 100 ˚C for 1 h. Thereafter, the temperature was raised to 215˚C (or

200˚C) under a dry nitrogen flow and a mixture of selenourea (12 mg, 97 μmol) and dicyandiamide (3.7 mg, 45 μmol) dissolved in DMF (200 μL) was injected. The reaction mixture was allowed to stir for additional 10 minutes and the heating mantle was removed to cool the reaction mixture. The work-up procedure was identical to the one reported for the 900 nm nanosheets.

X-Ray diffraction (XRD). Toluene solutions containing the nanosheets were washed twice with methanol (1:1 vol.). The nanosheets were re-dispersed in diethyl ether and dried to powder under vacuum. The XRD patterns of these powders were then acquired on a Rigaku SmartLab 9 kW diffractometer with the X-ray source operating at 40 kV and 150 mA. The instrument was equipped with a Cu source and a Göbel mirror (to obtain a parallel beam and suppress the Cu K_β radiation at 1.392 Å) and was used in the θ/2θ geometry can for data acquisition.

Thermogravimetric analysis (TGA). Analyses were conducted with a TGA Q500-TA instrument. As synthesized and methanol washed (using the same procedure as that of the XRD) samples were heated from 30 °C to 600 °C at a heating rate of 5 °C/min under nitrogen flow (50 mL/min).

Steady state UV-Vis-NIR extinction spectroscopy. Optical extinction spectra of dilute hexane dispersions of nanosheets and nanoparticles were recorded in quartz cuvettes with a 1 cm path-length by employing a Varian Cary 5000 UV-Vis-NIR absorption spectrophotometer. The extinction spectrum of the nanosheet dispersions suffered from a large scattering contribution. In order to overcome this, the absorption spectrum of the nanosheets was retrieved from their total transmission spectrum, which was recorded on a Perkin Elmer 1050 equipped with an integrating sphere. For this measurement, the nanosheet dispersion was spin-coated on top of a glass substrate and the reflectance of the sample was accounted for.

Elemental analysis. All elemental compositions were determined by energy dispersive X-ray spectroscopy (EDS). Concentrated colloidal solutions were drop-casted onto a Si substrate and measured in a high-resolution scanning electron

microscope (SEM), namely a JEOL JSM-7500F equipped with a cold field emission gun, and an Oxford X-Max 80 spectrometer (based on an 80 mm2 Si drift detector). Standardless quantification was achieved with Aztec Energy EDS software. Elemental analyses on single nanosheets were performed on a JEOL JEM-2200FS microscope equipped with a Bruker Quantax solid state detector. The composition of the nanosheets was also determined by inductively coupled plasma – optical emission spectroscopy (ICP-OES) analysis, which was performed on an aiCAP 6000 spectrometer (Thermo Scientific). The nanosheet solutions were digested in aqua regia overnight and diluted to a known volume prior to the measurements.

Transmission electron microscopy (TEM). Bright and dark field TEM images and selected-area electron diffraction (ED) patterns were acquired of samples, which were prepared by drop-casting colloidal solutions on carbon-coated 200 mesh copper grids, were acquired by using a JEOL JEM-1011 microscope (W filament) operating at an accelerating voltage of 100 kV. High-resolution TEM (HRTEM) images were acquired on a JEOL JEM-2200FS microscope, operating at 200 kV. The microscope is equipped with a CEOS objective corrector, allowing a resolution below 0.9 angstroms to be achieved, and an in-column filter (Ω-type), which was used to increase the contrast in the images by filtering around the elastically transmitted electrons. To obtain a top-view and side-view of the nanosheets, the samples were drop casted on ultrathin carbon and holey carbon coated copper grids, respectively.

Electron energy loss spectroscopy (EELS). Quantification of light elements as carbon and nitrogen from the ligands and solvent residuals was performed by using EELS in an FEI G2 transmission microscope equipped with an Enfinium spectrometer (Gatan, Inc.). The spectra were acquired using the diffraction mode, with a collection semiangle that was much larger than the convergence semiangle, in order to assure a highly accuracy quantification.

TEM simulations (Kindly performed by Dr. Giovanni Bertoni). Simulations of HRTEM images and ED patterns were performed using the xHREM software (HREM Research, Inc.) in the multislice approximation. For HRTEM, small values

of defocus (+25 nm) and spherical aberration (-0.03 mm) were used, as determined from the experimental images, by following the suggestions from Bertoni et al.[73]

XRD simulations (Kindly performed by Dr. Cinzia Giannini). Atomistic models were used as input structural information to a Debye equation-based simulation program.[74] A crystal lattice made of (200×200×1) unit cells along the a, b, and c axes was described in the simulations. The XRD patterns were computed in the angular range of 10° -90° with a 0.04° step, selecting the $K_{\alpha1}$-$K_{\alpha2}$ Cu doublet as the radiation wavelength.

AFM topography. The sample was prepared by spin-coating a dilute toluene suspension on a silicon substrate and the topography measurement was performed with a Park XE-100 instrument.

Raman spectroscopy. The sample was prepared by drop-casting a concentrated suspension onto a silicon substrate. The measurements were performed with a Renishaw inVia confocal Raman microscope using an excitation wavelength of 514.5 nm with a 50× objective, and an incident power of ~0.4 mW on the samples.

Device fabrication and characterization (Kindly performed by Dr. Sedat Dogan). A dilute dispersion of nanosheets was spin-coated onto an Si substrate coated with 300 nm of a thermally grown oxide layer. The substrate was then washed with isopropanol and methanol. The electrodes were patterned with electron beam lithography, then 4/50 nm Ti/Au layers were thermally evaporated. The devices were measured with a probe station in a vacuum chamber. Time-dependent photo-response measurements were performed using a mechanical chopper to modulate the incident laser beam. The output current was allowed to pass through a pre-amplifier before being recorded with an oscilloscope. Here we define the rise (fall) time as the time elapsed between 10% (90%) and 90% (10%) of I_{max}. Detectivities were calculated considering the shot noise from the dark current as the main source of noise.

DFT calculations. DFT-D218 calculations were performed using the Perdew-Burke-Enzerhof functional, Martin-Trouillers norm-conserving pseudo potentials for all elements and the pwscf code.[75] 100 and 400 Ryd were used as cutoffs for the plane waves and charge density, respectively. A uniform 6x6x3 mesh was used for the Brillouin Zone sampling of a bulk model, which was obtained by expanding 1 layer over c to yield a multilayered crystal with AA stacking. The optimized lattice parameters of the hexagonal unit cell were a=3.96 Å and c/a = 2.36, which is consistent with previous calculations on In2Se3 crystals.[76] Periodic slab calculations with a vacuum gap of 15 Å were performed using a Monkhorst-Pack 6x6x1 k-point mesh. The frequency-dependent dielectric function was computed using the random-phase approximation, by employing the epsilon.x tool of pwscf. To indicate the imulation convergence, the static limit of the dielectric function was computed using uniform 6x6x1, 12x12x1 and 16x16x1 meshes, obtaining the values of 4.08, 3.83 and 3.78, respectively. Finally, we used the 16x16x1 mesh for calculation using an interband smearing factor of 0.3 eV. The absorption coefficient was computed as the average of the two dielectric tensor diagonal components, which are perpendicular to light propagation. Additionally, a rigid upshift of 0.7 eV was applied to the conduction bands, in order to match the onset of the absorption profile with that of the experimental data. Results were compared with GW data (GW stands for the product of the Green's function G and the screened electron-electron interaction W).

4.3 RESULTS AND DISCUSSION

In this work, is reported a low-temperature (ca. 200 °C) colloidal synthesis of β-In_2Se_3 nanosheets with monolayer thicknesses and tunable lateral sizes from ~300 nm to. ~900 nm, employing short aminonitriles (dicyandiamide or cyanamide) as shape controlling agent. The structure and the monolayer nature of the nanosheets were ascertained by comparing experimental diffraction patterns with simulations and side-view high-resolution transmission electron microscopy imaging. The β-In_2Se_3 nanosheets were found to be indirect band-gap semiconductors (E_g=1.55 eV) and single nanosheet photodetectors demonstrated fast and remarkably high photo-responsivity across the whole visible spectrum.

i. Aminonitriles as shape controlling agents

The reaction between indium (III) chloride and selenourea in a homogeneous liquid phase medium composed of oleylamine and 1-octadecene (solvent) was found to yield very different products depending on the reaction temperature (see Figure 4.5a-c). At 280° C, nanosheets in the form of truncated triangles with lateral sizes up to a few hundred nanometers were obtained. By decreasing the reaction temperature to 240 °C, similar objects were obtained. However, these samples were quite polydisperse in terms of lateral size and thickness, and they exhibited a screw-type growth that was in indicative of the γ-In_2Se_3 phase. Furthermore, under the transmission electron microscope, the nanosheets that were grown at 240 °C showed less contrast than the ones grown at 280 °C, suggesting that they are thinner objects. Therefore, in an attempt to obtain thinner sheets with a better uniformity in terms of thickness, the reaction temperature was further reduced. Interestingly, reducing the reaction temperature further (to 220 °C) only yielded nanocrystals of ca. 5 nm.

This observation led to the hypothesis that the two-dimensional growth was promoted by products deriving from the thermal decomposition of selenourea. Therefore, a thermogravimetric analysis of selenourea was performed in a nitrogen atmosphere (see Figure 4.5d). An important weight loss (ca. 40 %) at ca. 210 °C was

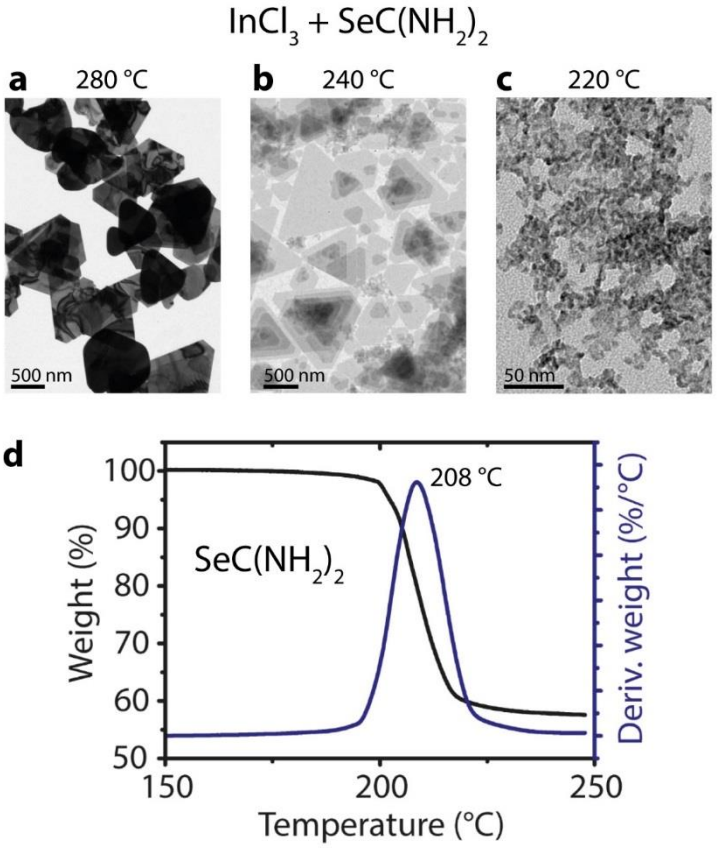

Figure 4.5 The reaction of $InCl_3$ with selenourea ($SeC(NH_2)_2$) in a solution of oleylamine and 1-octadecene leads to the formation of (a-b) micrometer large nanosheets at temperatures ≥ 240 °C. However, when they are conducted at (c) 220 °C, only small (ca. 5nm) nanocrystals are obtained. (d) Thermogravimetric analysis of selenourea under nitrogen flow

observed, which was ascribed to its decomposition into cyanamide ($NCNH_2$), carbon diselenide (CSe_2) and ammonia (NH_3)

$$2\,SeC(NH_2)_2 \xrightarrow{heat} NCNH_2 + CSe_{2\,(g)} + NH_{3\,(g)}$$

based on the known thermal decomposition pathway of thiourea.[77]

ii. The growth of In_2Se_3 nanosheets

A few previous works have exploited short molecules as shape/aggregation controlling agents for growing nanosheets of different materials.[32,33,35] Cyanamide is a non-volatile short chain amine, therefore it was hypothesized to be the two-dimensional growth promoter in this case. This hypothesis was confirmed, as the growth of nanosheets at temperatures under 220 °C could be achieved in presence of cyanamide or its dimer, dicyandiamide. In short, the low-temperature synthesis of nanosheets was demonstrated via a double injection procedure. The sheets were grown in two steps (Figure 4.6). First, indium selenide nanocrystals were formed by reacting $InCl_3$ with selenourea at 215 °C in the presence of oleylamine (Figure 4.6a).

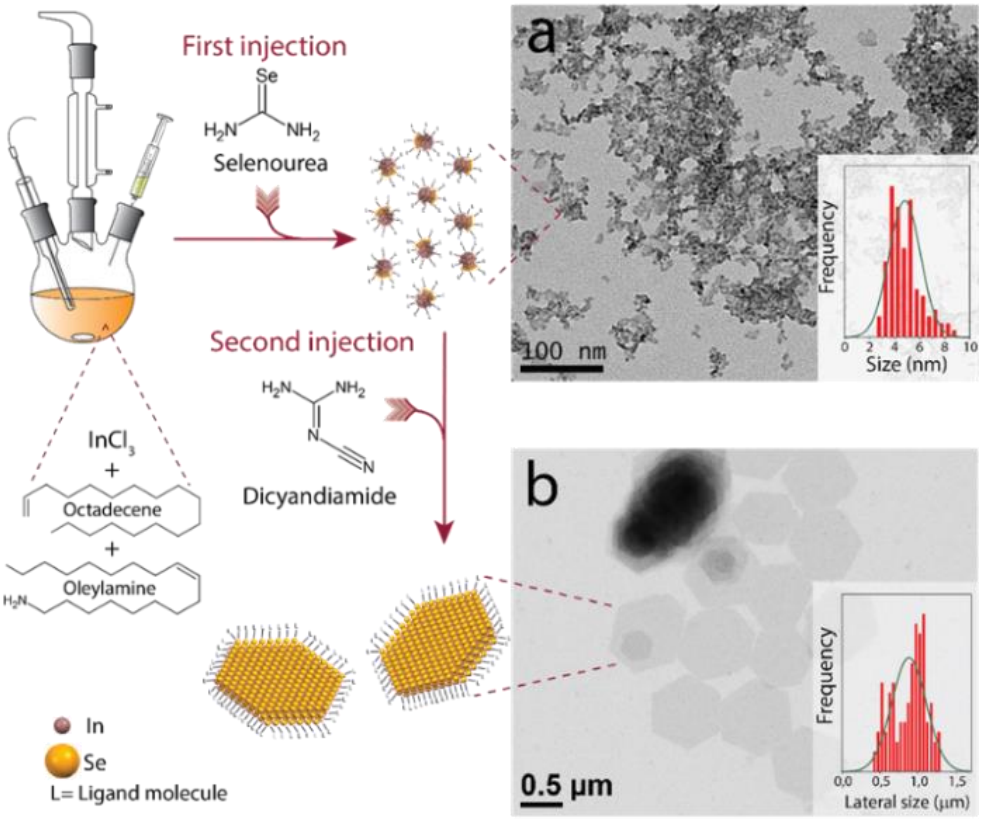

Figure 4.6 Schematic showing the growth of In_2Se_3 nanosheets by a two-step process. Representative TEM images of (a) $In_{1.8}Se_3$ nanocrystals formed upon injection of selenourea, and (b) In_2Se_3 nanosheets formed subsequently upon injection of a short aminonitrile

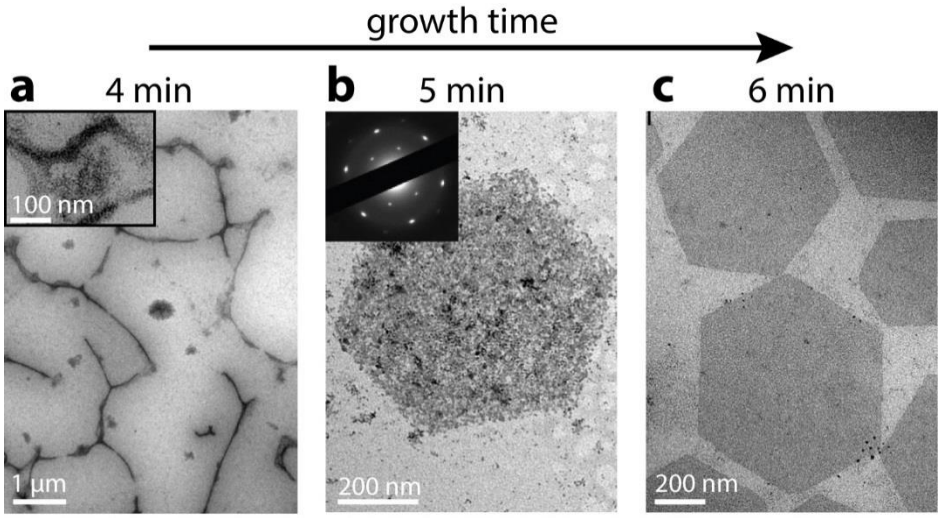

Figure 4.7 Growth of In_2Se_3 nanosheets using the double-injection approach. TEM images of aliquots collected (a) 4minutes (inset: magnified imaged), (b) 5 minutes (inset: selected area electron diffraction of a single nanosheet) and (c) 6 minutes after the injection of aminonitrile

The particles had an average size of 5 nm and average composition of $In_{1.8}Se_3$. Then, at 200 °C, a second injection containing a stoichiometric amount of dicyandiamide (in DMF) with respect to indium enabled the formation of hexagonally-shaped nanosheets (Figure 4.6b) with a $In_{2.1}Se_3$ composition, which is close to In_2Se_3, within a few minutes. Control experiments, in which the second injection consisted of just DMF (i.e. without the dicyandiamide), yielded indium selenide particles of only 5 nm, with a composition of $In_3Se_{1.92}$ and larger Se particles (see Figure A4.1 of the Appendix). This proves that dicyandiamide plays an active key role in the two-dimensional growth. Sheets could also be grown by using cyanamide instead of dicyandiamide (see Figure A4.1 of the Appendix). Shape control was lost when $InCl_3$ was replaced with other indium halides (see Figure A4.2 of the Appendix). At present, it is unclear as to why this happened, and further studies on this issues is required. One possibility is that since $InBr_3$ and InI_3 are less prone to accepting a lone-pair of electrons than $InCl_3$, they are also less reactive towards aminonitriles.

In order to investigate the two-dimensional growth, aliquots were collected along the reaction (see Figure 4.7). In the early stages after the injection of dicyandiamide t =

4 minutes), wires with several nodes (~120° angles) were present. A magnified image of these wires reveals that they are not continuous objects but are in fact made of small particles. These wires then disappear and porous hexagonal shaped nanosheets start to be observed. These are also composed of small particles, suggesting that their formation occurs via an oriented attachment mechanism. Although they might seem polycrystalline, they diffract as single crystals (see the inset of Figure 4.7b for an electron diffraction pattern of a single nanosheet). Increasing the reaction time causes the porosity to disappear and hole-free nanosheets are obtained. A clarification of whether these ligands promote an oriented attachment or a templated growth by selectively passivating the basal facets of In_2Se_3 will, however, require further study.

The average lateral dimensions of the In_2Se_3 nanosheets could be tuned by varying the concentration of oleylamine. For instance, by increasing its volume fraction from 20% to 60%, the lateral size could be tuned from 900 nm to 300 nm (see Figure A4.3 of the Appendix). The simultaneous injection of selenourea and dicyandiamide at 200˚C and 215˚C could equally deliver small nanocrystals in the early stages of the reaction, which would be followed by the formation of sheets (see Figure A4.4 of the Appendix). However, in this case, the sheets were heavily stacked. Stacking was also observed for the sheets that were prepared using the two-injection approach, albeit to a lower extent. The tendency to form stacks was accentuated by the addition of polar solvents and by centrifugation.

iii. Structural characterization and thermal stability

As previously described in detail in section 4.1v, discerning the many possible phases with an In_2Se_3 composition is difficult. In addition to the non-layered enantiomorphic γ-In_2Se_3 phase, various structural models have been proposed to describe layered phases, as is sketched in Figure 4.8. In short, the layered phases consist of covalently bonded 5-atom thick monolayers which are stacked in an ABC sequence, and they all share a very similar *a*-parameter (4.00-4.05 Å). Thus, proposed layered structures, both for a monolayer and few-layered flakes, become

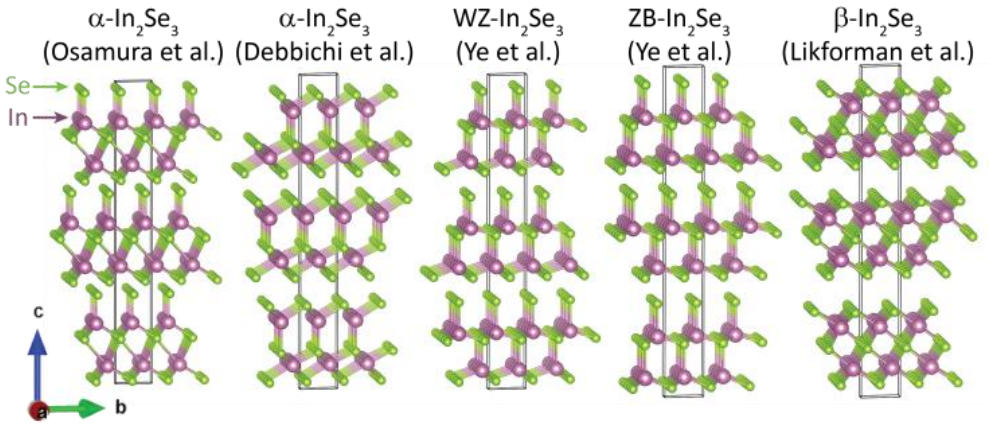

Figure 4.8. Structural models for the various proposed layered structures of In_2Se_3 (Se atoms depicted in green, In in purple) with the Van der Waals gap in between adjacent Se planes. From left to right: α-In_2Se_3 (Osamura et al.); α-In_2Se_3 (Debbichi et al.); WZ-In_2Se_3 (Ye et al.); ZB-In_2Se_3 (Ye et al.); β-In_2Se_3 (Likforman et al.).

indistinguishable from a simple qualitative analysis of their diffraction patterns. The structures differ in the coordination geometry of the indium atoms (which can be tetrahedral, octahedral, or mixed) and in the stacking sequence of the atomic layers (wurtzite or zincblende). Moreover, due to the peculiar ABC stacking, the {100} reflection is symmetrically forbidden for all the structures in the bulk.[64,66]

Here, in order to distinguish the crystal structure and the number of layers in the In_2Se_3 nanosheets, I combined high-resolution transmission electron microscopy (HRTEM) and X-ray diffraction (XRD) with the electron diffraction (ED) from the [001] oriented nanosheets. The latter method has previously been used to determine the thickness of graphene flakes.[78] ED simulations were performed to calculate the intensity ratio between the {100} and {110} reflections ($R = I_{\{100\}}/I_{\{110\}}$) as a function of the number of layers for all the proposed structures. The results are plotted in Figure 4.9a and show that the 1-layered and 2-layered flakes of most structures can be distinguishable within the experimental error.

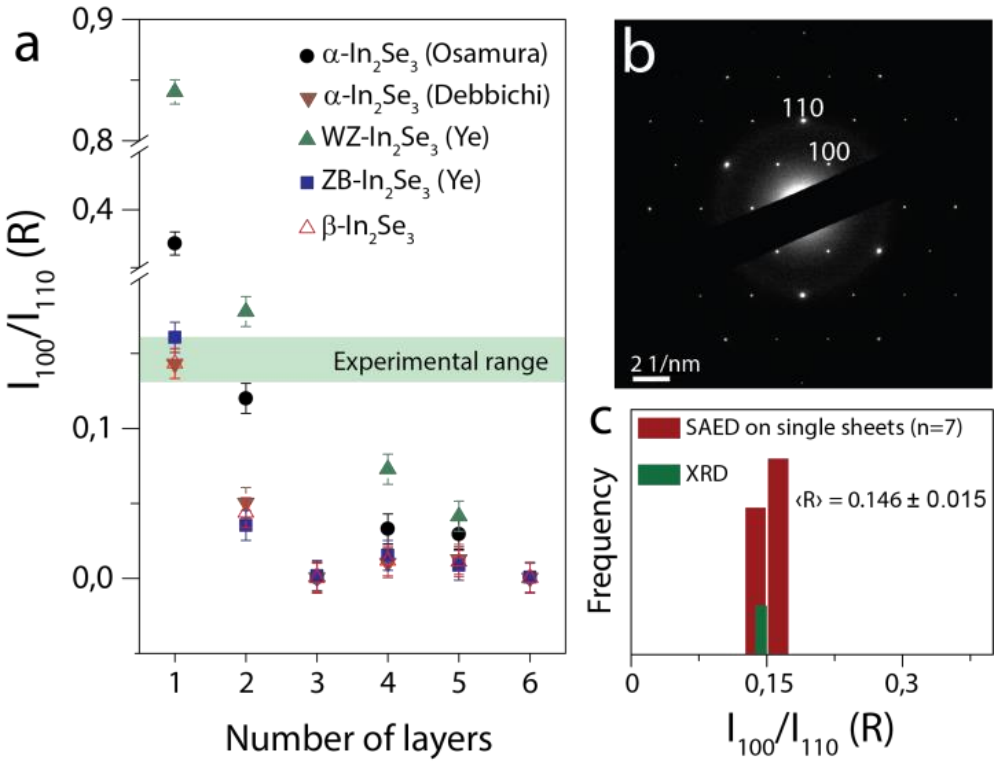

Figure 4.9 (a) ED simulations from [001] oriented nanosheets: integrated intensity ratio between (100) and (110) peaks as a function of the number of layers for all the structural models considered in Figure 2.8. (b) Typical selected-area electron diffraction pattern of a single In_2Se_3 nanosheet. (c) Distribution of intensity ratios obtained experimentally from several SAED patterns on single nanosheets and from the XRD pattern

The monolayered nature was seen by an HRTEM of side-views of folded sheets. An example is shown in Figure 4.10b: the contrast in the experimental image (top panel) is in good agreement with the one obtained from the simulation of a single layer (middle panel). Due to the experimental conditions of the imaging, the white fringes correspond to the In planes (see the sketch at the bottom of panel 2.10b). From the simulation of the ED patterns and from the HRTEM side-view it was concluded that the nanosheets consist of single layers of In_2Se_3. Two of the proposed structures, namely α-In_2Se_3 from Osamura *et al.*[79] and the WZ-In_2Se_3 from Ye *et al.*[66] can be excluded due to their high *R* values. However, three structures give very similar results: the α-In_2Se_3 and β-In_2Se_3 structures as proposed by Debbichi *et al.*[76] and Likforman *et al.*,[55] and the ZB-In_2Se_3 one by Ye *et al.*[66] For all of these structures, *R* =

0.14 ± 0.01 and, consequently, there is a very similar contrast in the HRTEM in top-view [001] orientation (Figure 4.10c).

A conclusive determination of the structure from a side-view HRTEM alone was not possible, due to contrast change depending on defocus, even if a good match with simulations was found for β-In_2Se_3 (as shown in the middle panel of Figure 4.10b). Therefore, the XRD patterns for the monolayered 2D slabs of the three structures that gave similar *R* values (from ED simulations) were also simulated and compared to the experimental pattern (see Figure 4.10a). The best match was given by β-In_2Se_3 that was proposed by Likforman et al. A small contraction of the *a*-parameter was found (a_{exp} = 3.97Å, -0.85%). The fit (red pattern in Figure 4.10a) is in good agreement with the experimental pattern (in green, Figure 4.10a). In addition, the XRD patterns for AA-stacked and ABC-stacked β-In_2Se_3 multilayered crystals were also simulated (see Figure A4.5 of the Appendix). As expected, as the number of layers increases, the broad peaks become narrower and additional peaks appear. Thus, XRD, can be a useful tool with regards to determining the number of layers.

The presence of the ligands on the surface of the sheets (even after extensive washing) was confirmed by elemental and thermogravimetric (TGA) analysis (see Figure A4.6 of the Appendix). SEM-EDS analysis confir med the presence of carbon and nitrogen in considerable amounts (12% In, 6% N, 57% C). Upon extensive washing with methanol, the amount of organic (ligands) content decreased, as can be inferred from the smaller weight loss that was observed in the TGA curve and from EDS analysis (17% In, 7% N, 47% C). The passivation of the sheets explains their average thickness of 3 nm, as was determined by atomic force microscopy measurements (see Figure 4.11a,b).[33] Therefore, these hexagonal nanosheets are organic-passivated, single-crystal 6Å̊-thick monolayers of β-In_2Se_3 with a slightly contracted *a* parameter (-0.85%) compared to the bulk. The same conclusions could be drawn for the smaller 300 nm nanosheets (see Figure 4.11c and Figure A4.3 of the Appendix). As is the case with other 2D crystals, the surface of these 5-atom thick monolayers exhibits rippling, as demonstrated by the broadening of the diffraction spots upon tilting

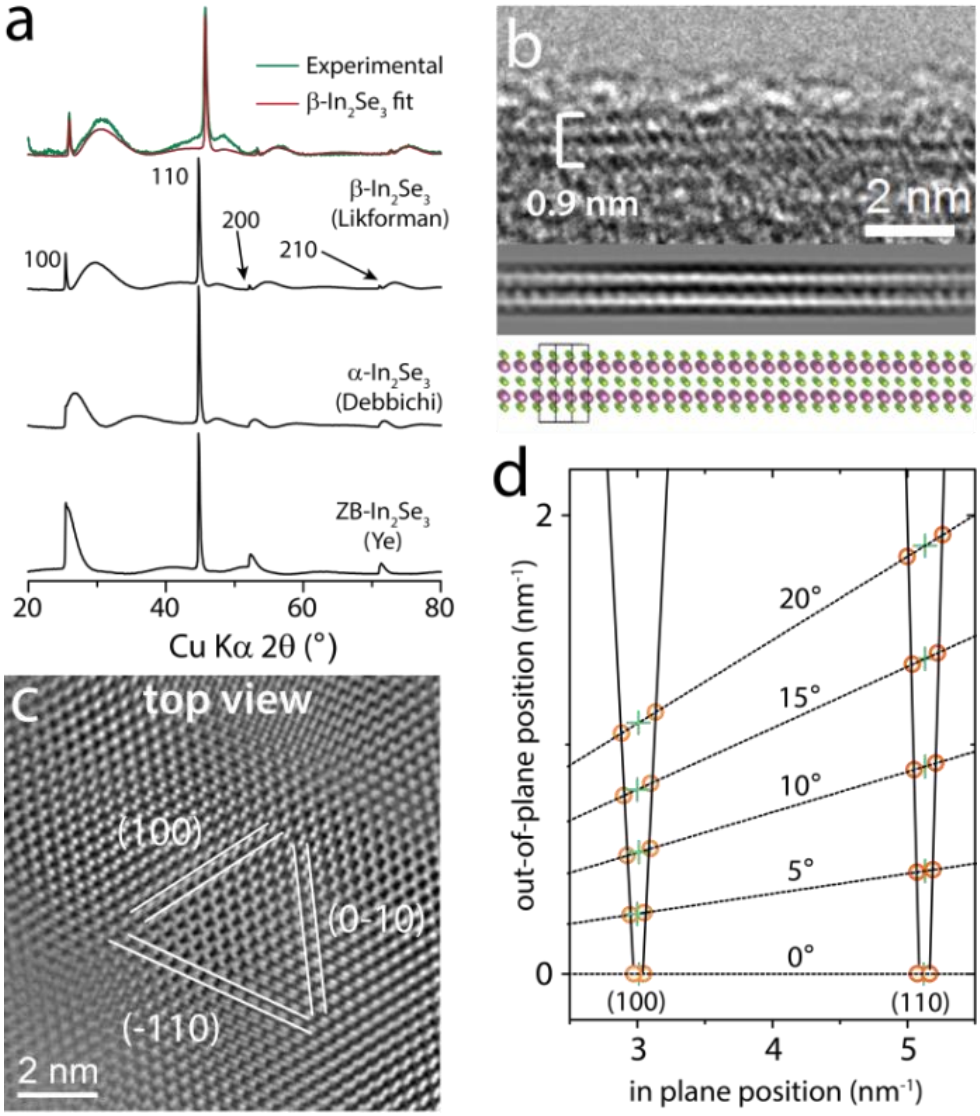

Figure 4.10 (a) Experimental XRD pattern (in green) of an In_2Se_3 nanosheet powder and simulated patterns for 2D 1-layered slabs of β (Likforman), α (Debbichi), and ZB (Ye) structures. A Debye refinement of the β structure was performed and the fit (in red) is shown along with the experimental pattern (green). (b) an HRTEM side-view image of a folded nanosheet on a holey TEM grid along with a simulated image 1° away from the [210] axis and the corresponding view of the structure model. The side view in the experimental image has a small tilt with respect to the [210] orientation. (c) HRTEM top-view image, and (d) broadening of the {100} and {2-10} diffraction spots upon tilting

(Figure 4.11d).[80,81] The presence of ripples changes the cylindrical shape of the rods, which constitute the reciprocal lattice of a perfect 2D crystal, into cones.[80] Consequently, the diffraction spots broaden upon tilting. The amplitude of the ripples can be inferred from the angle of the cone. In the present case their amplitude was below 1 nm.

The presence of the ligands on the surface of the sheets (even after extensive washing) was confirmed by elemental and thermogravimetric (TGA) analysis (see Figure A4.6 of the Appendix). SEM-EDS analysis confirmed the presence of carbon and nitrogen in considerable amounts (12% In, 6% N, 57% C). Upon extensive washing with methanol, the amount of organic (ligands) content decreased, as can be inferred from the smaller weight loss that was observed in the TGA curve and from EDS analysis (17% In, 7% N, 47% C). The passivation of the sheets explains their average thickness of 3 nm, as was determined by atomic force microscopy measurements (see Figure 4.11a,b).[33] Therefore, these hexagonal nanosheets are organic-passivated, single-crystal 6Å-thick monolayers of β-In_2Se_3 with a slightly contracted *a* parameter (-0.85%) compared to the bulk. The same conclusions could be drawn for the smaller 300 nm nanosheets (see Figure 4.11c and Figure A4.3 of the Appendix). As is the case with other 2D crystals, the surface of these 5-atom thick monolayers exhibits rippling, as demonstrated by the broadening of the diffraction spots upon tilting (Figure 4.10d).[80,81] The presence of ripples changes the cylindrical shape of the rods,

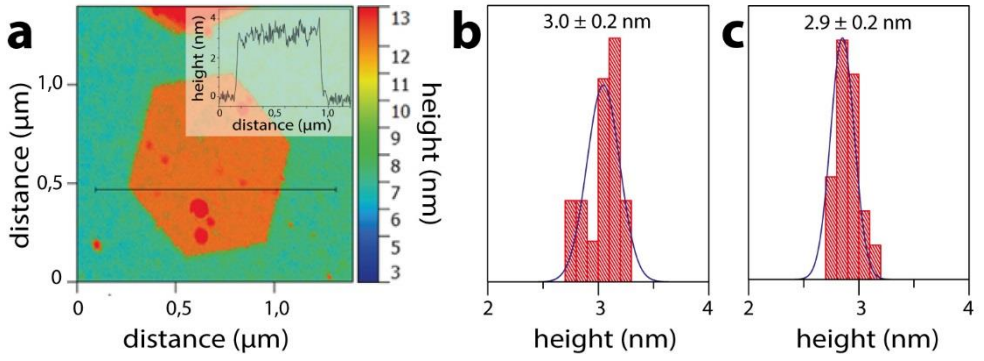

Figure 4.11 (a) Typical AFM topographic image of a single In_2Se_3 nanosheet (inset: height-profile of a line-scan). Height-distribution histograms of (b) 900 nm (n=18) and (c) 300 nm nanosheets (n=20)

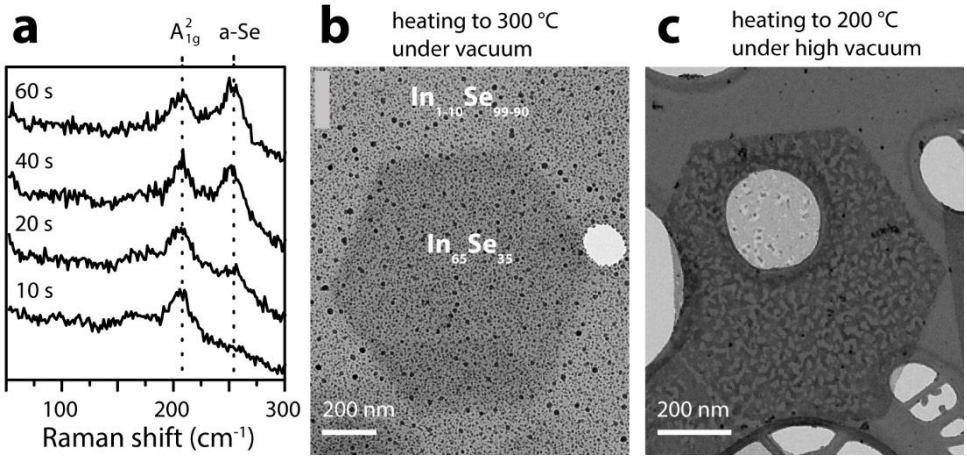

Figure 4.12 (a) Raman spectra of β-In_2Se_3 nanosheets after increasing the exposure times (λ = 514 nm, P = 0.4 mW). The peaks are attributed to the A^2_{1g} mode (205 cm^{-1}) of β-In_2Se_3 and amorphous selenium (a-Se, 250 cm^{-1}). (a,b) TEM images of nanosheets heated under vacuum

which constitute the reciprocal lattice of a perfect 2D crystal, into cones.[80] Consequently, the diffraction spots broaden upon tilting. The amplitude of the ripples can be inferred from the angle of the cone. In the present case their amplitude was below 1 nm.

Raman spectroscopy is a powerful technique for structural investigation, especially for two-dimensional materials in which the position of the shear and layer breathing modes can be exploited for the reliable determination of the number of layers, and the absence of these is characteristic of the monolayer nature.[82–85] Unfortunately, these peaks are typically located in the ultra-low frequency region, which is difficult to study experimentally. Bulk β-In_2Se_3 is known to exhibit three Raman peaks in the 100-210 cm^{-1} region, which correspond to the A^1_{1g} (110 cm^{-1}), E^2_g (180 cm^{-1}) and A^2_{1g} (205 cm^{-1}) modes. The E^2_g peak is weak and fades away in the few layered regime.[51,72,86] The Raman spectrum of as-synthesized β-In_2Se_3 nanosheets is reported in Figure 4.12a. A peak at ca. 205 cm^{-1} is observed which can be attributed to the A^2_{1g} mode of β-In_2Se_3. Another peak at ca. 250 cm^{-1} was found to evolve when the exposure time was increased, which can be attributed to amorphous selenium.[87] Ultra-thin In_2Se_3 layers have been previously reported to be easily damaged during Raman measurements.[72] Indeed, upon vacuum annealing the nanosheets (which

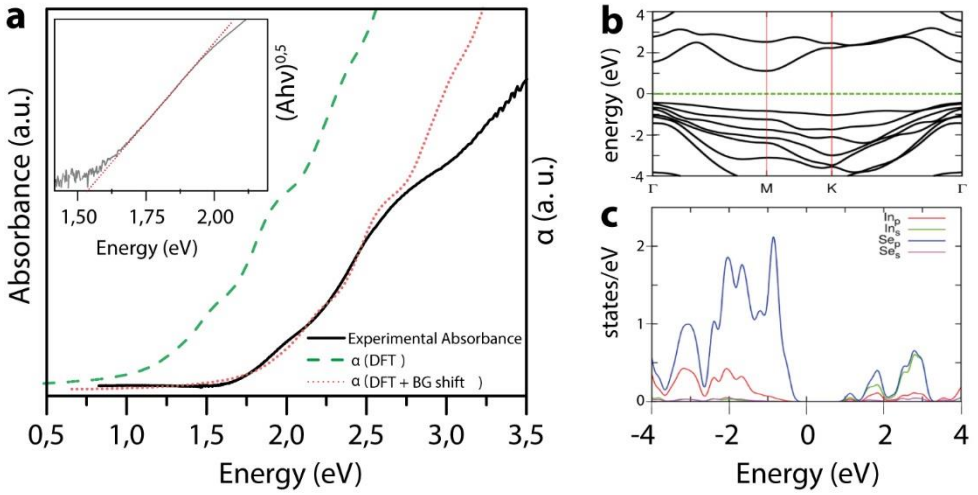

Figure 4.23 (a) Experimental absorption spectrum of β-In_2Se_3 nanosheets along with the calculated absorption spectrum for a single β-In_2Se_3 monolayer. An optical band-gap of 1.55 eV was de-termined by a Tauc plot analysis, as shown in the inset. Electronic band structure and (b) density of states (DOS) of the β-In_2Se_3 monolayer (in both cases the conduction band was rigidly shifted up in energy by 0.7 eV with respect to the DFT result, to match the onset of the calculated absorption with the experimental value)

were deposited on TEM grids), it was observed that a fraction of the chalcogen atoms was lost above a certain threshold temperature (and pressure) as is shown Figure 4.12b. The sheets maintained their structural integrity upon heating to 150 °C under vacuum (see Figure A4.7 of the Appendix), but increasing the temperature further, to 300 °C, leads to the segregation of selenium in the form of nanoparticles, which results in a porous indium-rich sheet being left behind. At higher vacuum levels, this process could be observed even at 200 °C (see Figure 4.12c), and the absence of selenium nanoparticles suggests that it sublimed in these conditions (note: the vapor pressure of selenium at 200 °C is ca. 25 mbar).[88] This observation is in line with other recent studies which have shown that thin flakes of the layered chalcogenides of post-transition metals are metastable.[72,89,90]

iv. Optoelectronic properties

The absorption spectrum of the as-synthesized β-In_2Se_3 nanosheets is shown in Figure 4.13a. It is characterized by a slow rise in absorption around the absorption edge (i.e. lack of a sharp absorption onset), which is typical of indirect semiconductors. No photoluminescence was observed. A value of 1.55 eV for the band gap was extracted by a Tauc plot analysis (Figure 4.13a inset).Bulk β-In_2Se_3 has a band-gap of 1.31 eV.[59] This data indicates that at the monolayer limit, the *c*-axis quantum confinement translates into an increase in the band-gap to 1.55 eV (this small increase can be explained by the poor electronic coupling between the layers in layered materials).

The electronic band-structure for monolayer β-In_2Se_3 was computed (Figure 4.13b), and confirms its indirect band-gap, with the lowest energy transition connecting the Γ and M symmetry points. The computed absorption coefficient (Figure 4.13a) qualitatively matches the experimental absorption spectrum, but a quantitative agreement is only obtained after applying a 0.7 eV upward shift to the calculated conduction band levels (the usual problem with PBE approximations).

Single β-In_2Se_3 monolayers were then contacted with Ti/Al or Ti/Au electrodes, as is shown in Figure 4.14a (inset). The dark current was below the detection limit of 0.5 pA and was within the applied voltage range for all samples, which is most likely due to the high contact resistance that was formed by a reversed biased Schottky barrier. Typical current-voltage curves under illumination with a laser light in the visible range for Ti/Au electrodes are displayed in Figure 4.4a. They demonstrate an almost linear behavior. For Ti/Al electrodes, the current was non-linear with increasing bias voltage (see Figure 4.8 of the Appendix), demonstrating a low current plateau around zero bias and then a superlinear increase for bias voltages larger than ± 1 V. Overall, devices with Ti/Al contacts manifested higher currents at high bias as compared to Ti/Au electrodes. This might be related to the work function of Al (around 4 eV), which is lower than that of Au (around 5 eV), resulting in a smaller Schottky barrier at the reverse biased contact. The responsivity, $R = I_{ph}/P_{inc}$, in which P_{inc} is the incident light power on the sheet area between the contacts and $I_{ph} = I_{light} - I_{dark}$

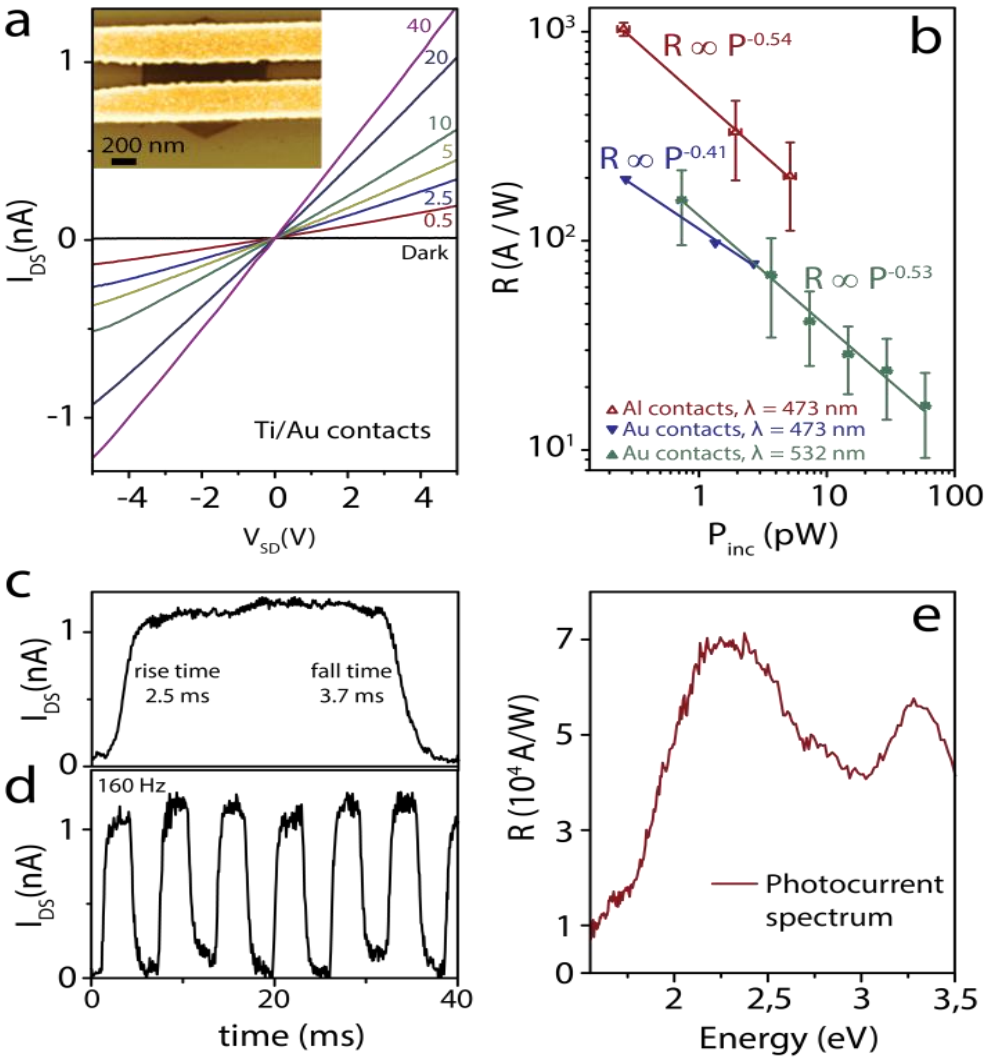

Figure 4.14 Optoelectronic performance of single monolayered β-In_2Se_3 nanosheet devices. (a) Current-voltage curves were recorded from a nanosheet that was contacted with Ti/Au electrodes in the dark and upon illumination with a 532 nm laser at different intensities (denoted in mW/cm2). The inset shows an SEM image of a single nanosheet that was contacted by two metal electrodes. (b) Photocurrent responsivity of six different devices. (c,d) Time response of the current of a device when the laser beam is (c) switched on and off, and (d) modulated by a mechanical chopper at 160Hz. (e) Photocurrent spectrum of a device under the illumination of a Xenon lamp coupled with a monochromator, recorded at a bias voltage of 10V. The impinging light power is in the fW range, which leads to responsivity values up to 7x10^4 A/W.

, is shown versus the incident laser power in Figure 4.14b for six different devices. The behavior can be well described by an inverse power-law[47,52,86] with responsivities in the 10^3 A/W range at a low laser power (a few pW) for the devices with Ti/Al electrodes. Other figures of merit, such as external quantum efficiency and detectivity, are shown in Figure 4.8 of the appendix.

The time-dependent photo-response is shown in Figure 4.14c, with a rise time of 2.5 ms and a fall time of 3.7 ms. Consequently, modulation frequencies up to 160 Hz could be well resolved (Figure 4.14d). These values of photo-responsivity and response times are comparable to the best photodetectors based on single and few-layered 2D semiconductors that have been reported so far,[26] and in particular to those of multi-layered β-In_2Se_3, which implies a higher photo-responsivity per layer in the monolayer regime.[86] Finally, the spectral dependence of the photocurrent of a single β-In_2Se_3 nanosheet device is shown in Figure 4.14e, in which a broad band centered at 2.3 eV, a pronounced low energy shoulder at around 1.6 eV, and a narrower high energy band at 3.3 eV can be identified. Note that the photocurrent spectra were recorded from single sheets on which metal layers for electrical contacts were deposited (which resulted in a Schottky field), while the absorption spectrum was taken from a film of nanosheets. This can account for the differences in the photocurrent and absorption spectra.

4.4 Conclusion

A colloidal synthesis of β-In_2Se_3 monolayered sheets with a lateral size-control up to the micrometer range was developed. The two-dimensional growth relied on the presence of short aminonitrile ligands, which were introduced to the field of colloidal synthesis for the first time. The crystal structure and the number of layers were determined by diffraction methods. In principle, the intensity ratio method, which is used here to determine the number of layers can be extended to other layered materials that crystallize in the same space group such as Bi_2Se_3, Sn_2Te_3, etc. The as-synthesized β-In_2Se_3 sheets exhibited fast and remarkably high photo-responses over the full visible range. This makes them very appealing for device applications in

layered structures with other two-dimensional materials, for example by deposition onto graphene as ultrasensitive photodetectors. Future directions will include unravelling the role of aminonitriles in the shape control of nanocrystals of materials that, like In_2Se_3, require high temperatures for their growth.

4.5 OUTLOOK

The existence of several layered structures with an In_2Se_3 composition remains a matter of debate. To date, only the β-structure has been accurately characterized and consists of a tetradymite-like structure. It is now well known that the archetypical tetradymite, Bi_2Te_3, becomes distorted upon the replacement of Bi or Te by elements with a smaller radius, such as Sb, As or S.[9] Therefore, it wouldn't be surprising if such distortions occurred in the indium selenide system. In fact, Ji et al.[64] demonstrated that bulk β-In_2Se_3 displays a positional disorder within the middle Se-layer, i.e. each Se atom occupies six fractionally occupied positions, and they also noted that impurities play an important role in the stabilization of the layered structure. Given that Se-vacancies are the major type of defects in tetradymite selenides, it would be interesting to understand how they affect the structure of β-In_2Se_3. The relevance of this question is supported by the fact that the migration of Se-atoms, shown in this work, occured in the same temperature range as that in which the so-called α to β transition takes place.[71] This is reinforced by the fact that a broad range of values have been reported for the electrical resistivity of layered In_2Se_3 (which is discussed in more detail in the following paragraph). Another intriguing mystery in this material is the origin of the photoluminescence that was observed by some groups, especially given the fact that band structure calculations always point to indirect band-gaps, regardless of the thickness of the crystals.[53,76,86]

Although the band-gap of β-In_2Se_3 (1.3-1.5 eV)is appropriate for application in solar cells, photodetectors and field-effect transistors (FET), it seems that it is intrinsically a very resistive phase (as has been demonstrated in this work and by others).[64,71] Therefore, controlling the doping levels in layered In_2Se_3 could be of great interest. In this regard, Ji et al. could decrease its resistivity to ca. 10^{-4} ohm.cm by introducing Sn (0.5% Sn with respect to In), and Eddike et al. could further decrease it to ca. 10^{-2}

using Sb as dopant (up to 3% Sb with respect to In).[91] However, these values are still low for electronic applications (semiconductors used in FETs typically have a resistivity of 1 ohm.cm). Nevertheless, it should be noted that these works were conducted on bulk crystals. At the nanoscale, the introduction of a small number of defects or impurities can actually translate into very high doping levels. In this regard, recent studies have demonstrated the realization of field effect transistors with layered In_2Se_3 thin-flakes.[52,53] No external dopants were reported to be present in these materials, which suggests that their good electronic properties could be due to self-doping, i.e. due to the presence of defects such as Se-vacancies, which were introduced in the previous section. Heavy doping in ultra-thin β-In_2Se_3 flakes could possibly also be achieved using surface functionalization strategies similar to those which have already been demonstrated for other two-dimensional layered chalcogenides.[28,92]

4.6 References

(1) Auerbach, S. M. *Handbook of layered materials*; **2004**.

(2) Dresselhaus, M. S. Intercalation in Layered Materials; **1986**.

(3) Julien, C. New Trends in Intercalation Compounds for Energy Storage; **2002**.

(4) Friend, R. H. *Adv. Phys.* **1987**, *34*, 1.

(5) Novoselov, K. S. *Science* **2004**, *306*, 666.

(6) Lalmi, B. *Appl. Phys. Lett.* **2010**, *97*, 223109.

(7) Mannix, A. J. *Science* **2015**, *350*, 1513.

(8) Leith, R. M. A. Preparation and Crystal Growth of Materials with Layered Structures; **1977**.

(9) Heremans, J. P. Nat. Rev. Mat. **2017**, *2*, 17049.

(10) Lei, J.-C. *Front. Phys.* **2015**, *10*, 276.

(11) Anasori, B. *Nat. Rev. Mater.* **2017**, *2*, 16098.

(12) Rainer, P. *Z. Naturforsch.* **2008**, *63b*, 1135.

(13) Chen, X. H. *Nature* **2008**, *453*, 761.

(14) Novoselov, K. S. *Nature* **2005**, *438*, 197.

(15) Katsnelson, M. I. *Nat. Phys.* **2006**, *2*, 620
(16) Chen, S. *Science* **2016**, *353*, 1522
(17) Boneschanscher, M. P. *Science* **2014**, *344*, 1377.
(18) Beugeling, W. *Nat. Commun.* **2015**, *6*, 6316.
(19) Dean, C. R. *Nat. Nanotechnol.* **2010**, *5*, 722.
(20) Xu, S. *2D Mater.* **2016**, *3*, 21007.
(21) Ataca, C. J. Phys. Chem. C **2012**, *116*, 8983
(22) Mak, K. F. *Phys. Rev. Lett.* **2010**, *105*, 136805.
(23) Splendiani, A. *Nano Lett.* **2010**, *10*, 1271.
(24) Mak, K. F. *Nat. Photonics* **2016**, *10*, 216.
(25) Zhou, X. *J. Am. Chem. Soc.* **2015**, *137*, 7994.
(26) Buscema, M. *Chem Soc Rev* **2015**, *44*, 3691.
(27) Coleman, J. N. *Science* **2011**, *331*, 568.
(28) Cullen, P. L. *Nat. Chem.* **2016**, *9*, 244.
(29) Li, X. *Science* **2009**, *324*, 1312.
(30) Shi, Y. *Chem. Soc. Rev.* **2015**, *44*, 2744.
(31) Nasilowski, M. *Chem. Rev.* **2016**, *116*, 10934.
(32) Ithurria, S. *J. Am. Chem. Soc.* **2008**, *130*, 16504.
(33) Schliehe, C. *Science* **2010**, *329*, 550.
(34) Stam, W. Van Der. *Chem. Mater.* **2014**, *27*, 283.
(35) Shamsi, J. *J. Am. Chem. Soc.* **2016**, *138*, 77240.
(36) Yoo, D. *J. Am. Chem. Soc.* **2014**, *136*, 14670.
(37) Jung, W. *J. Am. Chem. Soc.* **2015**, *137*, 7266.
(38) Oyler, K. D. *Chem. Mater.* **2009**, *21* (15), 3655.
(39) Vaughn, D. D. *J. Am. Chem. Soc.* **2010**, *132*, 15170.
(40) Li, L. *J. Am. Chem. Soc.* **2013**, *135*, 1213.
(41) Chan, Y. *Chem. Mater.* **2014**, *26*, 6120.
(42) Kamat, P. V. **1987**, *9*, 1004.
(43) Yang, S. *J. Phys. Chem. B* **2005**, *109*, 12701.
(44) Park, K. H. *J. Am. Chem. Soc.* **2006**, *128*, 14780.
(45) Lauth, J. *Chem. Mater.* **2016**, *28*, 1728.
(46) Lei, S. *ACS Nano* **2014**, *2*, 1263.

(47) Tamalampudi, S. R. *Nano Lett.* **2014**, *14*, 2800.
(48) Mudd, G. W. *Adv. Mater.* **2015**, *27*, 3760.
(49) Lei, S. *Nano Lett.* **2015**, *5*, 3048
(50) Bandurin, D. A. *Nat. Nanotechnol.* **2016**, *12*, 223.
(51) Jacobs-Gedrim, R. B. ACS Nano **2014**, *1*, 514.
(52) Island, J. O. *Nano Lett.* **2015**, *12*, 7853.
(53) Zhou, J. *Nano Lett.* **2015**, *15*, 6400.
(54) Newman, P. C. *J. Phys. Chem. solids* **1962**, *23*, 19.
(55) Likforman, A. *Acta Crystallogr.* **1978**, *34*, 1.
(56) Likforman, A. *J. Solid State Chem.* **1980**, *33*, 91.
(57) Pfitzner, A. *J. Solid State Chem.* **1996**, *124*, 305.
(58) Ye, J. *Jpn. J. Appl. Phys.* **1998**, *37*, 4264.
(59) C. Julien, A. Chevy, D. S. *Phys. stat. sol.* **1990**, *118*, 553.
(60) De Groot, C. H. *J. Appl. Phys.* **2001**, *89*, 4336.
(61) Chaiken, A. *J. Appl. Phys.* **2003**, *94*, 2390.
(62) Yudasaka, M. *Thin Solid Films* **1987**, *146*, 65.
(63) Emziane, M. *Mater. Chem. Phys.* **2000**, *62*, 84.
(64) Ji, H. *Mater. Res. Bull.* **2013**, *48*, 2517.
(65) Landuyt, J. *Phys. Stat. Sol.* **1975**, *30*, *299.*
(66) Ye, J. *Jpn. J. Appi. Phys.* **1998**, *37*, 4264.
(67) Lutz, H. D. *J. Less-Common Met.* **1988**, *143*, 83.
(68) Julien, C. *Thin Solid Films* **1986**, *137*, 27.
(69) Popović, S. *Phys. Status Solidi* **1971**, *6*, 301.
(70) Rasmussen, A. M. *Appl. Phys. Lett.* **2013**, *102*, 7.
(71) H. Miyazawa, S. S. *J. Phys. Soc. Japan* **1957**, *12.*
(72) Tao, X. *Nano Lett.* **2013**, *13*, 3501.
(73) Bertoni, G. *ACS Nano* **2012**, *6*, 6453.
(74) Debye, P. *Ann. Phys.* **1915**, *351*, 809.
(75) Giannozzi, P. J. Phys. Condens. Matter **2009**, 21, 395502.
(76) Debbichi, L. *J. Phys. Chem. Lettrs* **2015**, *6*, 3098.
(77) Wang, S. *J. Phys. Chem. B* **2005**, *109*, 17281.
(78) Meyer, J. C. *Solid State Commun.* **2007**, *143*, 101.

(79) Osamura, K. *J. Phys. Soc. Japan.* **1966**, *21*, 1848.
(80) J. C. Meyer. *Nature* **2007**, *446*, 60.
(81) Brivio, J. *Nano Lett.* **2011**, *11*, 5148.
(82) Tan, P. H. *Nat. Mater.* **2011**, *11*, 294.
(83) Lui, C. H. *Nano Lett.* **2014**, *14*, 4615.
(84) Zhang, X. *Chem. Soc. Rev.* **2015**, *44*, 2757.
(85) Zhao, Y. Phys. Rev. B - Condens. Matter Mater. Phys. **2014**, 90, 1.
(86) Balakrishnan, N. *2D Mater.* **2016**, *3*, 1.
(87) Lucovsky, G. *Solid State Commun.* **1967**, *5*, 113.
(88) Brooks, L. S. *J. Am. Chem. Soc.* **1952**, *74*, 227.
(89) Buha, J. *Nano Lett.*, **2016**, *16*, 4217
(90) Sutter, E. *Nano Lett.*, **2016**, *16*, 4410.
(91) Eddike, D. *Mater. Res. Bull.* **1998**, *33*, 519.
(92) Lei, S. *Nat. Nanotechnol.* **2016**, *11*, 465.

4.7 Appendix

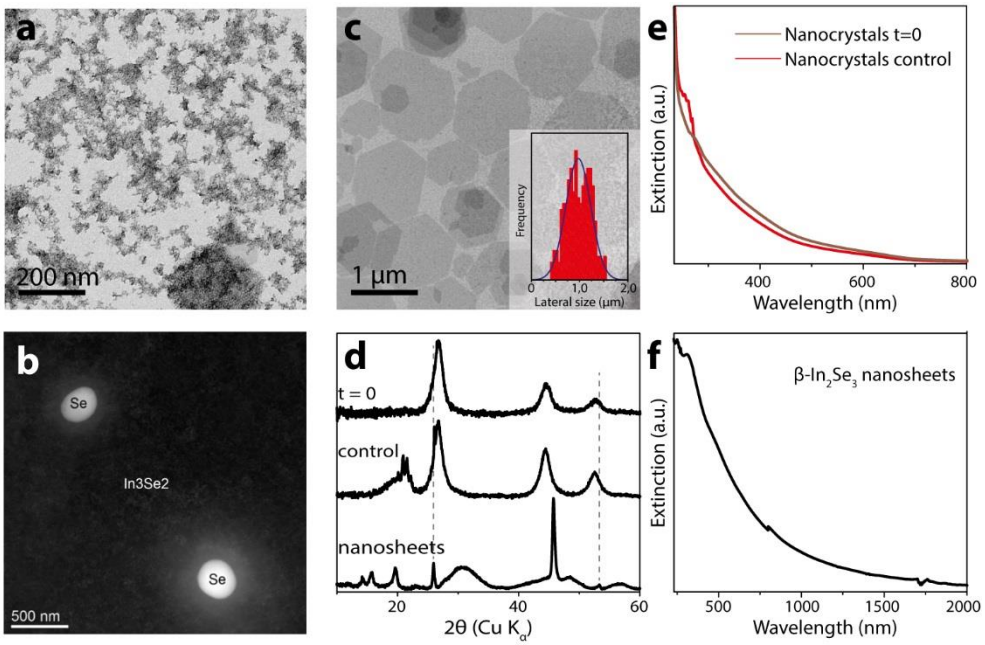

Figure A 4.2(a) TEM image of nanocrystals with an average composition of In_3Se_2 assessed by HRTEM-EDS resulting from a control experiment in which a DMF blank (i.e. without selenourea) was employed as a second injection. (b) HAADF-STEM image highlighting large selenium particles which were formed along with the In_3Se_2 nanocrystals. (c) TEM image of the nanosheets grown with cyanamide instead of dicyandiamide (in inset: size-distribution histogram). (d) XRD patterns of the nanocrystals that formed upon the injection of selenourea (denoted as t=0) and of those resulting from the control experiment, along with that obtained for the β-In_2Se_3 nanosheets for comparison. The extinction spectra of the dispersions of the nanocrystals and nanosheets in hexane are shown in (e) and (f) respectively

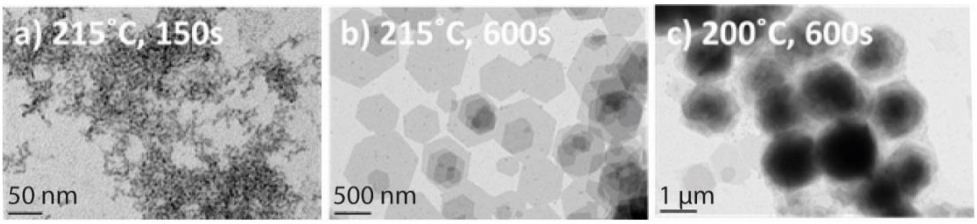

Figure A 4.1 TEM images of nanocrystals, obtained by replacing $InCl_3$ with (a) $InBr_3$ and (b) InI_3 and maintaining all other reaction conditions identical to those described for the synthesis of 900 nm β-In_2Se_3 nanosheets

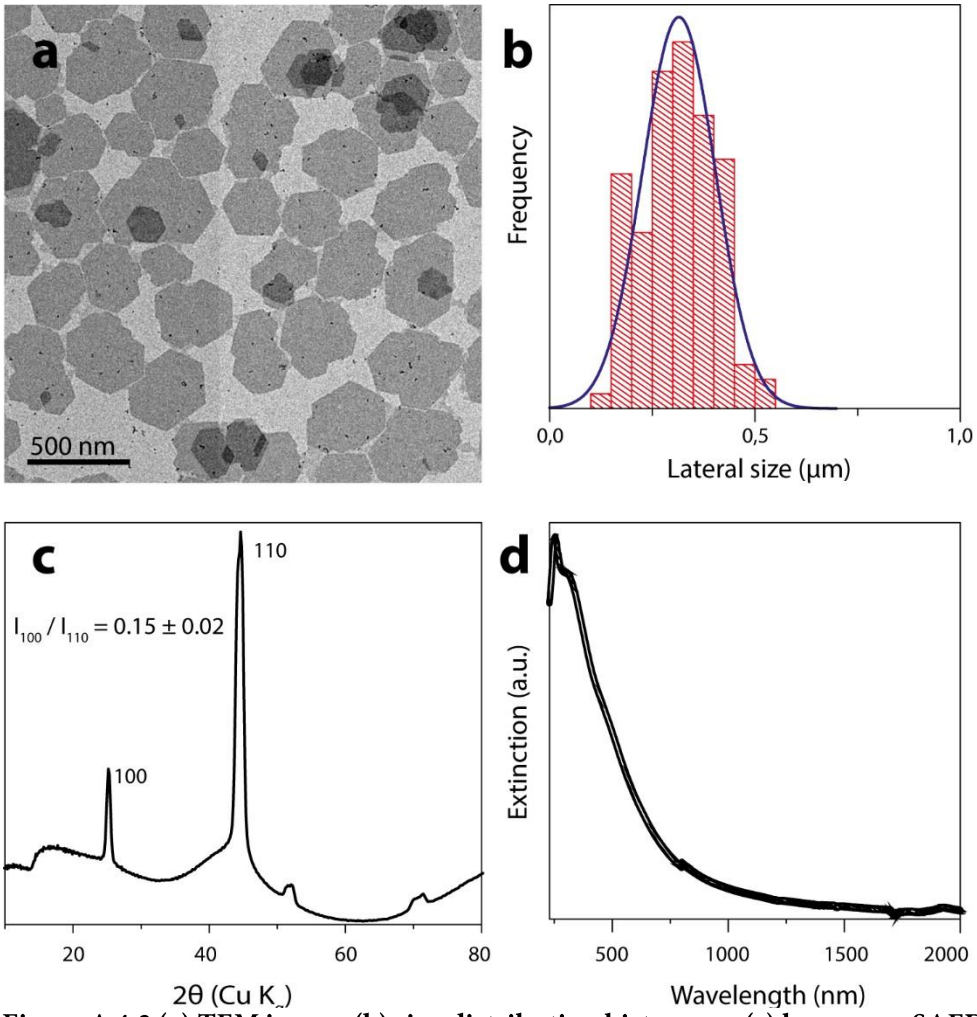

Figure A 4.3 (a) TEM image, (b) size-distribution histogram, (c) large-area SAED pattern and (d) extinction spectrum of 300 nm nanosheets synthesized with 60 % volume fraction of oleylamine (all other reaction conditions were kept the same as those used to synthesize the 900 nm β-In_2Se_3 nanosheets)

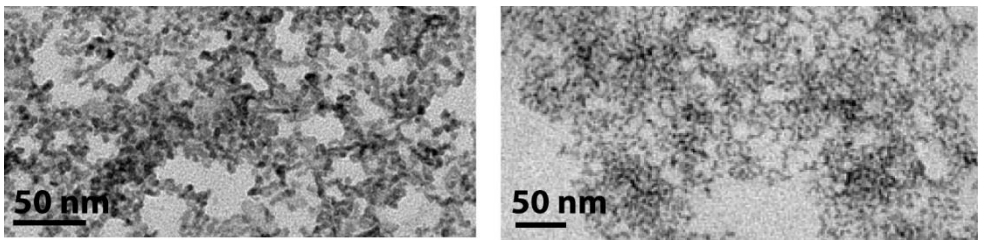

Figure A 4.4 TEM images of indium selenide nanocrystals and nanosheets obtained with a single-injection procedure at (a,b) 215°C and at (c) 200°C

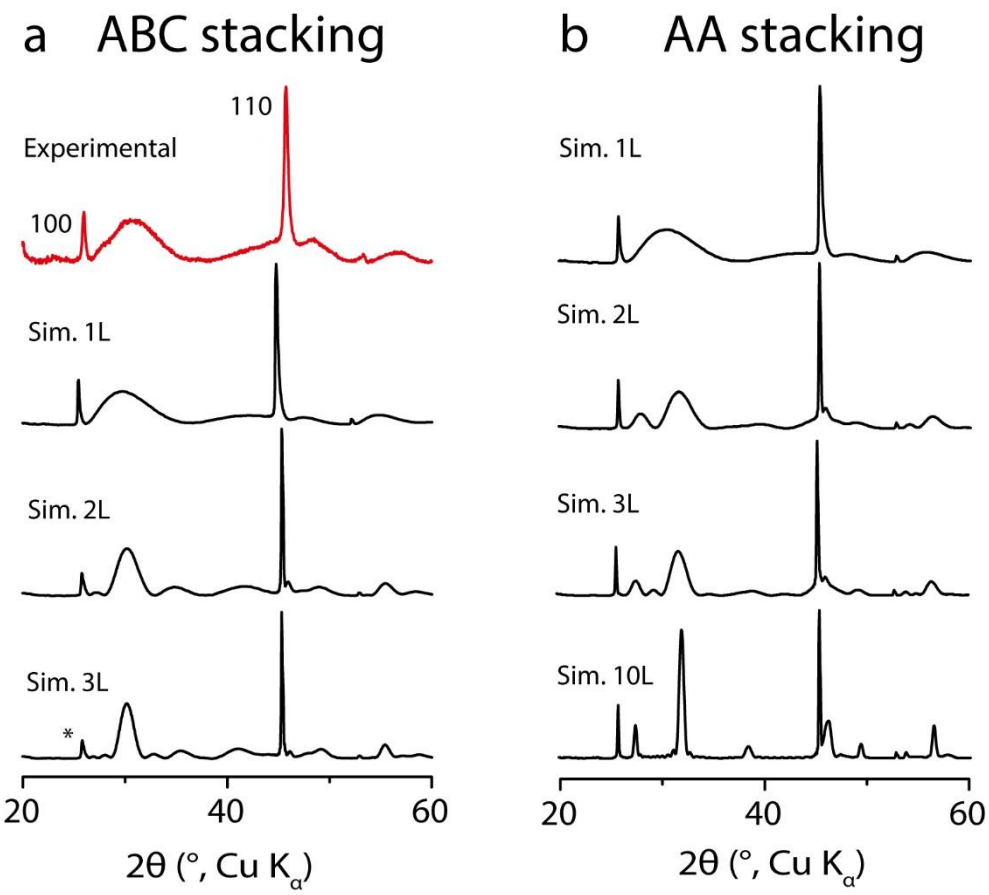

Figure A 4.5 Simulated XRD patterns of (a) ABC-stacked and (b) AA-stacked β-In_2Se_3 crystal 1 to 10 layers thick. The experimental XRD pattern obtained for the β-In_2Se_3 nanosheets that were synthesized in this work is shown in panel (a). For comparison the peak labeled with an asterisk (*) in the 3-layered pattern is assigned to the superposition of the (101) and (111) reflections, not to the (100) peak.

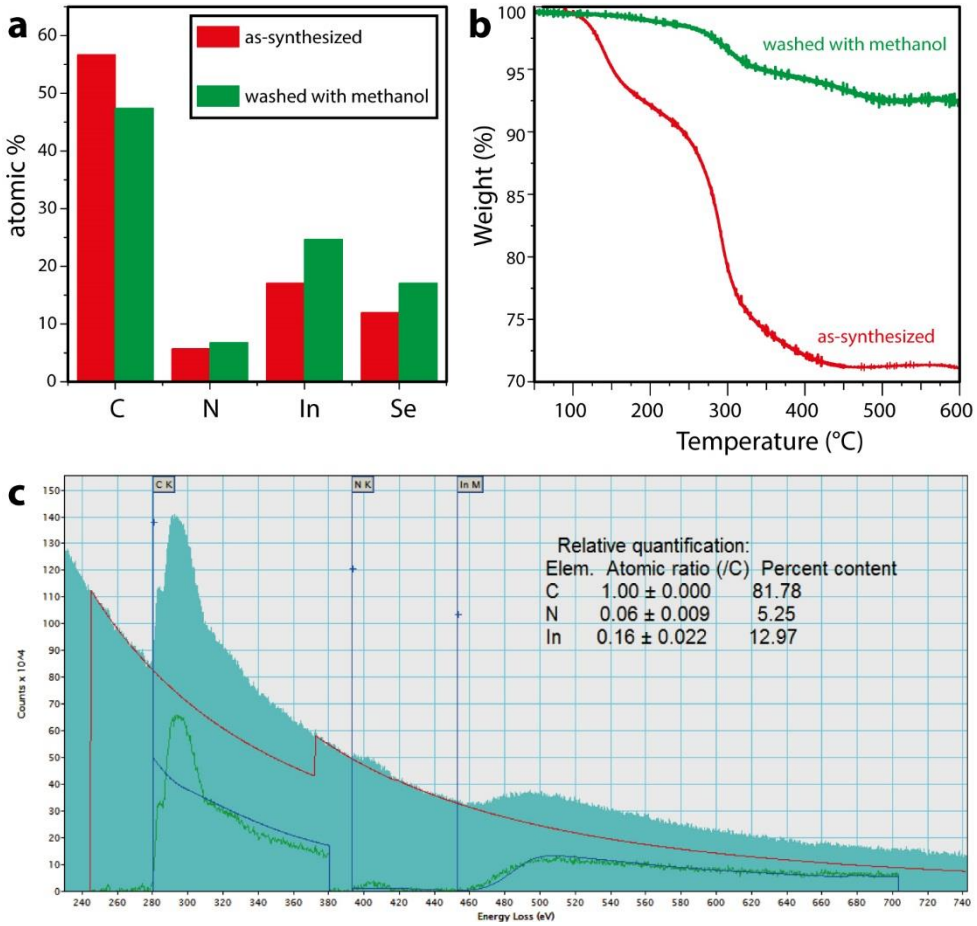

Figure A 4.6 (a) Elemental composition (determined by SEM-EDS) and thermogravimetric analysis of nanosheet samples. Similar results in terms of composition were obtained by analyzing the (c) EELS spectrum of a single β-In2Se3 nanosheet

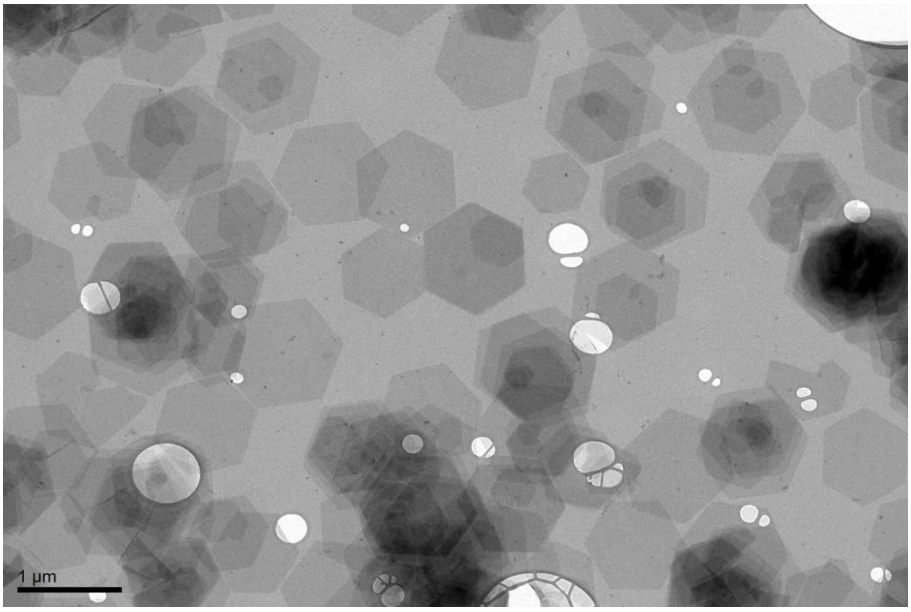

Figure A 4.7 TEM image of β-In_2Se_3 heated under vacuum to 150 °C

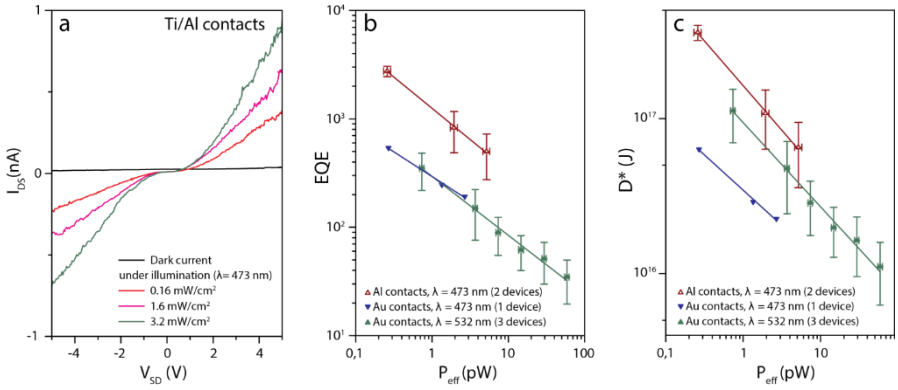

Figure A 4.8 (a) Current-voltage curves recorded from a single monolayer β-In2Se3 nanosheet which was contacted with Ti/Al electrodes in the dark and upon illumination with a 473 nm laser. (b) External quantum efficiencies (EQE) and (c) detectivities (D*) of several β-In2Se3 monolayered devices at 5V bias.

5 Conclusions

This dissertation focused on the development of colloidal synthetic routes for novel nano-crystalline semiconductors of interest in light conversion processes, in particular, $CuFeS_2$ for photon-to-heat conversion, $CsPbBr_3$ for photoluminescence and In_2Se_3 for photo-current generation.

Synthesis-wise, an interesting degree of control could be obtained in these systems. For instance, monodisperse tetragonal $CuFeS_2$ nanocrystals with trigonal pyramidal or square bipyramidal shape could be synthesized. The synthesis of this ternary system was until now hindered by the formation of CuS rich phases, which could be completely avoided in this case. The phase purity could be achieved by applying acid base concepts in order to reduce the reactivity of Cu^+. Acid-base concepts were also observed to be key in the size, shape and phase control of lead halide perovskite nanocrystals. In particular, the acid base interactions between oleylamine and oleic acid, ligands generally employed in colloidal synthesis, were investigated and could be exploited to synthesize monodisperse nanocubes and nanoplatelets. Furthermore, it was also found that the phase stability of this system is greatly influenced by the amount and relative concentration of these two ligands. Although these ligands can provide good size and shape control, they are not ideal candidates for passivating these nanocrystals, and therefore a new synthetic route, employing phosphine oxide ligands, was also proposed. Two-dimensional growth could also be achieved in another system, namely indium selenide. In this case, nanosheets with tuneable lateral sizes could be synthesized employing a mixture of oleylamine and aminonitriles such as cyanamide or dicyandiamide. To the best of the author's knowledge, this is the first time that aminonitriles were employed in colloidal synthesis. In comparison to other short ligands, they have the advantage of possessing very high boiling points.

All the samples produced in this work were optically and structurally investigated. In particular, an important part of the work is devoted to the crystal structures of these materials. In particular, the structural investigation of indium selenide was an interesting challenge that could only be solved by combining experiments and simulations. Optically, these materials were characterized via steady-state and transient spectroscopic techniques. Finally, application-wise $CuFeS_2$ and In_2Se_3 were exploited for photothermal conversion and photo-thermal generation, respectively. The results were quite satisfying as well. A photo-thermal conversion efficiency of 49 % could be achieved with $CuFeS_2$ nanocrystals and In_2Se_3 nanosheets were found to be promising materials for photodetection. Only CsPbBr3 were not exploited for any application, however it should be noted that there already exists a lot of literature in this regard.

List of publications

Publications (Equal contributing authors are underlined):

(4) Almeida, G; Goldoni, L.; Akkerman, Q.; Dang, Z.; Khan, A. H.; Marras, S.; Moreels, I.; Manna, L. The Role of Acid-Base Equilibria in the Size, Shape and Phase Control of Cesium Lead Bromide Nanocrystals. ACS Nano, 2018, 12, 1704-1711

(3) Palazon, F.; Almeida, G.; Akkerman, Q. A.; De Trizio, L.; Dang, Z.; Prato, M.; Manna, L. Changing the Dimensionality of Cesium Lead Bromide Nanocrystals by Reversible Postsynthesis Transformations with Amines. Chem. Mater. 2017, 29, 4167–4171.

(2) Almeida, G.; Dogan, S.; Bertoni, G.; Giannini, C.; Gaspari, R.; Perissinotto, S.; Krahne, R.; Ghosh, S.; Manna, L. Colloidal Monolayer β-In2Se3 Nanosheets with High Photoresponsivity. J. Am. Chem. Soc. 2017, 139, 3005–3011.

(1) Ghosh, S.; Avellini, T.; Petrelli, A.; Kriegel, I.; Gaspari, R.; Almeida, G.; Bertoni, G.; Cavalli, A.; Scotognella, F.; Pellegrino, T.; et al. Colloidal CuFeS2 Nanocrystals: Intermediate Fe d-Band Leads to High Photothermal Conversion Efficiency. Chem. Mater. 2016, 28, 4848-4858

Contributions to scientific conferences as presenting author:

(4) MRS fall 2017, Boston (oral presentation on In_2Se_3)

(3) Nanoge September meeting 2017, Barcelona (oral presentation on In_2Se_3)

(2) Graphene 2017, Barcelona (Poster presentation on In_2Se_3)

(1) ISN2A 2016, Lisbon (poster presentation on In_2Se_3)

ACKNOWLEDGEMENTS

Having been raised in a family full of people related to social sciences, I would probably not have pursued the study of natural sciences if it wasn't for my grandfather Ramiro. It is with great joy that I recall all the days of my childhood that I spent learning and playing in his company, as well as all the dedication he put into introducing me to science and research. He's certainly the wisest person I have ever met and I feel lucky for having him as grandfather. Today I still consult him every time I need to take an important decision! I also want to thank my parents for raising me – which was certainly not an easy task – and for all the sacrifices they made so that me and my little sister had a comfortable life and a quality education. Both of us decided to leave our country to pursue our studies abroad, which is a reflection of the adventurous spirit that our parents transmitted to us, for which I am very grateful.

I also want to thank many people that I met here in Italy. First, a big thanks to all those who helped me during my doctorate, in particular to my supervisor, Libero, who made my adventure in Italy and in particular, at a high-quality, multidisciplinary and global research institute, possible. Then, to all the co-authors of my publications and in particular to Giovanni Bertoni (from whom I learned a lot about crystallography) for his tireless efforts. Then to all the colleagues that made my stay at IIT a pleasant journey and in particular to those that also became good friends: Anatolyi Polovitsyn, Umair Gulzar, Arjen Boender, Sedat Dogan, Quinten Akkerman, Joao Bimbo and Nuno Garcia! Finally I also want to acknowledge those from outside the workplace that I will recall forever. These include, Marco Gaviglio, the first person I met in Italy, and Eugenia Amisano, at whose place I've been living for the past three years – who provided me invaluable help and offered me their great companionship!